Droplet collisions in turbulence

-An experimental study-

Gosse Oldenziel

Droplet collisions in turbulence

-An experimental study-

PROEFSCHRIFT

ter verkrijging van de graad van doctor
aan de Technische Universiteit Delft,
op gezag van de Rector Magnificus prof. ir. K. C. A. M. Luyben,
voorzitter van het College voor Promoties,
in het openbaar te verdedigen op
vrijdag 2 mei 2014 om 10:00 uur

door

Gosse OLDENZIEL
Master of Science Aerospace Engineering (M.Sc)
geboren te Haarlem, Nederland.

Dit proefschrift is goedgekeurd door de promotor:
Prof. dr. ir. J. Westerweel

Copromotor: Dr. ir. G. E. Elsinga

Samenstelling promotiecommissie:

Rector Magnificus,	Technische Universiteit Delft	voorzitter
Prof. dr. ir. J. Westerweel,	Technische Universiteit Delft	promotor
Dr. ir. G. E. Elsinga,	Technische Universiteit Delft	copromotor
Prof. dr. F. Toschi,	Technische universiteit Eindhoven	
Prof. dr. ir. J.F. Dijksman,	Universiteit Twente	
Prof. dr. E.K. Longmire,	University of Minnesota	
Prof. dr. ir. W. van de Water,	Technische universiteit Eindhoven	
Prof. dr. ir. G. Ooms,	Technische Universiteit Delft	
Prof. dr. ir. B. J. Boersma,	Technische Universiteit Delft	reservelid

This work is part of the research programme of the Foundation for Fundamental Research on Matter (FOM), which is part of the Netherlands Organisation for Scientific Research (NWO).

Cover design: Friso Blankevoort (freshco.org)

ISBN/EAN 9789461086594

Printed by Gildeprint V.V., Enschede

Contents

Summary

Droplet collisions in turbulence: An experimental study

– Gosse Oldenziel –

Liquid droplets occur in many natural phenomena and play an important role in a large number of industrial applications. One of the distinct properties of droplets as opposed to solid particles is their ability to merge, or coalesce upon collision. Coalescence of liquid drops is of importance in for example the food industry, where the shelf life of emulsion type of products is often elongated with absence of coalescence, rocket propulsion, where fuel and oxidizer are separately injected and ignite upon coalescence, the semiconductor industry, where droplets of molten tin are targeted by a laser to produce extreme ultraviolet light, and during the formation of rain. One might not realize it immediately, but the outcome of a droplet collision is not always coalescence, but also bouncing can occur.

In most of the mentioned cases the droplet collisions do not take place in a stationary environment but in an environment that flows with respect to the droplets or is even turbulent. The aim of the current study is to gain insight into the effect of external turbulence on the outcome of droplet collisions.

When two droplets collide it might appear that the drops are in contact, but in reality there will be a thin film of surrounding fluid in between the droplets. When this film becomes so thin that Van der Waals forces between the molecules of the two drops come into effect a hole will be initiated in the film and the droplets will coalesce. The associated thickness is in the order of $\mathcal{O}(60nm)$. If the film thickness does not decrease to this value, the droplets will bounce. The time it takes from the start of drop interaction to film rupture is called the drainage time, denoted by $t_{drainage}$. The time during which the drops are in apparent contact is called the interaction time $t_{interaction}$. A droplet collision will thus lead to coalescence when $t_{drainage} < t_{interaction}$, otherwise the collision results in bouncing.

To investigate film drainage an experiment was performed where a droplet of silicone oil was released in a layer of water below a layer of silicone oil. A film of water will form between the drop and the top liquid. Because the interaction time $t_{interaction}$ is always larger than the drainage time $t_{drainage}$, the film will eventually always rupture.

Refractive index matching and laser induced fluorescence (LIF) were used to image the film and determine its thickness and rupture location. The measurements show that the film attains a specific geometry. The film is thick at the center and thin at an off center ring.

This geometry is termed a 'dimple'. The measurements also show that the film ruptures faster than simple analytical models predict and that the film thins asymmetrically. The rupture locations correlate with the region of minimal thickness.
After the investigation of film drainage, investigation of droplet collisions with realistic values for the interaction time become of interest together with the influence of external turbulence. In order to investigate both phenomena a cylindrical tank was designed with discs at the top and bottom which could counter rotate at fixed frequency. The flow between counter rotating discs is referred to as Von Kármán flow. At the center of the flow facility a small volume exists where the average flow is approximately zero, but the turbulent velocity fluctuations are finite. Nozzles were mounted in the Von Kármán flow facility to inject droplets to produce collisions at this location. Droplets could be collided in a stationary flow and in a turbulent flow and using three high speed cameras the droplets could be tracked in 3D. The Reynolds number based on the Taylor micro scale and the turbulent fluctuations, denoted as Re_λ, is zero in case of a stationary flow $Re_\lambda = 0$ and for the turbulent case it holds that $Re_\lambda = 141$.
The collisions are characterized using the Weber number $We = \frac{\rho_d U^2 D}{\sigma}$ based on the drop density ρ_d, the relative drop velocity U, the drop diameter D and the interfacial tension σ. The Weber number is an indicator for the balance of inertial forces over surface tension forces.
In case of droplet collisions in a stationary liquid ($Re_\lambda = 0$) for low values of the Weber number the outcome of collision events is bouncing. For large values of the Weber number the outcome is coalescence and for the largest achievable values of the Weber number the droplets would coalesce, the coalesced drop would form a flat disc which would eventually break up into two separate drops and one small satellite drop. This behavior with increasing values of the Weber number was shown before for droplets in air by Qian and Law [68]. Droplet collisions in a liquid are thus similar to droplet collisions in air. In case of a stationary outer liquid the value of the Weber number at the boundary between bouncing and coalescence is approximately $We_{II,III} = 20$. In case of bouncing the interaction time was found to be equal to the theoretical drop oscillation period as derived by Miller and Scriven [57] and the drainage time was found to decrease with increase of the Weber number.
For droplet collisions in a turbulent outer flow ($Re_\lambda = 141$) on average collisions only lead to coalescence for values of the Weber number larger than 30 ($We_{II,III} > 30$). The external flow is thus of significant influence on the outcome of droplet collisions in terms of bouncing or coalescence. A possible part of an explanation for this hindered coalescence is the fact that a compressional flow in the direction of the collision axis induces an internal drop flow which counteracts film drainage.

Samenvatting

Druppelbotsingen in turbulentie: een experimentele studie

– Gosse Oldenziel –

Druppels komen veelvuldig voor in de natuur en spelen een belangrijke rol in veel industriële toepassingen. Een van de eigenschappen die druppels onderscheidt van vaste deeltjes is hun vermogen om samen te gaan bij een botsing. Dit wordt ook wel coalescentie genoemd. Coalescentie van druppels is van belang in bijvoorbeeld de voedselindustrie. Hier zorgt uitstel van coalescentie in bepaalde emulsies voor een verlenging van de houdbaarheid van het betreffende product. Ook bij voortstuwing door middel van raketboosters, waar de brandstof en de oxidator apart worden ingespoten en ontbranden bij het samengaan, in de halfgeleiderindustrie, waar druppels gesmolten tin worden belicht door een laser en daarbij extreem ultraviolet licht produceren, en bij de vorming van regen speelt coalescentie een rol. Wat niet altijd gerealiseerd wordt, is dat coalescentie niet de enige mogelijke uitkomst van een botsing is, ook het terugstuiteren van beide druppels is mogelijk.

In de meeste van de genoemde gevallen spelen de botsingen zich niet af in een stationaire omgeving, maar in een omgeving die stroomt ten opzichte van de druppels, of een omgeving die zelfs turbulent is. Het doel van de huidige studie is het onderzoeken van het effect van turbulentie in de omgeving op de uitkomst van een botsing tussen twee druppels.

Als twee druppels botsen lijkt het misschien alsof de druppels in contact zijn, maar in werkelijkheid bevindt er zich een dunne film van de omgevingsvloeistof tussen de druppels. Als deze film zo dun wordt dat intermoleculaire Van der Waalskrachten een rol gaan spelen, zal er zich een gat vormen in de film en zullen de druppels coalesceren. De dikte waarbij dit gebeurt is in de orde van $\mathcal{O}(60\ nm)$. Als de filmdikte deze grens niet passeert, zullen de druppels terugstuiteren. De tijd nodig om deze dikte te bereiken wordt de leeglooptijd genoemd, $t_{leegloop}$. De tijd gedurende welke de druppels interacteren heet de interactietijd $t_{interactie}$. Een botsing tussen twee druppels lijdt dus tot coalescentie als $t_{leegloop} < t_{interactie}$, anders lijdt de botsing tot terugstuiteren.

Om het leeglopen van de dunne film te onderzoeken is er een experiment uitgevoerd waarbij een druppel siliconenolie los is gelaten in een laag water welke zich onder een laag siliconenolie bevindt. Een dunne waterfilm vormt zich tussen de olie van de druppel en de olie van de bovenste fase. Omdat de interactietijd in de genoemde configuratie altijd langer is dan de leeglooptijd zal de film uiteindelijk altijd scheuren en zal de druppel altijd

samengaan met de bovenste vloeistof.

Om de filmdikte te meten en om de exacte locatie van de vorming van het gat in de film in beeld te brengen is gebruik gemaakt van matching van de brekingsindices en van laser geinduceerde fluorescentie (LIF). De metingen laten zien dat de film een specifieke geometrie vormt. Deze geometrie is dik in het midden en dun in een ring om het midden heen. Deze geometrie wordt ook wel een 'dimple' genoemd. De metingen laten ook zien dat de film sneller dun wordt dan bepaalde simpele analytische modellen voorspellen en dat het dunner worden niet symmetrisch is. De plek waar de film het dunst is, is op een ring rond het midden.

Naast het onderzoeken van de filmdikte, is het van belang druppelbotsingen met een realistische interactietijd en druppelbotsingen in een turbulente omgeving te onderzoeken. Hiervoor is een cilindrische tank ontworpen met een schijf aan de bovenkant en een schijf aan de onderkant, die beide kunnen roteren met een vaste frequentie maar in tegengestelde richting. De stroming tussen twee roterende schijven wordt ook wel een Von Kármán flow genoemd. In het midden van de cilinder is er een klein volume waar de gemiddelde snelheid nul is, maar waar er wel turbulente fluctuaties zijn in het snelheidsveld. Om precies op deze plek druppels te kunnen laten botsen zijn er twee injectiepijpjes geinstalleerd in de cilinder. Druppelbotsingen kunnen worden uigevoerd in een turbulente stroming en in een stationaire stroming en door middel van het gebruik van drie hogesnelheidscamera's kunnen de druppeltrajectoriën in 3D gemeten worden. Het Reynoldsgetal gebaseerd op de Taylor microschaal en de gemiddelde snelheid van de turbulente fluctuaties, genoteerd als Re_λ, is nul voor het stationaire geval, $Re_\lambda = 0$, en in het turbulente geval geldt dat: $Re_\lambda = 141$. In het algemeen is het Reynoldsgetal een maat voor de verhouding tussen traagheidskrachten en visceuze krachten in een stroming.

De druppelbotsingen worden gekarakteriseerd door het Weber getal $We = \frac{\rho_d U^2 D}{\sigma}$ gebaseerd op de dichtheid van de druppelvloeistof ρ_d, de relatieve druppelsnelheid U, de druppeldiameter D en de grensvlakspanning σ. Het Weber getal is een indicator voor de verhouding tussen traagheidskrachten en oppervlaktekrachten.

In het geval van een druppelbotsing in een stationair fluïdum ($Re_\lambda = 0$) geldt dat voor lage waarden van het Weber getal de uitkomst van de botsingen is dat de druppels terugstuiteren. Voor hoge waarden van het Weber getal is de uitkomst coalescentie, en voor zeer hoge waarden van het Weber getal gaan de druppels samen, waarna de gecoalesceerde druppel een platte schijf vormt die op zijn beurt weer uit elkaar wordt getrokken en splitst in twee grote druppels en één of meerdere satellietdruppels. Dit gedrag is eerder geobserveerd door onder andere Qian en Law [68]. Druppelbotsingen in een vloeistof lijken dus op druppelbotsingen in een gas. In geval van een stationaire omgeving is de waarde van het Weber getal op de grens tussen terugstuiteren en coalesceren ongeveer $We_{II,III} = 20$. In het geval van terugstuiteren is de interactietijd ongeveer gelijk aan de druppeloscillatiefrequentie zoals gegeven door Miller en Scriven [57] en neemt de leeglooptijd af met toenemend Webergetal.

Voor druppelbotsingen in een turbulente omgeving ($Re_\lambda = 141$) lijden botsingen gemiddeld pas tot coalescentie als $We_{II,III} > 30$. De externe stroming is dus van significante

invloed op de uitkomst van druppelbotsingen. Een deel van een mogelijke verklaring van de gehinderde coalescentie is dat de gemiddelde horizontale compressionele stroming een stroming in de druppel opwekt die het leeglopen van de film tegengaat.

Chapter 1

Introduction

Probably everyone is familiar with droplets. If it is not via some recipe for a great salad dressing, it can be through our interaction with rain. Industrial applications where drops are encountered range from the semiconductor industry to the food industry to the petroleum industry to the printing industry, to the fuel spray injection industry. In the semiconductor industry a strong pulsed light source is used to expose a tin droplet, which creates a plasma that emits extreme ultraviolet (EUV) light. Due to its very short wavelength this EUV light can be used in optical lithography to create the very small structures which are required on the lower layers of chips. A second application where droplets can be encountered in the semiconductor industry is when applying an immersion lens. An immersion lens is a thin liquid film which is used to improve imaging in order to etch smaller structures. One of the challenges with the immersion lens is to prevent small droplets from spilling from the imersion lens when translating the silicon wafer. These droplets remain on the wafer and can disturb the process. In the food industry knowledge of droplet physics is of importance for the stabilization of emulsions. The petroleum industry is another sector where droplets are often encountered, for example during the removal of water drops which are dispersed in the oil. In the printing industry and the fuel spray injection industry the injection of small droplets is a crucial part of the process.

In a number of the mentioned applications the breakup or coalescence of drops is of major importance. Breakup is important for the immersion lens droplet. Because of the high velocities with which the wafer moves underneath the immersion drop it tends to break up and leave behind smaller drops. These smaller drops prevent further processing of the structures generated on the wafer and thereby reduce the efficiency of semiconductor production. Coalescence, the merging of separate droplets, is of great importance in the food industry, where the coalescence rate is a factor determining the shelf life of certain emulsion type products like margarine, mayonnaise and ice cream. During the formation of rain in warm clouds it is speculated that condensation nuclei grow due to coalescence, until they reach a size where they are large enough to start falling.

In case of droplet collisions there is often a critical value of a collision velocity below or above which there will, or will not, be coalescence. In a number of the mentioned cases,

the flow around the drops is turbulent. The influence of this external turbulence on the critical velocity is largely unknown. The fact that by far not everything about droplet collisions in turbulence is known will not be a surprise to anyone who ended up misled by a dry weather forecast.
The remainder of the current chapter will consist of four sections. First a brief summary of the equations describing fluid flows will be given along with the relevant dimensionless numbers. Section 1.2 is dedicated to the description of the literature on droplet coalescence, droplet collisions and droplets in turbulence. The research goal is stated in section 1.3 and in the final section the outline of the entire thesis is given.

1.1 Physical parameters

The current research focuses on droplet collisions and possible subsequent coalescence. A simplified sketch of two droplets of equal size colliding head-on at relative velocity $U = |U_1 - U_2|$ is shown in Figure 1.1. U_1 and U_2 are the velocity vectors belonging to both drops. The density of the drops is indicated by ρ_d, μ_d is the dynamic viscosity of the drops, the continuous phase liquid is characterized by its density ρ_c and viscosity μ_c, and D_1 and D_2 are the droplet diameters. In the following only collisions with equally sized droplets with a diameter $D = D_1 = D_2$ are considered.

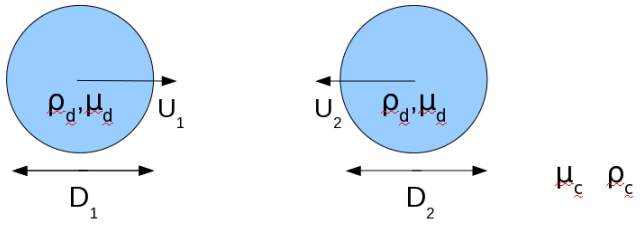

Figure 1.1: Head-on droplet collision. The interfacial tension is σ.

Incompressible fluid flows are described by the mass conservation equation:

$$\nabla \cdot \mathbf{u} = 0, \tag{1.1}$$

the equation describing conservation of momentum, called Navier-Stokes equation:

$$\frac{D\mathbf{u}}{Dt} = -\frac{1}{\rho}\nabla p + \frac{\mu}{\rho}\Delta \mathbf{u}, \tag{1.2}$$

and the relevant initial and boundary conditions. Here, $\mathbf{u}$ and p are the velocity and pressure variables, ρ is the fluid density and μ is the dynamic viscosity. Typical boundary conditions for the velocity are the no slip condition at solid boundaries and the free slip condition at a free surface. Relevant for fluid-fluid interfaces is the jump in pressure as given by the Young-Laplace equation: $\triangle p = \sigma[\frac{1}{R_1} + \frac{1}{R_2}]$, where σ is the interfacial tension

and R_1 and R_2 are the principal radii of curvature of the interface. Also relevant for fluid-fluid interfaces is equilibrium of the shear stress across the interface.
Non dimensionalising the Navier-Stokes equation leads to:

$$We\frac{D\overline{\mathbf{u}}}{D\overline{t}} = -\overline{\nabla}\overline{p} + Ca\overline{\Delta}\overline{\mathbf{u}}. \tag{1.3}$$

Here, We denotes the dimensionless Weber number and Ca denotes the Capillary number. They are defined as:

$$We = \frac{\rho_d U^2 D}{\sigma}, \tag{1.4}$$

and

$$Ca = \frac{\mu_d U}{\sigma}. \tag{1.5}$$

Quantities with an over line indicate dimensionless quantities, $\overline{\mathbf{u}} = \mathbf{u}/U$, $\overline{p} = pD/\sigma$, $\overline{t} = tU/D$, and for the spatial dimensions: $\overline{x} = x/D$, $\overline{y} = y/D$ and $\overline{z} = z/D$. The Weber number can be viewed as an indicator of the balance between inertial and surface tension forces and the Capillary number as the ratio between viscous and surface tension forces. For a droplet collision of given fluids, the fact whether the collision is inertia dominated or viscous dominated is determined only by the diameter and relative velocity of the droplets. In a plot of U versus D the boundary between these regimes will be the line where $Re \approx 1$, where Re is the droplet Reynolds number defined as:

$$Re = \frac{\rho_d U D}{\mu_d}, \tag{1.6}$$

note that $Re = We/Ca$. In the case that $Re \ll 1$, viscous forces dominate, in case $Re \gg 1$, inertia dominates. For viscous droplet collisions the Capillary number is used as dimensionless velocity, for inertial droplet collisions, the Weber number is mainly used. In Figure 1.2 the location of four droplet collision experiments in the (U, D)-parameter space is given, along with the line $Re = 1$ for water drops in air and for water drops in a silicone oil. The droplet diameter in these experiments ranges from approximately 70 μm to 8 mm and velocities range from $1 \cdot 10^{-6}$ m/s to 1 m/s. The literature on droplet collisions will be reviewed in section 1.2.
As mentioned, the analysis presented above is a simplified one. Gravitational forces are neglected and the viscosity of the continuous phase, denoted by μ_c will in practice play a role in the form of the ratio of viscosities $\lambda = \mu_d/\mu_c$. In chapter 2 both gravitational forces and the influence of the ratio of viscosities will be taken into account. Also the concept of added mass is not mentioned, one is referred to the work of Kim and Longmire [42] and Clift et al. [21] for further details. Nevertheless it will become clear that both the Weber number and the Capillary number will be important in the description and understanding of droplet collisions and coalescence.

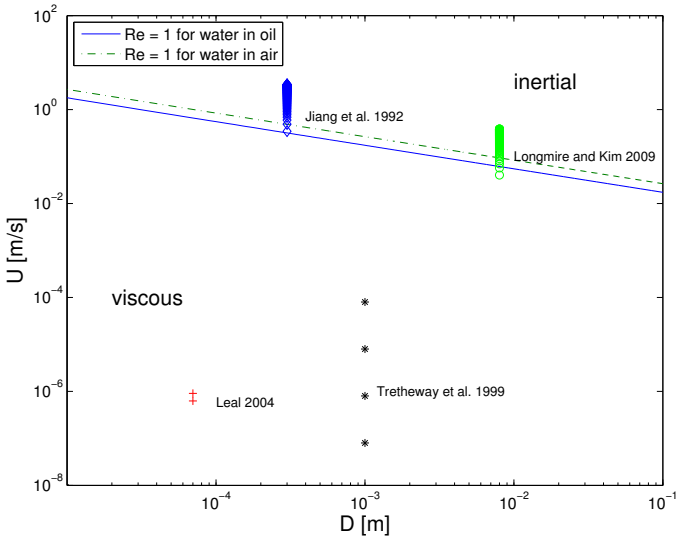

Figure 1.2: Location in (U, D)-space of measurements as described in Jiang et al. [39], Leal [52], Kim and Longmire [42] and Tretheway et al. [80]. The points are to be interpreted as a qualitative indication.

1.2 Droplet coalescence, droplet collisions and droplets in turbulence

In this section the current knowledge on droplet coalescence is discussed, along with a selection of works on droplets in turbulence. The selection is made to highlight possibly relevant methods of measurement and to obtain insight in current topics of interest for droplets in turbulence. Droplet coalescence can be roughly divided into four sub processes, see Chesters [19]. The first sub process is the approach of the drops; during this approach a thin film forms in between the drops. The drainage of this film further decreases its thickness, which is the second sub process. When the film reaches a thickness at which non hydrodynamic, forces such as the intermolecular Van der Waals force become relevant, film rupture will be initiated (sub process three). Initiation of the rupture process has been reasoned to occur due to thermal fluctuations [4]. The thickness at which this can occur for oil-water systems was measured to be around 60 nm, see Burrill and Woods [18]. The final sub process is the confluence of the droplets.
There exists a strong similarity between drop collision and a drop at a two-fluid interface. Because a drop at a two-fluid interface can be interpreted as a small drop that is being forced by gravity towards a large drop, this configuration can be a relevant model for a collision of two drops. A review of work on the case of a drop at a two-fluid interface is given in subsection 1.2.1. In subsection 1.2.2, droplet collisions will be discussed. Finally, in section 1.2.3, a selection of relevant works on droplets in turbulence is discussed. In all subsections the experimental and numerical work is treated separately. One important remark is that it is assumed throughout this work that there are no surface active agents, or

surfactants, present that can also cause surface tension gradients and that can immobilize interfaces. The section is concluded with a short summary.

1.2.1 Droplet at two-fluid interface

It is often stated [19, 43] that two colliding drops coalesce if the time it takes for the thin fluid film in between the drops to drain is smaller than the time it takes for the drops to interact. A natural way to describe coalescence is thus in terms of the following two mechanisms and their associated time scale:

1. the film drainage mechanism and drainage time scale $t_{drainage}$, and
2. the droplet interaction and the interaction time scale $t_{interact}$.

Coalescence occurs when $t_{drainage} < t_{interact}$. In order to investigate the drainage time one can employ the buoyancy driven rise of a drop or bubble towards a two-fluid interface as a model problem. This is attractive because one has an estimate for the interaction force, due to buoyancy, and one can measure the time until coalescence occurs ($t_{drainage}$). In principle the interaction time is infinite in this case, $t_{interact} \to \infty$. Two points need to be mentioned before the bulk of the work is reviewed.
In the literature on droplets at two-fluid interfaces, one can encounter statements about an "equivalent radius principle" [12, 19], where, quoting Chesters [19], "the equations governing (axisymmetrical) drainage between unequal particles are the same as those between equal particles of equivalent radius, R_{eq}, given by $2/R_{eq} = (1/R_1 + 1/R_2)$" (with the word *particles*, Chesters refers to droplets). This principle is assumed to hold if the contact area between two colliding drops is much smaller than the radius of the drops, which according to Chesters [19] is broadly satisfied for collisions leading to coalescence. It could thus be the case that the film drainage behavior for a drop at a two-fluid interface is the same as that for a collision between two drops. In chapter 4 results of droplet collision measurements are presented in which the contact area is not much smaller than the drop radius. It thus appears that the assumption by Chesters does not seem to hold in the reported measurements.
The second point of attention is on the importance of the Bond number for the drop in the two-fluid interface problem, where the Bond number is defined as:

$$Bo = \frac{(\rho_c - \rho_d) g R^2}{\sigma}, \tag{1.7}$$

where ρ_c and ρ_d are the densities of the continuous phase and the dispersed phase respectively, g is the gravitational acceleration, R the volume-equivalent droplet radius, defined as

$$R = \left(\frac{3Vol}{4\pi} \right)^{\frac{1}{3}}, \tag{1.8}$$

where Vol is the drop volume and σ the interfacial tension. Princen [67] was the first to document the geometry of the drop in a two-fluid interface problem. Solutions of

the differential equations describing the geometry are tabulated in this work. This was done for 35 values of a dimensionless parameter that uniquely describes the geometry. It is mentioned that this dimensionless parameter is a single-valued function of what is currently named the Bond number. Although the Bond number is not named in the article, a parameter with the same definition as the Bond number is also tabulated, hereby Princen links the geometry of the problem uniquely to the Bond number. The change in geometry with Bond number is sketched in Figure 1.3, as taken from Howell [36].

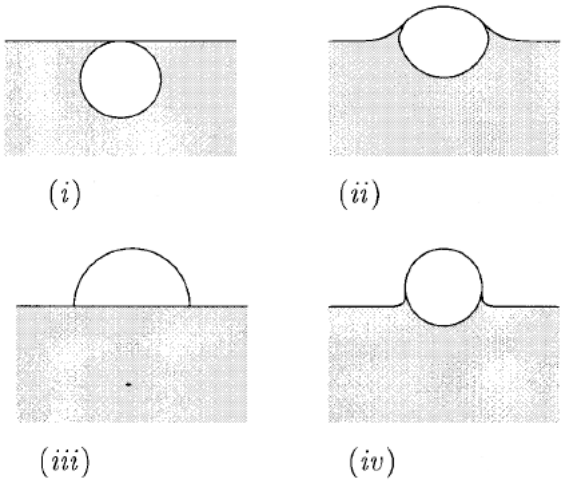

Figure 1.3: Schematic of the variation of bubble shape with Bond number, as in Howell [36]. *(i)* $Bo = 0$, *(ii)* $Bo > 0$, *(iii)* $Bo \to \infty$, *(iv)* impossible.

It can be noticed from Figure 1.3 that at small Bond numbers, $Bo \approx 0$, the interface between the bottom and the top fluid is straight and the drop is spherical. When the Bond number increases, $Bo > 0$, the radii of curvature of the top and the bottom of the drop increase where the radius of curvature of the top increases slower than that of the bottom, and the drop is no longer spherical. If the Bond number approaches infinity, $Bo \to \infty$, the drop shape approaches a half sphere with a flat bottom.

Experimental work For the measurement of the thickness of the thin fluid film between the drop or bubble and the top phase, interferometry is an often used method [18, 24, 44]. Debrégeas et al. [24] find exponential thinning for bubbles in an extremely viscous fluid at a free interface, and they relate the characteristic thinning time linearly to the radius of the spherical cap of the bubble. In their experiment the Bond number was larger than unity. They also investigate the speed at which the film retracts after rupture. Kočárková et al. [44] measure the film thickness for four fluids, among which two types of molten glass (silicate melts) at high temperature in a furnace. They find exponential thinning with a normalized thinning rate that decreases when the Bond number is increased, meaning that the film thins faster when the Bond number is smaller. Employing a relation between

the the area of the spherical cap of the bubble and the Bond number, they propose a simple relation for the thinning rate in terms of the Bond number. Burrill and Woods [18] performed their measurements using different types of oil in water at low Bond numbers and determined that the film ruptures at a thickness of 30 nm to 50 nm. They also found that film thinning sometimes is not axisymmetric. Aarts and Lekkerkerker [3, 2, 4] studied the coalescence of a drop with its bulk phase in fluid-fluid demixing colloid-polymer mixtures. The interfacial tension in these systems is 10^5 to 10^7 times lower than in molecular fluids, while the behavior is analogous to molecular fluids in different aspects. Using transmission light microscopy and laser scanning confocal microscopy they observed that for low viscosity ratios, like for bubbles, the rupture of the film initiates at a central location, whereas for high viscosity ratios rupture initiates off-center [3]. Here the viscosity ratio is defined as: $\lambda = \mu_d/\mu_c$, where μ_d and μ_c are the dynamic viscosities of the dispersed phase and the continuous phase respectively. In other work the focus was on the speed at which the film retracts after film rupture takes place [2]. It is reasoned that this speed is determined by surface tension and can be slowed down by viscous forces or inertial forces, depending on the Reynolds number. Striking in this work is that measurements for coalescing drops are compared to measurements for a drop at an interface. In very insightful work, Aarts and Lekkerkerker [4] image thermally induced capillary waves using a regular camera in real space. It is shown that in the colloid-polymer mixtures the initiation of film rupture happens due to the observed thermal capillary waves. This is different from molecular fluids, where this initiation is expected to occur due to Van der Waals forces. In these measurements the Bond number is approximately one, $Bo \approx 1$. Mohamed-Kassim and Longmire [58, 59] and Ortiz-Dueñas, et al. [63] used particle image velocimetry (PIV), tomographic particle image velocimetry (TPIV) and refractive index matching to determine two-dimensional and three-dimensional velocity fields inside and outside the drop. In these measurements the drop was composed of a mixture of water and glycerin and the continuous phase of silicone oil. The Bond number (based on drop radius, and not diameter as in the reference) in these measurements is on the order of one, $Bo \approx 1.1$ and $Bo \approx 1.7$ and the viscosity ratio is smaller than one, $\lambda \approx 0.3$ and $\lambda \approx 0.14$. Next to the quantification of the velocity fields, it is observed that the rupture of the film initiates off center. Bordoloi and Longmire [14] investigated the effect of neighbouring drops and differently wetted solid particles on the rupture location and found that rupture typically initiates near the lowest vertical position of the drop.

Numerical and modeling work An often used method for the simulation of the film thickness is the boundary integral method (BIM) [20, 86]. This is likely due to the fact that the ratio of spatial scales to be solved requires very large DNS simulations to resolve the film thickness with at least multiple cells. The boundary integral method for Stokes flow gives the velocity at desired locations as integrals of the Green's functions over the boundaries of the flow [49, 66]. This can be computationally less expensive than a DNS, although its application range is limited (often there are severe requirements on the Bond number or on the area of significant excess pressure between the drop and its bulk phase or a second drop

[1]). Boundary integral simulations for droplet coalescence are often performed using either a constant interaction force or a constant approach velocity. The latter is presumably best suited for droplet collisions whereas the former can be an appropriate condition for the droplet at a two-fluid interface. Chi and Leal [20] simulated the rise of the drop towards the interface at different capillary numbers $Ca = \mu U/\sigma$ and ratios of viscosity λ. In the capillary number, σ denotes the interfacial tension and U a characteristic velocity. By choosing the velocity to be the terminal velocity for a drop, $U \sim \triangle \rho g R_{eq}^2/\mu$, this capillary number is equivalent to a Bond number and will also referred to as such. In their work, the rise of a droplet towards a two-fluid interface is simulated for three Bond numbers, $Bo = 0.2$, $Bo = 1$ and $Bo = 10$ and three viscosity ratios, $\lambda = 0.1$, $\lambda = 1$ and $\lambda = 10$. The main result is that the geometry of the film is only dependent on the viscosity ratio and not on Bond number. For the small viscosity ratio, $\lambda = 0.1$, the film is thinnest at the center, in this case drainage is fast. For the intermediate viscosity ratio $\lambda = 1$, the film is of uniform thickness, and for large viscosity ratio $\lambda = 10$, the film shape is called 'dimpled'. This means that the film is thick at the center and has a minimum in thickness at an off-center ring. Drainage of dimpled films is slower than for the uniform and fast drainage cases. Yiantsios and Davis [86] derived long time thinning rates in the limit of small Bond numbers. It is mentioned that for a two phase system involving water, a typical upper diameter for the drop is 10 μm for their analysis to be valid. They analyzed the cases of immobile and partially mobile interfaces, which corresponds to respectively $\lambda \gg \sqrt{R_{eq}/h}$ and $\sqrt{h/R_{eq}} \ll \lambda \ll \sqrt{R_{eq}/h}$, where h denotes the film thickness (in their work they refer to the mentioned interface mobilities as small and fully mobile). In all cases dimple formation is observed, and the long term thinning rate for partially mobile interfaces is approximated as $h \sim t^{-\frac{2}{3}}$. They stipulate that for a fixed value of λ, due to the decrease of h, the interface mobility will increase. All previously mentioned work using the boundary integral method is using the Stokes flow equations in boundary integral form. In more inertia dominated droplet impact phenomena, like for a droplet falling onto a substrate, it might be more appropriate to use a boundary integral formulation for potential flow, as in Bouwhuis et al. [15]. It could be the case that this method is thus applicable for droplet impact with larger deformation. Other simulation methods which are used include the coupled level-set/volume of fluid method, see Coyajee et al. [22] and dissipative particle dynamics, see Iancu [37]. In both works [22, 37], the emphasis is on the dynamics of the impact of the drop at the two-fluid interface.

1.2.2 Droplet collisions

This section concerns a literature review of two colliding drops. As shown in the previous section 1.1, an important parameter for head-on collisions of drops of given fluids is the ratio of inertial forces over surface tension forces given by the Weber number $We = \frac{\rho_d U^2 D}{\sigma}$. If one wants to investigate general droplet collisions that are not head-on, a parameter describing

[1]It appears that the requirements on the Bond number are similar to requirements on the area of contact.

the geometry of the collision, B, referred to as the impact parameter, is introduced. B is defined as the offset χ between the centroids of the drops, perpendicular to the relative velocity vector, normalized by the drop diameter D:

$$B = \chi/D. \tag{1.9}$$

This parameter is zero for head-on collisions and increases to a maximal value of one for grazing collisions. The definition of B is taken as in the work of Ashgriz and Poo [8] and is shown in Figure 1.4.

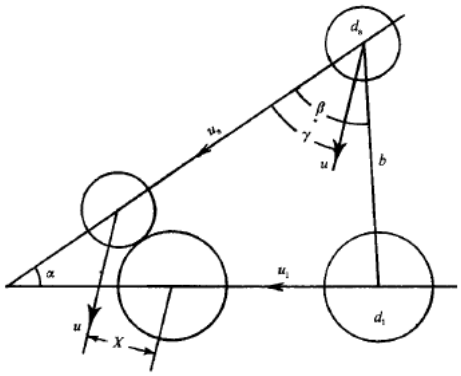

Figure 1.4: Definition of impact parameter B (as in Ashgriz and Poo [8]). The impact parameter is the non dimensional perpendicular distance χ between the relative droplet velocity $\mathbf{U}$ as taken from the the centroid of one droplet, and the centroid of the other drop. Non-dimensionalising χ with the droplet diameter D gives B: $B = \chi/D$.

Experimental work In order to categorize droplet collisions, often regime maps in (B, We)-space are used [6, 8, 16, 39, 68, 76]. An example is shown in Figure 1.5. For example, the interpretation of the diagram in Figure 1.5 is as follows in the head on collision case ($B = 0$). For low inertia, high surface tension collisions, the outcome of the collision will be *coalescence* of the drops, this is labeled as regime I in Figure 1.5. If the Weber number We is increased then at some point the droplets will stop coalescing and the collision will result in *bouncing*. This is regime II. If We is further increased for head on collisions, at some point the drops will again coalesce. This is regime III. If now the Weber number is increased even further, regime IV will be reached. Regime IV, termed near head-on separation by Qian and Law [68], consists of collisions that eventually lead to coalescence, but after severe deformation where the coalesced drop attains a flattened disc shape, the drops break up again due to regained inertia after the disc contracts due to surface tension. A satellite drop appears during separation. This regime is often referred to as *coalescence and reflexive separation*. The remaining regime, number V, only occurs for off axis collisions and is described by *coalescence and stretching separation*, the colliding drops coalesce but maintain enough inertia to separate again afterward. Also satellite drops are formed at separation.

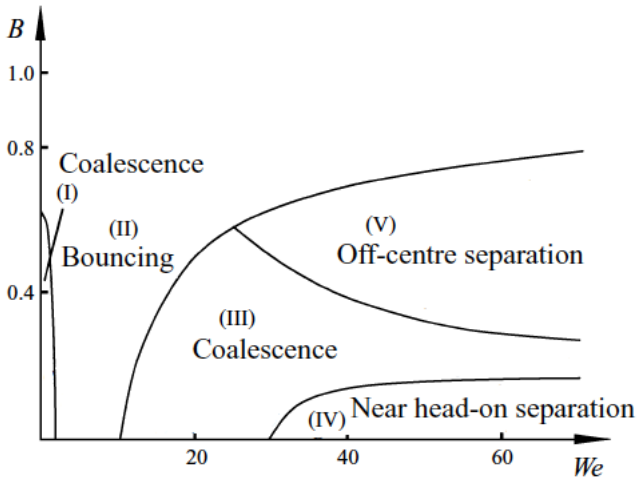

Figure 1.5: Sketch of the regime diagram for binary drop collisions (after in Qian and Law [68]). Values on the axes are typical for collisions of tetradecane drops in a nitrogen environment at a pressure of 1 bar.

A primitive version of a diagram like the one in Figure 1.5 is given by Adam and Lindblad [6]. Brazier-Smith et al. [16] produce similar findings. In these works, as well as in the work of Ashgriz and Poo [8], the system under consideration consisted of water in air or nitrogen. Where Brazier-Smith et al. [16] strictly encounter what is currently understood as regime III (coalescence) and regime V (coalescence and stretching separation), Ashgriz and Poo [8] extend this picture with what is now known as regime IV, coalescence and reflexive separation. It has to be mentioned that the phenomena of regime IV are already imaged in the work of Adam and Lindblad [6]. Around the same time Jiang et al. [39] conduct both binary droplet collisions of water in air and of a number of different hydrocarbon drops in air, and are the first to distinguish the five different regimes as mentioned previously. It was not until the work of Qian and Law [68] that bouncing (regime II) was observed for water drops. In their work [68] the different versions of the regime map for different liquids are unified, and the general diagram as in Figure 1.5 is established. They perform a large number of measurements varying the continuous phase gas composition, the pressure of the gas, the droplet fluid and also the presence of fluid vapor in the gas. It is found that increasing the gas pressure *promotes bouncing for water drops*. At a pressure of 2.7 atm the full five regimes are found for water. If the pressure is increased to 8 atm, bouncing becomes more prominent and the critical Weber number separating bouncing and coalescence (regime II and III) shifts from approximately 5.5 to 13. At this pressure it was not possible to detect regime I anymore. The authors comment on this stating that *"Realistically, of course, two droplets will merge when they are slowly brought together"* [68]. Inverse to the promotion of bouncing for water drops at increased pressure, Qian and Law also found that reduction of the ambient gas pressure for hydrocarbons suppresses bouncing.

Experimental work on droplet collisions at high Weber number, other than the already mentioned work, can be found in Roisman et al. [71], Tang et al. [76] and Willis and Orme [83]. Roisman et al. consider the head-on collision of drops of immiscible fluids in air at atmospheric conditions and consider the drop dynamics after coalescence. For these collisions the result is often coalescence as in regime III of the map by Qian and Law, see Figure 1.5. Also regime IV is observed. Tang et al. [76] investigated head-on collisions of droplets of unequal size. They found that varying the size ratio influences the critical Weber number between the bouncing regime II and coalescence regime III only moderately, whereas the critical Weber number between the coalescence regime III and the coalescence followed by reflexive separation regime IV significantly increases with the size ratio. It is argued that this relative increase of permanent coalescence is enhancing the ignition of gelled hypergolic propellants in rocket engines. Finally, Willis and Orme [83] perform binary droplet collisions of silicone oil drops in a vacuum and encounter similar regimes as those reported by Roisman et al.

All mentioned work on droplet collisions up to now considered liquid drops in a gas or vacuum. A number of droplet collision experiments in a liquid were carried out by Leal et al. [52]. They managed to manipulate the flow in a four roll mill in such way that one injected drop could be broken up into two, which could be made to collide by reversing the flow direction. These collisions, which were already performed at negligible inertia ($We \ll 1$) resulted in coalescence only in case of *gentle collisions*. Kim and Longmire [42] quantified two dimensional flow fields inside colliding droplets and in the continuous phase via the use of Particle Image Velocimetry (PIV) and refractive index matching. In their measurements, droplets only coalesced for large Weber numbers $We \gg 10$. For smaller Weber numbers only bouncing was observed. These measurements hint at the fact that for droplet collisions in a liquid, a similar regime map exists as for droplets in a gas as shown in Figure 1.5. The droplets in the measurements of Kim and Longmire consisted of a mixture of water and glycerol and the continuous phase consisted of silicone oil. Salber and Longmire [72] report that the boundary between bouncing and coalescence for liquid drops in a liquid shifts to larger values of the Weber number when the viscosity ratio is increased.

Experimental work on low Weber number droplet collisions has been described by Bremond et al. [17] Klaseboer et al. [43], Leal et al. [52] (and references therein), Aarts et al. [2] and Paulsen et al. [64]. Bremond et al. [17] studied the coalescence of water drops in hexadecane in a microfluidic flow and concluded that coalescence occurs when the centers of mass of the drops are already separating after impact. They also show that coalescence can be forced even in presence of surfactants, by separating the drops. Application of this research is in the field of emulsification. Klaseboer et al. [43] studied the film thinning process during viscous droplet collision via interferometry in a configuration where two drops, which were still attached to nozzles from which they emerged, could be made to collide by translating the nozzles at a fixed velocity. The Weber numbers in these measurements are extremely small, $We \approx 1 \cdot 10^{-10}$. They compare their measurements to simulations that they also performed and found a good match when comparing with

Stokes flow boundary integral simulations with an immobile interface. This good match is rare and possibly has to do with the way the drops are brought together. Leal et al. built up an extensive repertoire of experiments and simulations with colliding drops [52]. The diameter of the droplets in this work is between 20 μm and 100 μm. As already mentioned they found that colliding drops coalesced only for gentle collisions. Increasing the droplet diameter to $\mathcal{O}(1$ mm) always resulted in Weber numbers too high for coalescence in their device and bouncing occurs. The fluids under consideration are the immiscible polymers polybutadiene for the droplets and polydimethylsiloxane (PDMS) for the continuous phase. A number of researchers are interested in the phenomena that occur after the film has drained and the film is retracting. Aarts et al. [2] measure the speed of retraction of the film and find that there are two regimes. Directly after film rupture the retraction velocity is bounded by viscous forces and set by the capillary velocity and at later times inertia sets the retraction speed. Paulsen et al. [64] introduce a third regime, which they name the *inertia-limited-viscous* regime following an experiment where two droplets hanging from a nozzle are made to coalesce via translation of the nozzles. They state that for coalescing drops to be in the Stokes regime the surface tension force has to be large enough to translate the drop globally. Because during the very initial phase of film rupture the neck circumference is too small to generate a force large enough for a translation of the entire drop, they claim the third regime preexists the viscous and inertial regimes.

Numerical and modeling work By far most numerical simulations on droplet collisions are for low inertia cases via the boundary integral method. This coincides with regime I of the Qian and Law map. Examples are the work by Abid and Chesters [5], Davis et al. [23], Bazhlekov et al. [12], Nemer et al. [60] and Eggers et al. [27]. Abid and Chesters [5] observe dimple formation and approximate the thinning rate by an algebraic relation for partially mobile drops colliding at constant velocity. They obtain the relation $h_{min} = 4.8t^{-1.6}$ for the minimal off center film thickness. Davis et al. [23] obtain the lubrication force between two drops at constant collision velocity for different interfacial mobilities: immobile interfaces $\lambda \gg \sqrt{R_{eq}/h}$, partially mobile interfaces $\lambda \approx \sqrt{R_{eq}/h} \sim \mathcal{O}(1)$, and fully mobile interfaces $\lambda \ll \sqrt{R_{eq}/h}$. Bazhlekov et al. [12] considerably extend previous results by providing a fitted relation for the film thickness in time for all values of their parameter $\lambda^* = \lambda Ca$. Here Ca is the capillary number using the relative droplet velocity as the characteristic velocity. They also show that the geometry of the dimple is different for different values of λ^* and that drainage behavior is sensitive to the outer boundary condition of the film, i.e. a constant velocity case or constant interaction force. It is concluded that more realistic simulations have to be done if one wants to be able to distinguish between coalescence and bouncing based on simulation results, because in reality neither the interaction force nor the interaction velocity are constant. Important is that in all mentioned work, the effect of the outer flow is disregarded. Nemer et al. [60] show that the outer flow does have an influence on film drainage. They compare drops colliding due to body forces in a stationary fluid with drops being pushed together in an extensional flow and conclude that the internal drop stress directed towards the center of the film, caused by the extensional

outer flow, decelerates film drainage significantly. Contrary to an inward stress causing a deceleration of the film drainage, the case of a large drop below a small drop, both rising due to buoyancy forces displays an internal drop stress directed away from the center of the film which causes a fast (exponential) film drainage. In both cases the ratio of viscosities is equal to unity: $\lambda = 1$. Yoon et al. confirm the deceleration leading to entire stagnation of film drainage in their boundary integral simulations of colliding drops being pushed together by the outer flow at a stagnation point [87]. See Figure 1.6 for an illustration of the flow in this case. The rupture behavior of the thin film is also investigated using the boundary integral method. This is done by Eggers et al. [27]. Their main finding is that if two drops coalesce in a viscous fluid, the edge of the retracting film has a thick rim near the hole.

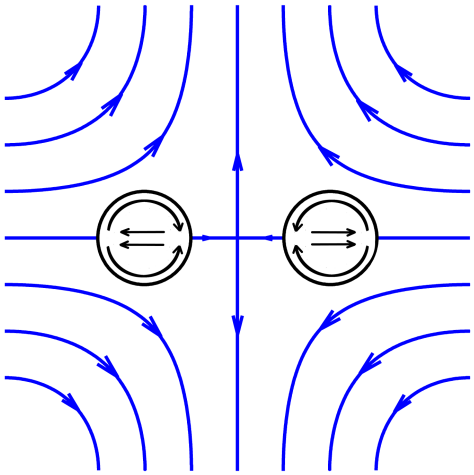

Figure 1.6: Sketch of flow field in case of decelerated drainage as in Yoon et al. [87] and Nemer et al. [60].

It is not unexpected that collisions with higher inertia and thus larger deformation, which could lead to coalescence as in regime III of the map by Qian and Law [68], can not be modeled by the Stokes equations in boundary integral form. As mentioned before, alternatively an approach using a potential flow boundary integral model can be used; see Bouwhuis et al. [15]. Kwakkel et al. [46] use a Coupled Level-Set/Volume-of-Fluid (CLSVOF) method to simulate droplet collisions of tetradecane in air at Weber numbers up to $We = 61.4$. Because it is computationally too expensive to simulate all scales of the flow, a model by Zhang and Law [90] is used to determine the drainage time of the film. This model is briefly discussed later in this subsection. If the correct film drainage time is available, the CLSVOF method can reproduce existing experimental and numerical results. If one wants to predict whether two colliding droplets of given fluids will coalesce, however, the model prediction of the drainage time is not accurate enough according to Kwakkel et al. Iancu [37] simulated droplet collisions in a fluid using Dissipative Particle Dynamics and observed the bouncing (II), coalescence (III) and coalescence followed by stretching separation (V) regimes in the Qian and Law map.

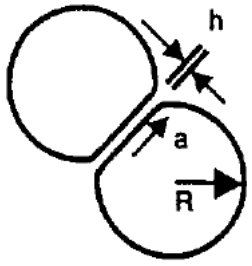

Figure 1.7: Sketch of geometry for parallel disc models for two identical colliding droplets with radius R and separated by a film with thickness h; the area of contact is a disc with radius a (as in Chesters [19]).

A review containing a number of simple analytical models for the modeling of droplet coalescence is given by Chesters [19]. His explanation of the parallel disc models for rigid spheres and drops with different interfacial mobilities are particularly insightful. The words 'parallel disc' refer to the approximation of the area of contact of both drops i.e. the film geometry is thought of as a cylindrical disc with thickness $h(t)$ where t denotes time, see Figure 1.7. These models lead in most cases to algebraic relations for the decrease in film thickness with time except for fully mobile interfaces, like for gas bubbles in a liquid, where exponential thinning is expected. For droplet collisions with a constant interaction force and immobile interfaces the thickness decreases according to $h^* \sim 1/t^{*1/2}$, while for partially mobile interfaces the thickness decreases according to $h^* \sim 1/t^*$. Here, h^* and t^* are the scaled dimensionless film thickness and time. The viscosity ratio of the two fluids enters in parallel disc models via the boundary conditions. In case of fully mobile interfaces, the flow between the drops can be approximated by a plug flow while in case of immobile interfaces the flow would be a Poiseuille flow, and for intermediate interfacial mobilities it would be a superposition of both. A significant modeling effort was done by Zhang and Law [90]. They approximate head-on colliding drops by truncated spheres and derive a system of nonlinear ordinary differential equations that can be solved in order to obtain the film thickness during the collision of fluid droplets in a gas. Remarkable in this model is that the outcome of collisions appears to be predicted well in terms of a coalescence or a bouncing event for water drops and hydrocarbon drops at higher and lower gas pressures. An interesting test case for this model could be the collisions of drops of liquid in another liquid, rather than a gas, as continuous phase.

1.2.3 Dispersion, break-up and coalescence of droplets in turbulence

There is a large amount of work on droplets and particles in turbulence. Much of this work is focusing on the dynamics of particles or drops through statistical methods. For a recent

review see Toschi and Bodenschatz [79]. An example of experimental work on droplets in turbulence can be found in a paper by Gopalan et al. [30]. In this work, the trajectories of thousands of oil drops rising in a locally isotropic turbulent flow are measured via in-line holography. The turbulent diffusion coefficient of the drops is determined for various turbulence levels. It is observed that the turbulent diffusion coefficient of the drops is lower than that of the fluid at low turbulence intensity and higher than that of the fluid at high turbulence intensity.

A classical work on break-up of droplets in turbulence is that of Hinze [35]. In this work Hinze derives a maximal droplet diameter by equating inertial and capillary forces via a critical Weber number, where the velocity in this Weber number is taken to be a typical turbulent velocity fluctuation in the inertial subrange over a distance D: $\overline{v^2} = C_1(\epsilon D)^{2/3}$, see Batchelor [11]. Here D is the droplet diameter, ϵ the turbulent dissipation rate, and C_1 a constant. The critical diameter, often referred to as the Hinze diameter, is defined via the following relation:

$$D_{max}\left(\frac{\rho_c}{\sigma}\right)^{3/5}\epsilon^{2/5} = 0.725. \tag{1.10}$$

For a droplet with $D = 1$ mm to break up due to turbulent velocity fluctuations in a liquid-liquid dispersion typical dissipation levels of approximately $\epsilon = 2.35$ m^2/s^3 are thus required.

In devices like stirred tanks and extraction columns that contain dense suspensions it can be of importance to understand break-up and coalescence in order to predict and possibly prevent for example phase inversion events. A typical phenomenological way to model coalescence and break-up is via the use of drop-eddy collision rates and breakage efficiencies, and drop-drop collision rates and coalescence efficiencies, see for example the work of Tsouris and Tavlarides [81]. In stirred tanks, break-up mostly occurs near the impeller region. The modeling of coalescence in the work of Tsouris and Tavlarides [81] is as follows. The rate of film thinning is approximated by the model mentioned in section 1.2.2, and the interaction force is taken proportional to the mean-square velocity difference at either ends of the eddy: $F \sim \rho\overline{v^2}a^2$ where a is some appropriate length (for example the radius of the parallel disc). Also the interaction time is approximated by this model. If the colliding drops are in contact long enough for the film thickness to become thinner than 50 nm they are considered to coalesce. Cumulative volume fractions versus drop diameter plots of the model prediction match reasonably well with measurement results. The fact that such coarse models produce results that match measurements reasonably well is surprising, this may indicate that the collisions occurring in stirred tanks occur at low inertia.

Measurements in a stirred tank by Tobin et al. [77] focused on coalescence by first setting the impeller velocity to a very large value in order to break the droplets up to small diameters, where after the impeller speed is put to a small value and the measurement is started. Transient drop size distributions are measured by inspecting samples using a microscope. It is found that larger drops coalesce more often than small drops.

Recently Wunsch et al. [85] performed simulations of droplet coalescence in homogeneous

isotropic turbulence for droplets at five values for the Stokes number. In the DNS coupled with Lagrangian particle tracking coalescence was modeled to occur for every drop collision, a behavior typical for non grazing collisions of water droplets in a cloud for example. They found that the highest coalescence rate occurs for intermediate Stokes numbers and explain this by reasoning that for droplets with these Stokes numbers preferential concentration occurs which promotes coalescence. The way in which coalescence is monitored is via variation in time of drop size distribution.
Eastwood et al. [26] investigated the break-up of liquid injected in a submersed jet. In this way it is ensured that the break-up is due to turbulence. Their main conclusion is that the break-up frequency scales with passage frequency of large scale turbulent structures which is contrary to the idea that break-up results from interaction with turbulent velocity fluctuations over a distance comparable to the droplet diameter.

The current state of knowledge on droplet coalescence can now be summarized as follows:

- given a collision of droplets of any fluid in any continuous phase, there exists yet no general model that can accurately predict whether the droplets will coalesce or bounce.

- Droplets of water in air at atmospheric conditions will generally coalesce upon collision at moderate values of the Weber number, whereas hydrocarbon droplets tend to bounce.

- In general there are two kinds of permanent coalescence: (1) the kind where inertia is negligible, $We \ll 1$, and (2) the kind where inertia is significant, $We \sim \mathcal{O}(1)$.

- Statements like "coalescence is favored for gentle collisions (collisions where the radius of interaction a is much smaller than the radius of the droplets R: $a \ll R$)" are not valid for collisions with significant inertia $We \sim \mathcal{O}(1)$. This might indicate that the word "gentle" is defined as: $We \ll 1$.

- Simulations of droplet coalescence using the boundary integral method for Stokes flow, neglecting the large scale drop and outer flow, are only likely to agree with measurements in case of artificial collisions (where the drops are still attached to a nozzle, $We \ll 1$). Boundary integral simulations using a potential flow model might be of interest for the description collisions with significant inertia, $We \gg 1$.

- For droplet collisions with low inertia, there is evidence of significant influence of the large scale drop and outer flow on the drainage of the film and thus on the outcome of a collision.

- Droplet collisions in turbulence have only been investigated via measurements and simulations of cumulative size distributions and thus not on the level of individual collisions.

1.3 Research goal

As mentioned previously, droplet coalescence in turbulent flows is of significant practical and scientific interest. However, to the best of the author's knowledge, there is not any experiment that investigates this at the level of individual drops. With this in mind, the goal of the current work is stated as:

to quantify the effect of turbulence on droplet collisions at the level of individual drops, with particular focus on the prediction of the outcome of the collision in terms of bouncing or coalescence, for given values of the Weber number We and the alignment of the drop velocities, quantified by the impact parameter B.

Throughout this thesis the framework as described by Qian and Law [68] is kept in mind. Because of the thorough flow field quantification inside the colliding droplets and in the continuous phase in the work of Kim and Longmire [42], this work will adopted as a guide for the experimental approach.

Two experiments are described in this thesis. In order to examine film drainage, a droplet at a two-fluid interface is investigated and results are compared to the parallel disc model. In order to quantify the influence of turbulence in the continuous phase, an experiment was designed where droplet collisions in turbulence are be compared with droplet collisions in a stationary continuous phase. Quantification of the potential change in crossover Weber number between the regimes of bouncing and coalescence regimes is of special interest.

Novel in the current work is the application of refractive index matching in combination with laser induced fluorescence (LIF) to quantify film thickness and the determination of the location of film rupture. Next to this the application of 3D droplet tracking to droplet collisions has never been done before. In addition the study of individual collisions in a turbulent continuous phase is unique. To the best of the author's knowledge the presentation of droplet collisions in a liquid in the (B, We)-parameter space has never been published in a scientific journal, although one occurrence in a conference proceeding exists, see Kim and Longmire [41].

Inherent to experimental research are certain choices made to achieve the goal. The main purposeful limitations in the current work are now summarized. For the measurements of the drop at the two-fluid interface the main limitation is the fact that film thickness below 50 μm can not be measured. For the droplet collision experiments the focus will be on head on collisions. The reason for this choice is the mechanical difficulty to design and build an experiment which is optically transparent, has rotating parts inside the facility, and of which the nozzles are translatable. Secondly the measurements will be performed using droplets of one liquid, a silicone oil, at one drop size D and one ratio of viscosities λ. The Reynolds number based on the Taylor micro scale and the velocity fluctuations of the continuous phase, Re_λ, will be varied. Thirdly the requirements for the fluids to be reasonably pure and without contamination, especially by possible surface active agents, demand renewing the continuous phase liquid regularly which also leads to the fact that the

3D droplet tracking system must be calibrated equally often. The time this takes together with the large amounts of data (typically 4 GB of image data per collision), cause that the number of recorded collisions will be in the order of $\mathcal{O}(100)$.
Now a hint of the main results is presented. For the drop at the two-fluid interface it will be shown that due to a non axisymmetric phenomenon the accuracy of the drainage time predicted by the parallel disc models is low. The film shape is a so called dimple and film rupture initiates at the thin ring of the dimple. For the droplet collision measurements it is shown that four of the five regimes of collision outcomes existing for droplets in a gas also exist for droplets in a liquid, namely the four regimes at Weber numbers larger than one: $We > 1$. Two of these have, to the best of the author's knowledge, never been reported before in literature for droplets in a liquid. *Droplet collisions in a liquid are thus similar to droplet collisions in a gas.* It is also shown that the continuous phase flow has a large influence on the collision outcome, in the current research the critical Weber number between bouncing and coalescence (regime II and III) will increase, thus promoting bouncing. Finally it is shown that the time the drops interact $t_{interact}$ is equal to the droplet oscillation time, and the time until film rupture, $t_{drainage}$, decreases with increasing Weber number.

1.4 Outline of thesis

The remaining four chapters of this thesis are organized as follows. First in chapter 2, film thinning for a droplet at a two-fluid interface is investigated. It will be shown that the geometry of the film is thick at the center with a thin ring around it. This is referred to as a dimple. This film shape is also expected to occur in case of colliding droplets. In chapter 3 the experimental approach is explained for the measurement of colliding droplets. The turbulent flow in the experimental setup is quantified using particle image velocimetry (PIV) and the drop detection via image processing and the droplet tracking are explained. Measurements of droplet collisions in a stationary continuous phase and droplet collisions in turbulence are the subject of chapter 4. In this chapter the measurement results will be presented and discussed. Conclusions resulting from the comparison between droplet collisions in a stationary liquid with droplet collisions in a turbulent liquid are also given. In the final chapter, chapter 5, conclusions are drawn in a broader sense. Droplet collisions in a liquid will be compared to droplet collisions in a gas.

Chapter 2

Measurements of liquid film thickness for a droplet at a two-fluid interface

Abstract

Coalescence of a droplet at a two-fluid interface is studied at Bond numbers larger than one and at three different values of the viscosity ratio. Both the thickness of the liquid film between the rising droplet and the two-fluid interface, and the location of film rupture are measured using Laser Induced Fluorescence. Particle Image Velocimetry was applied to the flow in the film. It is found that the film thins asymmetrically, and that the time interval between collision and film rupture is shorter than predicted by commonly used models. The film ruptures at an off-center location. It can be concluded that asymmetric film drainage speeds up coalescence.

2.1 Introduction

Coalescence and breakup of droplets of fluid dispersed in a second fluid continues to be of interest. Dispersants speeding up the break up of large portions of oil in the Gulf of Mexico in the 2010 oil spill were used in large amounts, while micro organisms further break down the oil. In studies of situations like this, knowledge of droplet break-up, and its counterpart, coalescence, is required. Coalescence will be the subject of investigation in this work. Two types of configurations are mostly used for coalescence investigations: (i) two colliding droplets and (ii) a droplet at a two-fluid interface. A sketch of a droplet at a two-fluid interface is shown in Figure 2.1. Via the equivalent radius principle these two cases are equivalent [19], where the equivalent radius, R_{eq}, is given by:

$$\frac{1}{R_{eq}} = \frac{1}{2}\left(\frac{1}{R_1} + \frac{1}{R_2}\right), \tag{2.1}$$

This chapter is based on G. Oldenziel, R. Delfos and J. Westerweel, *Measurements of liquid film thickness for droplets at a two-fluid interface.* Phys. Fluids **24**, 022106 (2012)

where R_1 is the radius of the first drop and R_2 the radius of the second drop, which is infinite in case of a two-fluid interface. If one wants to predict whether two approaching drops will coalesce, one has to know whether the time scale of drainage of the liquid film between the drops is smaller than the interaction time scale. In case of a droplet at a two-fluid interface, the time scale of interaction is always larger than the time scale of the draining of the thin film, so coalescence will always occur. If this requirement on the time scales is met, it is generally accepted that when the film reaches a thickness which is of the order of tens of nanometers, intermolecular Van der Waals forces will come into play and initiate rupture of the film [19]. For describing the process of film-thinning, a number of models

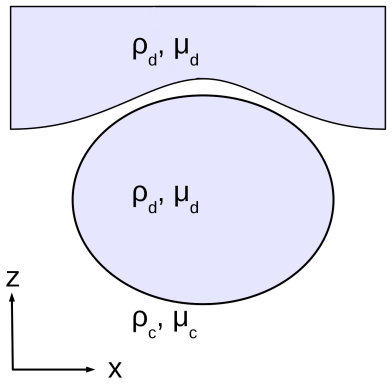

Figure 2.1: Droplet at a two-fluid interface, with $\rho_d < \rho_c$ and a viscosity ratio $\lambda = \mu_d/\mu_c$.

exists. In all models an important parameter is the ratio of viscosities $\lambda = \mu_d/\mu_c$, where μ_d is the viscosity of the dispersed phase and μ_c that of the continuous phase. Generally, three situations are considered for the thin film, denoted as 'fully mobile' ($\lambda \ll 1$), 'immobile' ($\lambda \gg 1$), and 'partially mobile'. In case of partial mobility the ratio of film thickness h to droplet radius R is of importance along with the viscosity ratio. For partially mobile films it holds that $\lambda\sqrt{h/R} \approx 1$, see for instance Davis et al [23]. The interface mobility will determine to a large extent the flow in the film. If the flow is a lubrication flow, i.e. the pressure is constant over the height of the film, the flow can be considered at any location as a superposition of a Poiseuille flow and a plug flow. The balance between these is determined by the boundary conditions. In the boundary conditions, λ plays a significant role through the equilibrium of the shear stress at the two-fluid boundaries. Davis et al. [23] solve the lubrication approximation of the governing equations outside of two drops moving toward each other at constant velocity and employ a boundary integral technique to solve for the flow inside the drops. They determine the pressure in the film, which they integrate to find the hydrodynamic interaction force. The shape of the film is important, because it is coupled to the pressure distribution in the film through the local curvature. Here, with shape we mean the radius of the (axisymmetric) disc where the film is thin and the radial profile of its thickness. Yiantsios and Davis [86] employ a numerical model to solve the fully coupled flow in the film and in the drop to predict the shape of the thin film

in time. For a large range of viscosity ratios with $\lambda \geq 1$, the shape of the thin liquid film can be described as a pocket of fluid surrounded by a thin ring, referred to as a 'dimple'. Yiantsios and Davis [86] also derive relations for the behavior of the minimum film thickness with time, the results of which show astonishing agreement with the predictions of simple parallel disc models [19]. A convincing approach to unify the modeling of the partially mobile case and the immobile case, as separately described in Yiantsios and Davis [86], has been attempted by Bazhlekov et al. [12] They consider (i) the case of a constant force driving the drops together and (ii) the case of a constant approach velocity. In a combined experiment and modeling effort, Klaseboer et al. [43], found good agreement between the film drainage between two drops and their lubrication model. They concluded that the interface was immobile and explained this by assuming that surfactants were present. Furthermore they observed that sometimes the initially axisymmetric drainage became unstable and resulted in a non-axisymmetric drainage. This same observation was made by Burrill and Woods [18], who performed a large number of interferometric measurements on droplets coalescing at a two-fluid interface. Asymmetric drainage for a liquid drop at a liquid-liquid interface is also mentioned by Hartland and Robinson[33]. In all models mentioned where the film shape is not imposed to be parallel, the long term behavior is that the film thins in a symmetric way, maintaining the dimple shape. For small values of λ ($\lambda \ll 1$), Chi and Leal [20] show that a dimple does not develop and that the location of minimal film thickness is in the middle of the film. Because the film will rupture at the location of minimal thickness, it can be expected that the rupture of the film will initiate at the center for $\lambda \ll 1$. Experiments by Aarts and Lekkerkerker [3] show that indeed for gas bubbles the film ruptures more symmetrically than for liquid drops. At least one example of a movie by Miessner et al. [25, 56] of film rupture at the center of the film, at $\lambda = 0.03$, is known to the authors. Further work was done by Ortiz et al. [63], who quantified three-dimensional velocity fields for the coalescence of one and two droplets at a two-fluid interface by means of high-speed tomographic Particle Image Velocimetry (PIV) [29]. It was observed that the thin fluid film ruptured off-center at $\lambda = 0.14$.
All mentioned publications that were specifically aimed at measuring or modeling the thinning of the film were performed at Bond numbers $Bo < 1$, where the Bond number is defined as the ratio of gravity forces to surface tension forces:

$$Bo = \frac{(\rho_c - \rho_d) g R^2}{\sigma}. \tag{2.2}$$

Here ρ_c and ρ_d are the densities of the continuous phase and the dispersed phase respectively, g is the gravitational acceleration, R the droplet radius, and σ the surface tension. Burrill and Woods [18] reach values of Bo between 0.0052 and 0.042, and for the measurements of Klaseboer et al. [43] the Bond number is approximately $Bo = 0.2$. In the numerical work of Yiantsios and Davis [86], it is assumed that $Bo \ll 1$ and through a normal stress balance on a near spherical drop at a two-fluid interface it can be derived that the condition $d_{film} \ll R_{eq}$ used by Bazhlekov et al. [12] is equivalent with the requirement that $\sqrt{Bo} \ll 1$ if the interaction force is supplied by gravity. Here, d_{film} denotes the radius of the disc that represents the film.

The first main goal of the current work is to investigate the process of film drainage through measurement of the film thickness for a range of viscosity ratios and to compare this with existing models in terms of geometrical behavior and time it takes to coalesce. Determination of the location of rupture of the film is the second research goal. Both were done for droplets with a Bond number larger than one.
To measure the film thickness, the interferometric method only works well when the change in film thickness is of the order of several wavelengths of the light. For larger changes in thickness, this technique is inappropriate. In this work the film thickness is analyzed under these circumstances and the location of film rupture is determined, both through the use of laser induced fluorescence (LIF). The film thickness is investigated from a side-view, while the rupture location is determined from a top view. PIV is applied to the flow in the film from a top view in order to quantify flow velocities and the effect of the presence of PIV seeding particles on the location of film rupture initiation is investigated. In order to apply an optical method like LIF, the two-fluids need to have equal refractive indices. This was achieved by refractive index matching. All measurements were done for three different values of the viscosity ratio, that is $\lambda = 0.95$, 2.5 and 7.1.
In a review article, Chesters [19] mentions a number of simple analytical models describing the drainage of the thin liquid film between two droplets. They are referred to as 'parallel disc models', because the film is approximated by a flat disc of fluid. The specific models that might be applicable in the current work are referred to as 'drainage between deformable immobile interfaces', and 'drainage between deformable partially-mobile interfaces'. Two kinds of models are encountered: (i) models where the velocity of the droplets during the collision is constant, and (ii) models that assume a constant interaction force. Here, the part of the drainage process of interest is that where the buoyancy force on the droplet is approximately constant. That is why the constant interaction force case will be adopted. The force is denoted by F and is supplied by gravity. $h(t)$ denotes the liquid film thickness and t time. Then the film thickness for drainage between deformable immobile interfaces shows the following behavior:

$$h^2(t) \sim \frac{3\mu_d R_{eq}^2 F}{16\pi\sigma^2}\frac{1}{t}. \tag{2.3}$$

Here, R_{eq} is the equivalent radius as defined in 2.1. For deformable and partially-mobile interfaces the result of the modeling of the film thickness is:

$$h(t) \sim \left[\frac{\pi\mu_d F^{1/2}}{2\left(\frac{1}{2}\pi\sigma/R_{eq}\right)^{3/2}}\right]\frac{1}{t}. \tag{2.4}$$

Both models assume that:

$$h/h_0 \ll 1, \tag{2.5}$$

where h_0 denotes some initial film thickness. A second assumption is that the radius of the disc that represents the film, d_{film}, is much smaller than the equivalent radius of the drops:

$$d_{film} \ll R_{eq}. \tag{2.6}$$

This chapter is structured as follows. After the introduction there are sections on the experimental approach, a section with results and a section where conclusions are drawn. The section on the experimental approach and the section with the results are subdivided in three subsections, one for each measurement. These are an LIF measurement with a view from the side, an LIF measurement with a view from the top and a PIV experiment also with a view from the top. The section on the experimental approach starts with a general description.
In the next section the three experimental configurations are explained. The accuracy of the film thickness measurement, the refractive index matching, the determination of the rupture locations, and the PIV parameters are described. It will be shown that the measurement technique can only be used to measure down to a film thickness of approximately $h \approx 30$ μm. The processing of the LIF data is also explained. The results of the measurements are presented after the section on the experimental approach. The main observations are that the drainage process is not symmetric, that the film ruptures quicker than symmetric models predict and that the film ruptures off center. Conclusions are summarized in the final section.

2.2 Experimental approach

The first main research goal involves a measurement of the film thickness using LIF from a side view of the droplet. The second involves a measurement using LIF while viewing the droplet from the top. To measure flow velocities PIV was applied from a top view. In this section the matching of the index of refraction of both fluids and a brief analysis on the error of the film thickness measurements is presented as well as an explanation of the experimental set-ups. Both the side view and the top view measurements were conducted in a transparent tank in which a layer of silicone oil was floating on top of a layer of water mixed with glucose syrup. The glucose syrup was added to the water to match the refractive indices of the two working fluids. Drops of silicone oil were released from below by a computer controlled syringe pump (Hamilton 500B) through a nozzle. The exact dimensions of the tanks, nozzle, layers of fluid and other parameters for the side view and top view experiment can be found in Table 2.1. The drops were released close to the interface, approximately $4R$ below it. This resulted in the smallest variation in impact location so that the field of view (FOV) could be chosen such that the entire droplet could be imaged at the highest possible magnification. In this way also the behavior will be closest to that described by the constant force model. The measurements were performed with three different types of silicone oil, namely Wacker AK5, AK20 and AK50, where the number stands for the kinematic viscosity in mm^2/s at 20 °C. The measured values for the density ρ, viscosity μ, surface tension σ, and refractive index n for the three different viscosities are given in Table 2.2.
To minimize optical distortions, the refractive index n of the water/glucose syrup mixture was matched to that of the silicone oil. It is possible to change the index of refraction of a liquid by adding a miscible other liquid with a different index of refraction [34]. In this way

Table 2.1: Experimental set-up parameters for side view and top view experiment.

	side view measurement	top view measurement
Tank dimensions (l×w×h) (mm^3)	$50 \times 50 \times 600$	$93 \times 93 \times 120$
Height water/glucose syrup layer (mm)	150	50
Height oil layer (mm)	25	13
Nozzle diameter (mm)	3.5	4
Distance between nozzle and interface (mm)	13	13
Imaging frequency (Hz)	7.55	600

Table 2.2: Fluid properties as measured for the two-fluids at all viscosity ratios at 25 °C. Density was measured using a Brand density bottle and a Servo Berkel Prior scale, viscosity using a Contraves low shear 40 rheometer, refractive index using an Abbe refractometer and the interface tension using the method as described by equation 3.5 in Aarts and Lekkerkerker [3]

.

	Viscosity ratio λ		
	0.95	2.5	7.1
Silicone oil	AK5	AK20	AK50
Density ρ (kg/m^3)	917 ± 4	947 ± 4	956 ± 4
Dynamic viscosity μ $(mPas)$	5.5	17.7	51.1
Refractive index n $(-)$	1.396 ± 0.0005	1.400 ± 0.0005	1.402 ± 0.0005
Water/glucose syrup mixture			
Glucose syrup mass fraction ϕ $(-)$	0.47	0.50	0.51
Density ρ (kg/m^3)	1169 ± 4	1169 ± 4	1179 ± 4
Dynamic viscosity μ $(mPas)$	5.8	7.0	7.2
Refractive index n $(-)$	1.396 ± 0.0005	1.400 ± 0.0005	1.402 ± 0.0005
Interface tension σ (N/m)	0.021	0.018	0.019

not only the index of refraction will be altered, but also the density and the viscosity of the mixture of the two-fluids. Miessner et al. [56] used two mixtures, one for each phase in their experiment, so that they could choose the viscosity ratio next to matching the refractive indices. In the current experiment, this is not the case and the refractive index of the mixture is matched to that of the oil, yielding a large range in λ at approximately constant μ_c. Despite this loss of a free parameter, the viscosity ratios attained in this experiment, $\lambda = 0.95$, 2.5 and 7.1, are better suited for comparisons with numerical simulations that utilize an immersed boundary method to represent the liquid/liquid interface [22]. The refractive index was measured using an Abbe refractometer. Within two decimal places it can be described by as $n = 1.33 + 0.16\phi$. The deviation from this correlation is systematic in concentration and temperature, and is shown in Figure A.1 in appendix A, where ϕ is the glucose mass-fraction of the water-glucose mixture. A rheometer (Contraves low shear 40) was used to measure the viscosity of the mixture at $T = 298$ K at different glucose syrup mass fractions, see Figure A.2 in appendix A. The measured values for the refractive indices of the silicone oils AK5, AK20 and AK50 were respectively $n = 1.396$, 1.400 and 1.402. When using the fitted polynomial at $T = 298$ K this leads to corresponding mass fractions of glucose syrup of $\phi = 0.47$, 0.50 and 0.51 respectively. After the mixture was prepared, the index of refraction was measured and if necessary water or glucose syrup was added to fine tune the index matching. In total this would change the mass fraction by no more than 3% of its initial value.
In order to distinguish the two-fluids from each other, a small amount of fluorescent dye is added to the heavier fluid. Laser induced fluorescence is used to obtain measurements of the film thickness between the oil droplet and the continuous oil layer. Approximately 0.004 g of fluorescent dye (Rhodamine B) is added to the total amount of 700 ml of water/glucose syrup mixture. If the fluorescent dye is illuminated by a laser with a certain wavelength the dye emits photons of a larger wavelength. Mounting an optical long pass filter on the camera ensures that the water/glucose syrup mixture will appear bright in the obtained images and the oil will be dark.

2.2.1 Side view LIF measurements

The drainage of the liquid film is recorded from the side by means of a CCD camera (LaVision ImagerIntense) with a 1376×1040-pixel 12-bit image format. It was operated at a frame rate of 7.55 Hz. The objective (Nikkon Micro-Nikkor) has a focal length of $f = 105$ mm and was used with a $f^{\#} = 5.6$ aperture stop. An optical long-pass filter (Schott OG570) with a cut-off wavelength of 570 ± 6 nm was mounted on the objective. A vertically oriented laser sheet makes it possible to generate images of a slice through the middle of the drop. A frequency-doubled (532 nm) pulsed Nd:YAG laser (New Wave Solo PIV III) illuminates the field of view. Via three mirrors and two lenses the laser beam is formed into a sheet. The minimum laser sheet thickness is less than 1 mm and is located above the nozzle. The dimensions of the field of view are 12.6×9.5 mm^2. A sketch of the experimental set-up is shown in Figure 2.3.

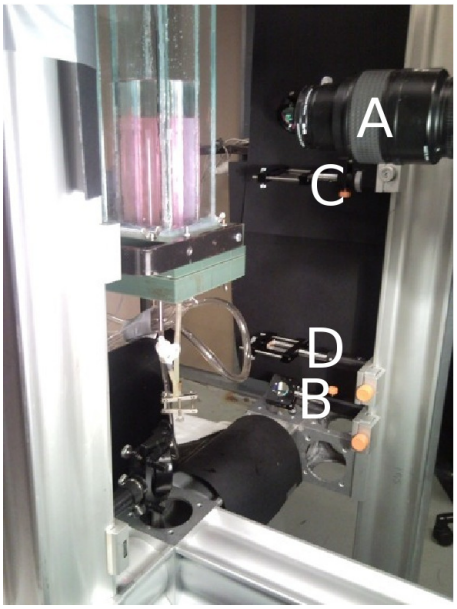

Figure 2.2: Experimental set-up. In the top right the objective (A) can be seen, one mirror (B) and two lenses (C and D) can also be seen. The water phase is bright pink.

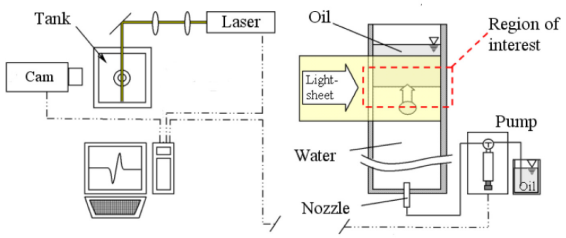

a: top view b: side view

Figure 2.3: Schematic representation of the experimental set-up. Left: top view. Right: side view.

Using LIF to detect the thickness of films that are in the order of tens of μm is not ideal. Because of the finite thickness of the laser sheet the thickness of the film will always be overestimated. As shown in Figure 2.4, the error ϵ can be written in terms of the radius of curvature of the top of the droplet a and the laser sheet thickness Δz_0 as:

$$\epsilon = a - a\cos\left(\arcsin\left(\frac{\Delta z_0}{2a}\right)\right) \approx \frac{1}{8}\frac{\Delta z_0^2}{a}. \tag{2.7}$$

Entering conservative values of: $a = 4.5$ mm and $\Delta z_0 = 1$ mm yields: $\epsilon = 0.028$ mm. The minimal measured thicknesses were approximately 0.03 mm so this is consistent with the estimate. From an optical point of view the smallest scale that can be detected is the

diffraction-limited spot diameter d_s, defined on the image as:

$$d_s = 2.44\,(1 + M_0)\,f^{\#}\lambda, \tag{2.8}$$

where M_0 is the magnification, $f^{\#}$ the f-number, and λ the wavelength of the light. In these measurements, typical values for the optical parameters were: $M_0 = 0.7$, $f^{\#} = 5.6$ and $\lambda = 580$ nm, so $d_s = 13.5$ μm, which is slightly larger than two pixels. Consequently, no significant information appears to be missed because of averaging over pixels.

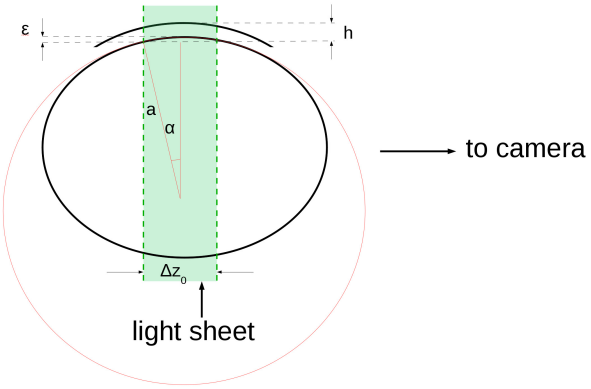

Figure 2.4: Side view perpendicular to camera view. Δz_0 is the light sheet thickness, a is the radius of curvature at the two-fluid interface as defined by Aarts and Lekkerkerker [3].

Figure 2.5 shows a typical image set obtained for $\lambda = 0.95$. From the LIF images the film thickness was determined at each time step by a method based on the determination of the locations of the maximum and minimum of the gradient of the signal. The distance between these is taken to be the film thickness h. Five basic steps describe this method:

1. First a circle is fitted to the top of the droplet using a least squares method. The image is then interpolated linearly on radial lines starting at the center and extending to 1.1 times the radius $r = a$. Angles between $-50\,^\circ$ to $50\,^\circ$ with the vertical are included in the measurement. In Figure 2.6 the angular range is depicted. In this Figure also the definition of the distance along the film d is depicted, which is zero at the top of the droplet. The step size in angle was chosen to be smaller than one pixel on the arc.

2. The background signal (i.e. the domain of the image not containing a fluorescent signal) is approximated by a fifth order polynomial, based on the signal outside a 70 pixel region centered around the maximum value, and subtracted from the signal.

3. In order to smooth the signal, it is expanded in a Fourier series via a Fast Fourier Transform, and the coefficients corresponding with a wave number larger than $k_{\text{cutoff}} = \frac{2\pi}{\lambda} = 310/\text{mm}$ are put to zero. This eliminates high frequency noise.

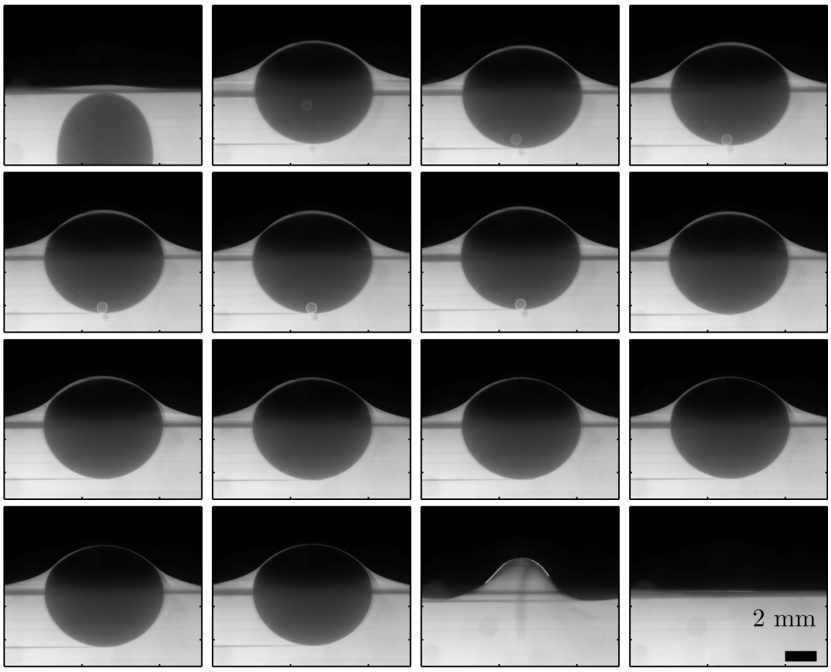

Figure 2.5: Example of typical raw data at $\lambda = 0.95$. One out of every two images is shown with a delay of $\Delta t = 0.265$ s between subsequent images. One big and several small satellite drops can be observed inside the large drop.

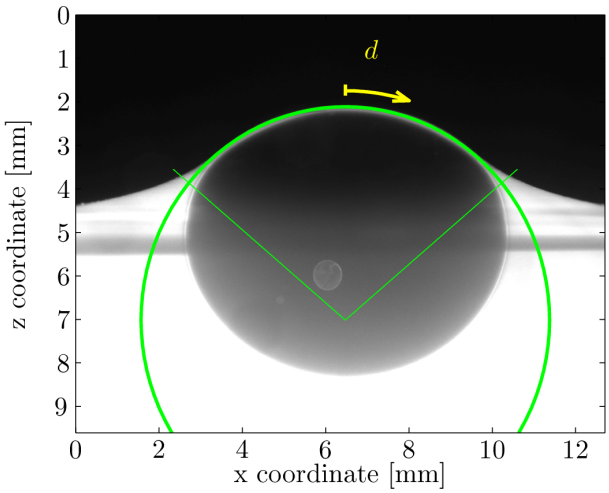

Figure 2.6: Raw image with fitted circle and leftmost and rightmost radial lines for maximum gradient method and definition of coordinate d.

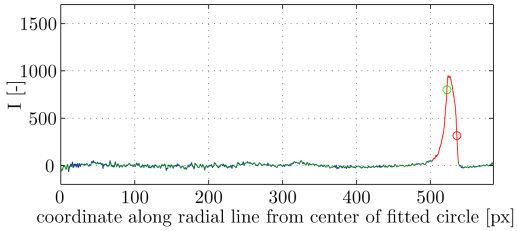

Figure 2.7: Example of a typical signal minus background with detected maximum and minimum gradients.

4. For radii larger than $0.75a$ and image gray values higher than $I = 50$ the maximum and minimum gradients are now determined by the approximation $\frac{\partial I}{\partial r}|_{r+\frac{1}{2}\Delta r} \approx \frac{I(r+\Delta r)-I(r)}{\Delta r}$, where Δr is the size of the mesh in radial direction. The film thickness h is now the distance between the location of the maximum and the minimum. See Figure 2.7 for a typical detection.

5. To detect the film thickness on the next frame the fitted circle is translated along with the droplet via a detection of the droplet position in the new image based on thresholding.

The entire data set for the side view measurement consisted of 11, 13 and 15 droplets for $\lambda = 0.95$, $\lambda = 2.5$ and $\lambda = 7.1$, respectively. Droplets that floated out of focus entirely due to asymmetric behavior, which is described in 2.3.1, were excluded. Due to the finite accuracy of the refractive index matching there always remains a thin shadow near the top of the film, which causes difficulties to detect the film thickness, see Figure 2.8. Before

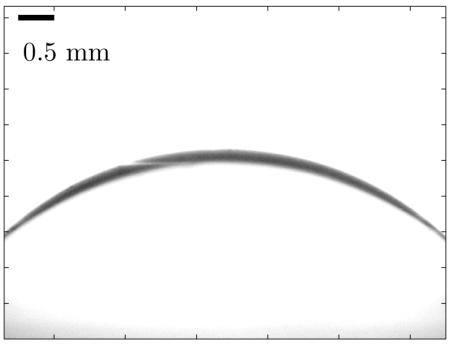

Figure 2.8: Close up of inverted raw data around the thin shadow in the film at the top of the droplet just left of the center.

an experiment was performed the setup would be cleaned thoroughly. When performing the next experiment it was observed that during a number of minutes the droplets would coalesce immediately after which the behavior would change to the one described in this work. This behavior was also observed by Burrill and Woods in the third part of their work [18]. Table 2.3 shows the various experimental parameters. The volume of the droplets was determined by assuming them to be rotationally symmetric ellipsoids, the major and minor axis of which were determined manually. The radius R is defined as the radius the droplet would have if it were a sphere with the volume of the ellipsoid.

Table 2.3: Experimental parameters for side view measurement.

	Viscosity ratio λ		
	0.95	2.5	7.1
Droplet radius R (mm)	3.6	3.8	3.8
Bond number Bo $(-)$	1.46	1.7	1.7
Size data set N $(-)$	11	13	15

2.2.2 Top view LIF measurements

In the top-view measurement a horizontal laser sheet illuminated only the part of the droplet and liquid film that is slightly above the initial interface level. For a sketch see the left part of Figure 2.9. For details of the experimental parameters and set-up see Table 2.1. The rupture process was filmed from the top with a high-speed camera (Photron APX-RS) at a frame rate of $f = 600$ Hz. The camera has a 10 bit CMOS sensor array with a resolution of 1024×1024 pixels, where the pixel size is 17 μm. The circular buffer functionality of the camera was used in order to capture the rupture events. This means

that images were recorded sequentially, where each new frame overwrites the oldest frame, until the acquisition is stopped. For the top view LIF measurements the same objective and optical long pass filter were used as in the side view case, and the same aperture stop was used ($f^{\#} = 5.6$). The dimensions of the field of view are 22.2×22.2 mm^2. A high-speed Nd:YLF laser (New Wave Pegasus) was used with a wavelength of 527 nm. The circular laser beam was formed into a horizontal sheet via three mirrors and a negative cylindrical lens. The measurement was performed for the same three viscosity ratios λ as in the side view case, see Table 2.4.

Table 2.4: Experimental parameters for top view measurement with and without tracer particles.

	Viscosity ratio λ		
	0.95	2.5	7.1
Without tracer particles			
Droplet radius R (mm)	3.9 ± 0.1	4.1 ± 0.2	4.2 ± 0.2
Bond number Bo $(-)$	1.7	2.0	2.1
Size data set N $(-)$	5	4	11
With tracer particles			
Droplet radius R (mm)	4.3 ± 0.2	4.4 ± 0.2	4.4 ± 0.2
Bond number Bo $(-)$	2.1	2.3	2.2
Size data set N $(-)$	11	11	5

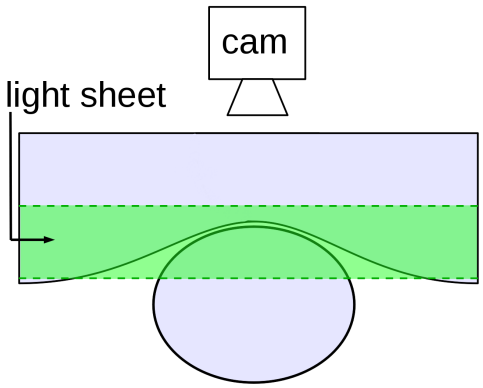

Figure 2.9: Sketch and photo of high-speed top view experiment. Left: sketch (camera not drawn to scale).

The size and position of the droplet at the time of rupture was manually determined. First a circle is fitted to the drop via a least squares fitting method. Hereafter, the location of

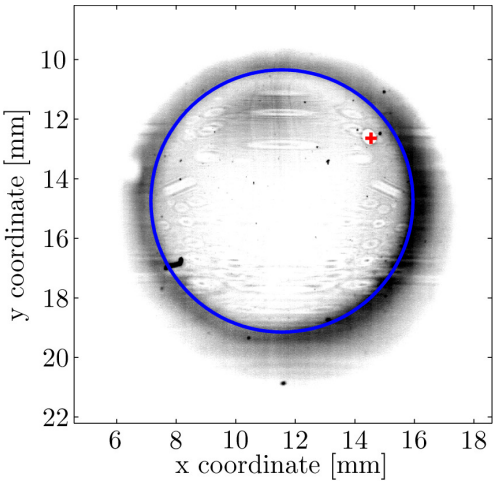

Figure 2.10: Example of a typical rupture location as indicated by the '+ symbol' ($\lambda = 7.1$). The image is cropped around the drop and gray values are inverted. The fitted circle is shown. The nozzle is at the center of the original field of view, so at $(12.1, 12.1)$ mm.

rupture was detected manually. A typical result can be seen in Figure 2.10. The ruptured film initially expands radially from this location.

2.2.3 Top view PIV measurements

In order to apply PIV to the high-speed images, a small amount of tracer particles (Spheri-cell 110 P8 hollow glass spheres) was added to the water/glucose syrup mixture. These particles have an average diameter of 11.7 μm. No optical filter was used, and the aperture was set to $f^{\#} = 11$ to prevent overexposure. The laser was operated at much lower power than for the LIF experiments. The PIV processing was performed by means of commercially available software (LaVision DaVis 7.2). Two values for the time between two frames to cross-correlate were used. For the slow pre-rupture drainage a value of $\Delta t = 1/60$ s was used, while for the rupture itself this was $\Delta t = 1/600$ s. A multipass/multigrid interrogation approach is employed starting with a window size of 64×64 pixel areas and finishing with 16×16 pixel windows with 50% overlap. The velocities were thus resolved with a spatial resolution of 0.18 mm. A circular mask was used such that only the drop region of the image was used for correlation. A median filter was used for validation of the measured data in a postprocessing step.

Table 2.5: Experimental results for side view measurements. Uncertainty margins are estimated standard deviations.

	Viscosity ratio λ		
	0.95	2.5	7.1
Time to coalescence t_{coal} (s)	2.43 ± 0.49	2.60 ± 1.0	4.95 ± 1.42
Minimum thickness location $d_{h_{min}}$ (mm)	3.3 ± 0.1	3.2 ± 0.4	3.5 ± 0.6
$R_{h_{min}}/R_{sm}$ (-)	0.80	0.77	0.81

2.3 Results

2.3.1 Side view LIF measurements

The time before the droplets coalesced, t_{coal}, can be found in Table 2.5 with the measured values for the distance from the center to the location of minimal film thickness $d_{h_{min}}$. Also in Table 2.5 the radial location of the minimum film thickness from a top projection, $R_{h_{min}}$ over the radius of the semi major axis of the droplet, R_{sm}, is given. This is done because it is expected to correspond best to what is observed from a top view. Time $t = 0$ is defined as the first frame where the top of the droplet was above the original interface. Measured values for the time to coalescence are found to increase with λ. Now the time before coalescence occurs will be estimated using the simple parallel film model as described by Chesters [19] and mentioned in section 2.1. This is done for the case of partially mobile interfaces. Entering values representative for the case $\lambda = 0.95$ in equation 2.4 leads to:

$$h(t) \cong \frac{2.32 \times 10^{-6}}{t}. \tag{2.9}$$

If we now, for ease of calculation, assume that the film thickness $h = 2.32 \times 10^{-6}$ m at $t = 1$ s, for which it is assumed that condition (2.5) will hold, it would still take $t = 23.2$ s before the film thickness reaches 100 nm, at which rupture can be expected; see for example Burrill and Woods [18]. This is much longer than what the present measurements indicate. Figures 2.11 and 2.12 show the thickness of the liquid film versus the distance along the film in time for an experiment at $\lambda = 0.95$ where rupture happened relatively late. Due to the thin shadow in the image of the film (see Figure 2.8) the thickness just left of the center is not properly detected. A five point moving average filter was applied to the resulting profiles. In disagreement with the assumption that the drainage process is entirely symmetric, which is assumed in all models mentioned previously, the process is initially symmetrical, but becomes asymmetric after some time. What was observed fits well in the five step drainage as described by Burrill and Woods [18]. The first step is the

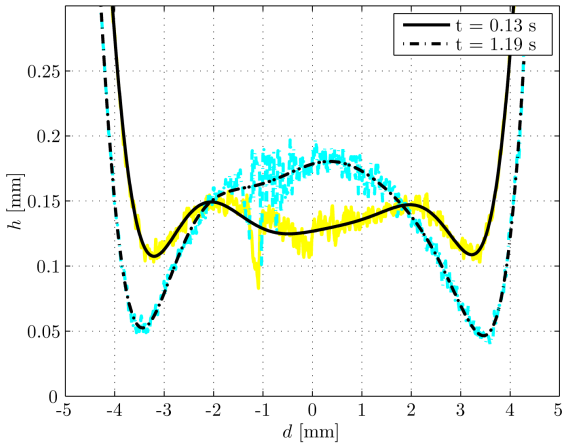

Figure 2.11: Film thickness at start and end of dimple formation. $\lambda = 0.95$. Black lines are the fitted tenth order polynomials to the data which are plotted in light gray (yellow online) and gray (cyan online).

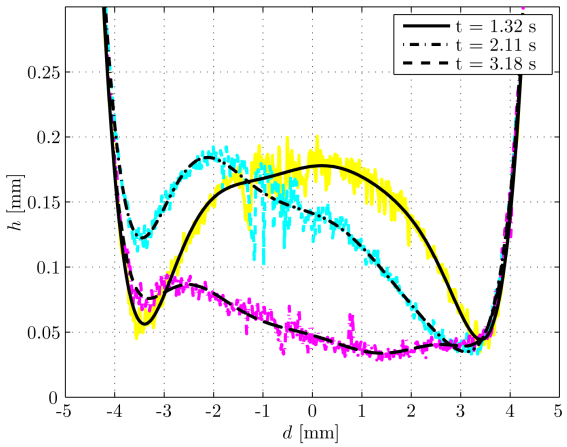

Figure 2.12: Film thickness at start, halfway through and at the end of uneven drainage. $\lambda = 0.95$. Black lines are the fitted tenth order polynomials to the data which are plotted in light gray (yellow online), gray (cyan online) and dark gray (magenta online).

buoyancy-driven approach of the drop to the interface. After the first impact the droplet undergoes a damped oscillation during which drainage sets in. From $t = 0.13$ s to $t = 1.46$ s the formation of a dimple can be observed. See Figures 2.11 and 2.12 for a detailed look at the film thickness at the start and end of this phase. Burrill and Woods [18] describe that during the formation of the dimple, slow even drainage can be observed by noticing the thin ring getting thinner. Thinning of the ring is observed in the current example too. Up until this point everything is still fully symmetric. This dimple formation phase was observed to be symmetric in the measurement plane for every droplet. From $t = 1.6$ s to $t = 3.4$ s, it can be seen that a large parcel of fluid leaves the film to the left, see Figure 2.12. This is the fourth step. It is referred to as uneven drainage. The uneven drainage was also observed experimentally by Klaseboer et al. [43] who report it in a section on miscellaneous observations. In the current measurement, this appears to be purely gravity-driven. A parcel of heavy fluid on top of a droplet of lighter fluid under the influence of gravity will be unstable. In their work, Burrill and Woods [18] investigate the influence of different concentrations of surfactants and also explain the phenomena they observe mainly through a redistribution of surfactants. In the current experiment the phenomenon in its entirety is not expected to be surface tension driven since the Bond numbers are much larger than those considered by Burrill and Woods. The fifth step, the rupture of the film, takes place between $t = 3.44$ s and the next frame at $t = 3.57$ s. The largest Bond number in the work of Burrill and Woods [18] is for the case of toluene drops in water: $Bo = 0.0419$, while the smallest Bond number in the current experiment is $Bo = 1.46$, see Table 2.3. This difference stems mainly from the droplet size. In the mentioned work, the radii of the droplets ranged from $R = 1.1$ to 1.7 mm. The difference for the current measurements, between the different viscosity ratios, was that for the larger values of λ the process would be slower. The five step pattern would be followed until rupture would occur in every case. In most cases rupture would occur during the asymmetric phase. Figure 2.13 depicts the behavior of the film thickness at the left and right minimal values and at the maximum for the same drop as that in Figure 2.11 and Figure 2.12. The values were obtained by approximating the data by a tenth order polynomial. In the same Figure also the location of the maximum thickness, $d_{h_{max}}$, is shown during the phase where one distinct maximum existed. This maximum is found to abruptly shift from a location near the center to a position on the side. The uneven drainage phase was not always as obvious as in the previous case. In a number of cases the fluid parcel sliding off the drop would appear to be symmetric. It is believed that these cases are examples of uneven thinning perpendicular to the measurement plane. An indirect indication for this is that the drop moved out of focus most of the times this occurred. Such movement is evidence for an asymmetry in the direction with a component normal to the laser sheet.

In order to investigate the influence of impurities in the fluids that could change the surface tension, two dimensional direct numerical simulations were carried out by Kwakkel and Breugem [45], using the same method as in Coyajee and Boersma [22]. Their results show that asymmetric drainage will occur without contamination being present if there is a small asymmetry present in the initial condition. In this simulation the droplet was released from

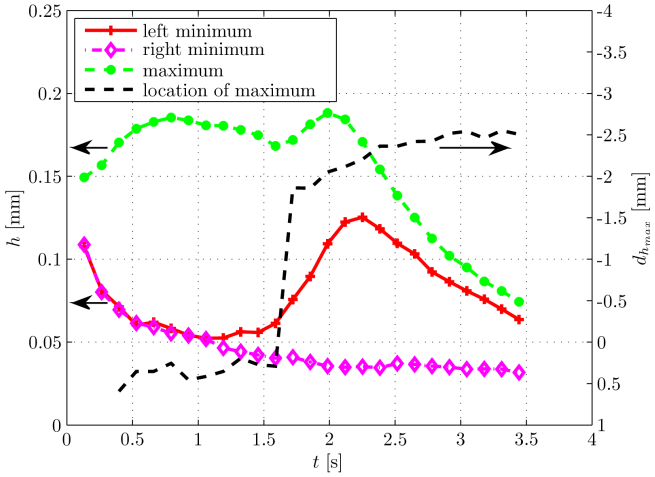

Figure 2.13: Minimal and maximal thickness of film (left axis) and the location of the maximal thickness in time (right axis) for $\lambda = 0.95$.

a horizontal position at 0.99W, where W is the domain half-width. Figure 2.14 shows the result of the application of the LIF processing method as mentioned before, to binary images of the droplet in the water/glucose syrup mixture resulting from the simulation. The asymmetric behavior is present, so it is plausible that in the measurements surfactants are not causing the uneven drainage.

2.3.2 Top view LIF measurements

An example of the rupture of the thin fluid film is shown in Figure 2.15. A hole in the film initiates somewhere off-center, after which the film retracts. During the process of retraction the edge of the retracting film takes the shape of a number of arcs. Trails of fluid are left behind in between the arcs. These trails break up into smaller droplets, reminiscent of the Rayleigh instability [74]. Sometimes two trails merge into one. The small droplets, with diameters around 40 μm, will eventually settle due to gravity and can interfere in the coalescence process. So without exterior contamination the measurement can be disturbed by these small droplets. The number of trails differed in each case and sometimes the edge was entirely without trails. The speed of retraction becomes lower for larger viscosity ratios.
For the determination of the location of rupture without PIV seeding a data set of five, four and eleven droplets was collected for $\lambda = 0.95$, 2.5 and 7.1 respectively. The top part of Table 2.6 summarizes the results. On average, the location of rupture, as determined by hand is at approximately 0.83 times the radius of the drop as observed from the top view. The uncertainty is the root mean square value of the difference of the individual cases with the average location. The minimum thickness of the film as observed from the side occurs at on average 0.79 times the largest horizontal radius of the drop. The data set used for the cases where PIV tracer particles were added consists of eleven, eleven and five

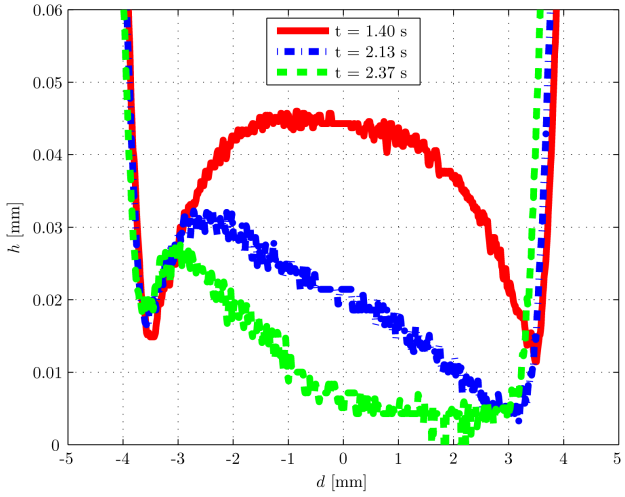

Figure 2.14: Film thickness at start, halfway through and at the end of uneven drainage in a DNS. $\lambda = 0.95$.

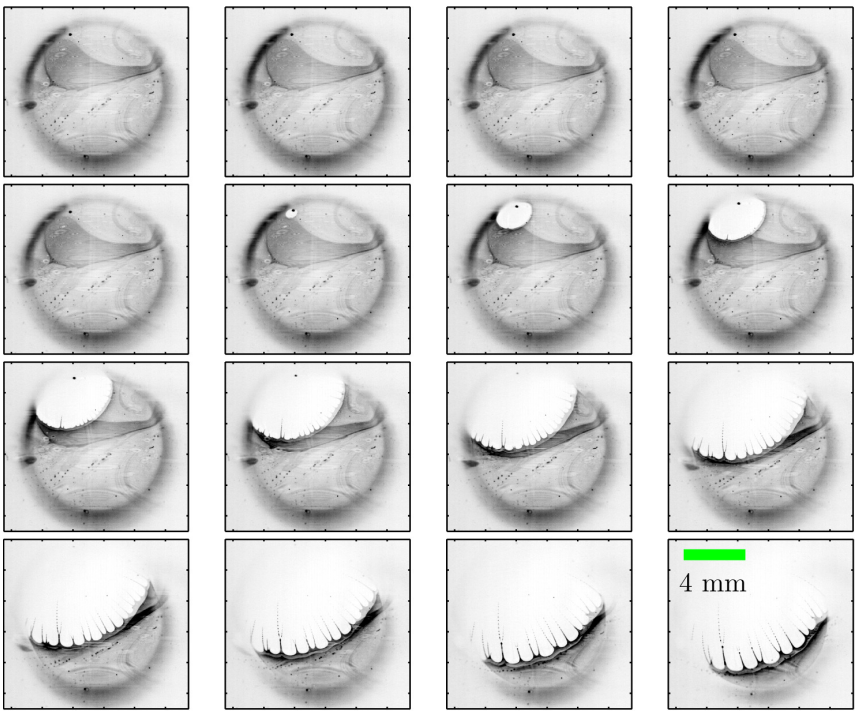

Figure 2.15: Example of the rupture of the thin film for $\lambda = 7.1$. The time between the subsequent frames shown here is 1/300 s (only every second frame from the images that are captured at 600 Hz is shown). The formation of trails of satellite droplets can be observed. The image is cropped around the droplet and the gray values are inverted.

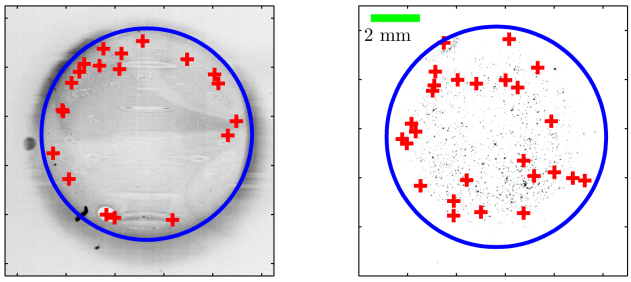

Figure 2.16: All observed rupture locations without PIV seeding depicted on one drop image for the case without seeding (left) and the case with seeding (right). The radii of the rupture locations are scaled with respect to the detected droplet radius. Angular location with respect to the droplet center is unchanged. Because the location in the field of view of the droplets during rupture differed all rupture locations are depicted on one droplet. The image is cropped around this location and the gray values are inverted.

droplets for $\lambda = 0.95, 2.5$ and 7.1 respectively. The results are summarized in the bottom part of Table 2.6. The variation in radial rupture location is much larger in case seeding is added to the fluid. Figure 2.16 shows images where all observed rupture locations are depicted on one image for the two cases. The radial rupture location is scaled with the droplet size, the angular location with respect to the drop center is unchanged. In the raw images of the experiment where tracer particles were added to the water phase, it appears in a small number of cases as though the rupture is initiated at the location of a single seeding particle or an agglomeration of seeding particles.

Table 2.6: Experimental results for top view measurements with and without tracer particles.

	Viscosity ratio λ		
	0.95	2.5	7.1
Without tracer particles			
Rupture radius R_{rupt} (mm)	3.23 ± 0.18	3.27 ± 0.22	3.52 ± 0.29
R_{rupt}/R (-)	0.83	0.81	0.84
With tracer particles			
Rupture radius R_{rupt} (mm)	2.69 ± 0.55	2.85 ± 0.62	3.04 ± 0.70
R_{rupt}/R (-)	0.63	0.65	0.69

2.3.3 Top view PIV measurements

For viscosity ratios of $\lambda = 0.95$, 2.5, and $\lambda = 7.1$ the data set to which PIV was applied consisted of ten, ten and five droplets respectively. Resulting PIV velocity fields for the uneven drainage phase and the rupture itself are shown in Figure 2.17 for $\lambda = 2.5$. It is known that small particles tend to agglomerate at two-fluid interfaces, see Binks and Horozov [13]. Therefore, it is expected that most of the seeding particles to which the PIV correlation was applied are at the upper water/oil interface. In the pre-rupture phase this will slightly underestimate the velocity in the thin film because of the partly parabolic nature of the film flow. It can be observed that the motion is asymmetric in the first subfigure of Figure 2.17. An off-center velocity maximum is present in this subfigure. Maximum velocities during the uneven drainage are in the order of 3 to 6 mm/s. In all cases two velocity minima can be observed on both sides of the location of maximal velocity. This is also the case in Figure 2.17. It appears as though the fluid circulates around these locations. In the majority of cases it was found that rupture of the film initiated at the opposite side of the pre-rupture velocity maximum. This is also the case in Figure 2.17. Initiation of rupture was never observed to be at the velocity maximum. Typical rupture velocities are around 0.2 m/s for $\lambda = 0.95$ and $\lambda = 2.5$ and 0.1 m/s for $\lambda = 7.1$, i.e. up to a factor 67 higher than that of the uneven drainage.

2.4 Conclusions

The first of the two most noticeable results of the side view LIF experiment is that in the film thinning is not necessarily symmetric for viscosity ratios in the partially mobile and immobile regime. From the top view PIV experiment it could be observed that in fact every droplet behaved asymmetrically. In all cases dimple formation occurs in a symmetrical fashion, but quickly the observed asymmetry develops. This is in direct disagreement with all modeling efforts known to the authors, and in agreement with the uneven drainage process as described by Burrill & Woods [18]. It is likely that this is in direct relation with the fact that the Bond number in the current measurements is large. In the derivation of the different models the Bond number is often assumed to be small. In a two-dimensional DNS by Kwakkel and Breugem [45] with a constant surface tension, similar asymmetric behavior was observed. This leads to the conclusion that presence of surfactants is not the cause of the asymmetric behavior.
Using the simple parallel disc model for partially mobile interfaces from Chesters [19], it was shown that the measured time it takes the film to drain is much shorter than that predicted by the model. This is the second noticeable result from the side view LIF measurements.
One of the main results from the top view LIF measurement is that, in absence of PIV seeding, the thin film will rupture near the radial location where it was observed to have a minimal thickness in the side view measurement. When adding PIV seeding it is observed that the locations of rupture are located at much more random radial locations than without PIV seeding. The average diameter of the seeding particles is 12 μm. The fact

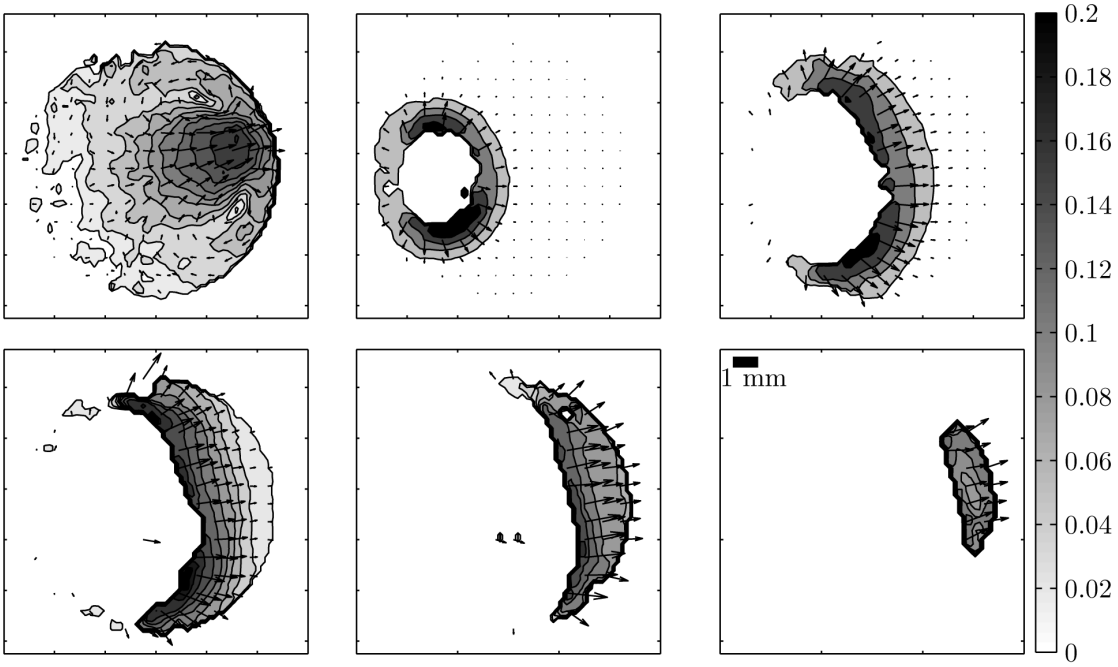

Figure 2.17: Example of a PIV result for $\lambda = 2.5$. Grayscale axis is absolute velocity in m/s. The top left image is during the uneven drainage before rupture. For this single image the scale of the shade bar is from 0 m/s to 3 mm/s, for the other images it is as shown on the right. Only part of the vectors is shown. The time between the second to fifth image is $\Delta t = 4/600$ s. Note that rupture occurs at the opposite side of the location of maximal velocity during the uneven drainage phase.

that the rupture process is influenced by the particles is an indication that the thickness at rupture, without the presence of PIV seeding particles being present, is smaller than 12 μm.

In the top view PIV experiment it was observed that in the majority of cases the film ruptures at the side opposite the velocity maximum during the uneven drainage and never at the location of the velocity maximum.

A recommendation for further research is to perform an experiment where it can explicitly be shown that the asymmetric behavior is due to gravity, so for a range of Bond numbers from $Bo \ll 1$ to $Bo > 1$. It is possible that this will be a measurement using interferometry. In order to predict the time to coalescence, the modeling of the observed asymmetric behavior is also of interest.

Chapter 3

Experimental approach for droplet collisions

3.1 Introduction

Successful experimental studies of the coalescence process require quantitative observations of the collision trajectory and coalescence when it occurs, in a flow that is fully characterized. L.G. Leal, *Phys. Fluids* **16**, APS Award paper, 2004 [52].

In the previous two chapters the current level of knowledge on droplet coalescence was explored and an experiment with a drop at a two-fluid interface is described. One of the conclusions of the experiment is that even in a relatively simple geometry the film drainage time is difficult to predict. This implies that the outcome of a collision of two droplets in terms of coalescence or bouncing is hard to predict. In chapter 1 the research goal was formulated as: *to quantify the effect of turbulence on droplet collisions at the level of individual drops, with particular focus on the prediction of the outcome of the collision in term of bouncing or coalescence for given values of the Weber number We and the impact parameter B.* Because the result from chapter 2 shows that it is not straightforward to perform an experiment that accurately models colliding droplets, a second experiment is conceived where actual droplet collisions can be investigated. The above quote from L.G. Leal indicates the main requirements for the experimental facility in order to quantify the effect of continuous phase turbulence:

- optical accessibility,
- a droplet injection and 3D tracking system, and for the flow a
- fully characterized turbulent flow field.

For the turbulent flow an additional requirement is that the average velocity between the nozzles is very small or zero. This additional requirement originates from the choice to adopt a nozzle approach to droplet injection as in Kim and Longmire [42]. If the average

velocity between the nozzles is not approximately zero, it is not unlikely that potential effects on coalescence are caused by the average flow. In this work it is attempted to prevent this. It is not evident that there is an effect of the continuous phase turbulence before performing the measurements. If there is an effect, a possible cause can be the influence of continuous phase stretching or compression on the film flow through the boundary conditions i.e. the flow inside the drops. The way the mentioned requirements are met is discussed in the current chapter. The results from the subsequent collision experiments are discussed in the subsequent chapter. In the remainder of this chapter first the Von Kármán flow facility is described along with the droplet injection system and the imaging set-up. The flow is characterized using PIV, this is described in section 3.3. In section 3.4 the droplet detection via image processing is described as well as the calibration and the 3D droplet tracking algorithm. The properties of the fluids and the drops is given in section 3.5. Finally, conclusions are drawn and the accuracy of the measurement method is discussed.

3.2 Experimental set-up

Homogeneity is one of the requirements as mentioned in the introduction of this chapter. The central stagnation point makes a Von Kármán flow facility a suitable experimental facility for the present experiments. Flows of this type are often used in turbulence research [70], [69], [48], [47], [82] and [84].
In 1921 Theodore von Kármán showed that the flow above a rotating disc of infinite radius is described by a pair of nonlinear ordinary differential equations that are fully equivalent to the Navier-Stokes equation (1.2). This is the reason that since then, flows above, below or in between rotating discs are referred to as Von Kármán flows. A mathematical review on the subject of these flows is given by Zandbergen and Dijkstra [89]. Batchelor was the first to describe the flow between two infinite discs in exact counter rotation. His solution is shown in Figure 3.1. Batchelor's solution consists of a boundary layer near the discs, solid

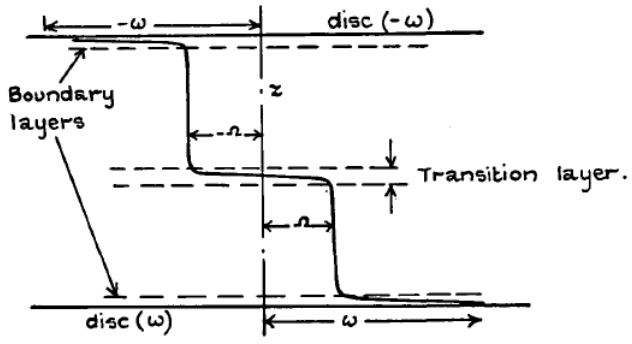

Figure 3.1: Sketch of flow profile between two infinite discs in exact counter rotation, from Batchelor [10].

body rotation in the top and bottom part of the fluid, and a transition layer in between the upper and lower main bodies of fluid. If one considers the confined flow between two discs in exact counter rotation, as conceptually shown in Figure 3.2, the centrifugal pumping of the discs induces a toroidal streamline pattern in both the top and the bottom part of the flow. The two main parts of the flow between two confined discs in exact counter rotation

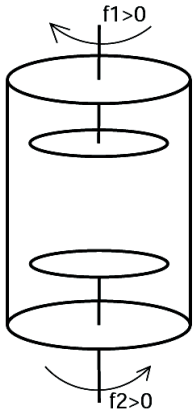

Figure 3.2: Concept of Von Kármán flow facility [69]. In exact counter rotation it holds that $f1 = f2$.

are shown in Figure 3.3. In the following this type of flow is referred to as Von Kármán flow. The flow profiles as shown in 3.3 indicate a central stagnation point.

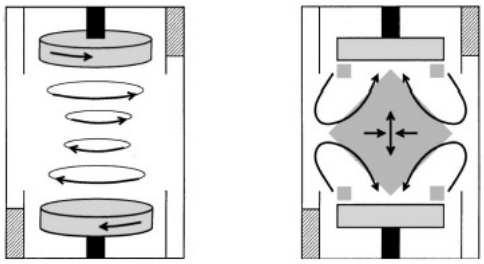

Figure 3.3: Sketch of main flow components. Left: central shear. Right: centrifugal pumping. From La Porta et al. [47].

3.2.1 Von Kármán flow facility

The present facility was based on a modified design as described by Ravelet [69]. The facility is depicted in Figure 3.4 and the dimensions of the core of the facility are indicated in Figure 3.5.
The core of the facility consists of a plexiglas cylinder with an inner diameter of 170 mm and two plexiglas discs of radius 8.3 cm connected to an axle. The hole through which the

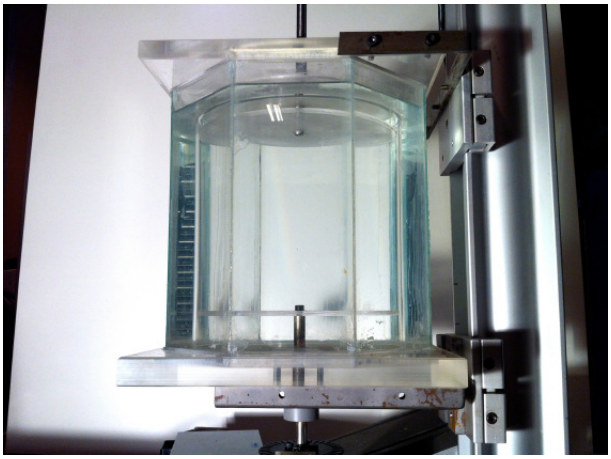

Figure 3.4: Von Kármán flow facility.

bottom axle enters the facility is made water tight with an o-ring and a bearing. In order to be able to image the center of the facility without the optical distortion associated with curved walls, the core is placed in an octagonal glass tank, which can be filled with water. The discs are driven by dc motors. The disc rotation frequency was measured optically by a photodiode and was found to remain constant within 7%. A difference between the presently described Von Kármán flow facility and the facilities described in references [70], [69], [48], [47], [82] and [84] is that no baffles are used on the discs. Ravelet [69] studied the difference between flows driven by discs with baffles and flows driven by discs without baffles and mainly finds that when baffles are used, the main upper and lower bodies of fluid rotate at a higher velocity relative to the discs, than without baffles. Ravelet refers to the flow with the use of baffles as *inertially driven* flows, and to the flow without baffles as *viscous driven* flows. Because the anticipated turbulence levels for the current research are lower than the turbulence levels in the work of Ravelet, no baffles are used here. A second reason not to use baffles is that baffles will cause injected drops to break up into smaller drops which will rise slowly and thus cause problems in the optical detection of drops in the measurement volume.

3.2.2 Droplet injection

The droplets are injected through two nozzles centered around the center of the Von Kármán flow facility as shown in Figure 3.6. The inner nozzle diameter is 3 mm, the outer diameter is 5 mm and the distance between the nozzles is 3.27 cm. A brief exploration of the use of different configurations of fluids and nozzle geometries indicated that the current combination of drop viscosity and volume, nozzle diameter and inter nozzle distance leads to a range in impact Weber numbers that makes the measurement of a change in critical Weber number between bouncing and coalescence possible. Two plexiglas blocks glued to the outside of the core cylinder of the Von Kármán flow facility are used to clamp

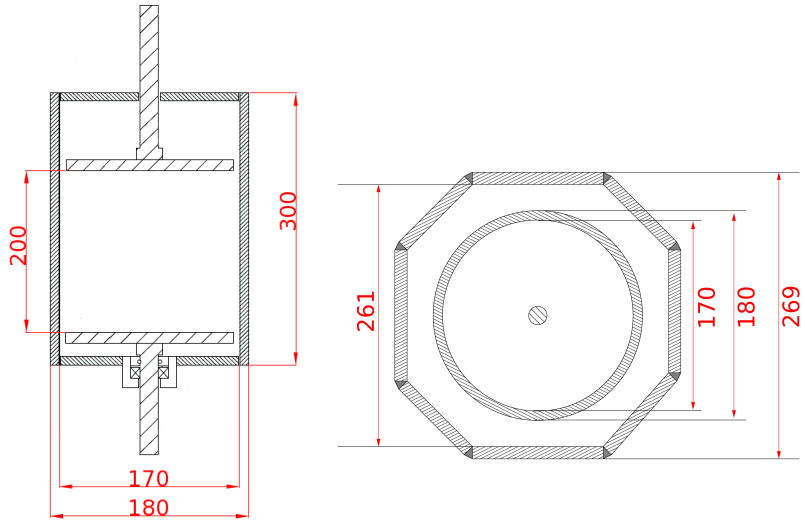

(a) (b)

Figure 3.5: Side view with dimensions of inner part of the Von Kármán flow facility (a) and top view of inner and outer part of facility (b). Units are mm.

the nozzles as shown in Figure 3.7.

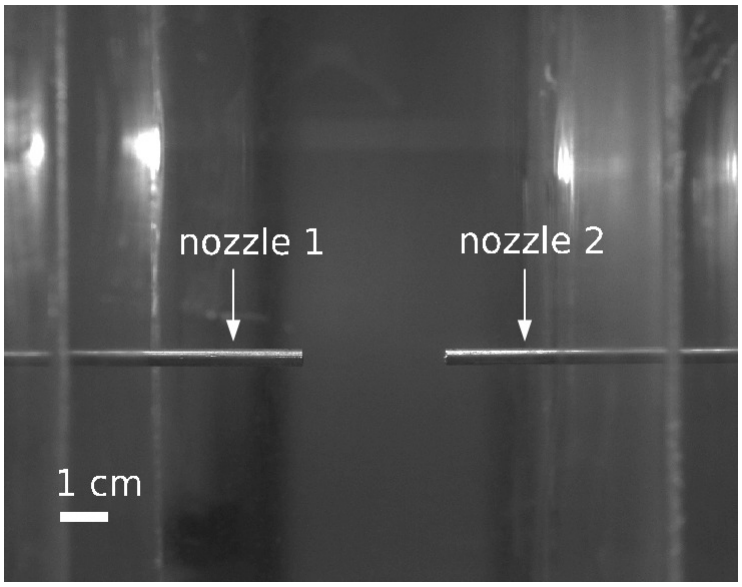

Figure 3.6: Droplet injection nozzles.

Two computer controlled syringe pumps (Hamilton 500B) with 25 ml syringes inject the droplet fluid. The control of the amount of fluid to be dispensed is in integer units where every unit is $1/1050^{\text{th}}$ of an entire syringe. The control of the time during which the

Figure 3.7: Core cylinder of Von Kármán flow facility with nozzles for droplet injection.

selected amount of fluid is dispensed is also in integer units, where a unit corresponds to the number of seconds in which an entire syringe is emptied. So a smaller number corresponds to a faster dispense. As an example, a typical setting is an amount of liquid corresponding with 4 steps and a time setting of 10. This would be equal to a dispense of 0.0952 ml in 0.0381 s. The use of the pump is explained in the pump manual [32], and LabView software is used to control the pump. The pumps are connected to a reservoir and before every collision an amount of fluid equal to the dispensed amount is collected from the reservoir via the tubing. The injected fluid flows from the pump to the nozzle through the tubing which enters the flow facility through two holes in its top lid. In order to reduce flow losses the length of the tubing is kept as small as possible, to approximately 40 cm. It is of very high importance to eliminate the presence of air in the tubing in order to attain a stable and reproducible droplet generation. It is further important to note that there is a limit in injection velocity above which the droplet shape and pinch off are no longer well defined, because a thin thread of fluid remains attached to the nozzle. When injecting fluid at a very low flow rate, it can occur that the droplets do not pinch off at all or have significantly accelerated vertically by buoyancy before collision.

3.2.3 Droplet imaging set-up

Without a turbulent background flow, the droplet trajectories lie more or less in a thin plane. Because of the inherent three dimensional character of turbulent flows it is necessary to track the droplets in 3D in order to estimate the impact parameter and droplet velocities. The minimum number of points of view necessary to estimate the position of an object using lines of sight is two. An ideal imaging configuration with regard to the expected cylindrical symmetry of the drops is a dual axis setup where the axes are orthogonal, so

one camera images a vertical plane and another camera images a horizontal plane with both planes parallel to the center line through the nozzles. Due to the axes of the discs and the discs themselves a configuration like this is not possible. Instead the imaging configuration is chosen to be consisting of two cameras at 45^o on the same side of the nozzles, at a height identical to that of the nozzles and one camera imaging the nozzles with a line of sight perpendicular to the center line through the nozzles but from below at an angle of 27^o with the horizontal, see Figure 3.8. Because of this angle a prism filled with demineralized water is used to optimize the imaging by reducing the effects of refraction. The prism is attached to the flow facility using hair gel. The hair gel has a refractive index close to that of the tank and prism walls and has a viscosity so that it does not flow away from between the tank and prism walls. In order to be able to focus the two side cameras in a vertical plane through the center line through the nozzles, Scheimpflug adapters [7] are used on these cameras. Light is provided by three LED panels mounted opposite to each camera. The experimental setup is depicted in Figure 3.8 where also the numbering of the cameras is defined. A close up of the imaging during measuring is shown in Figure 3.9.

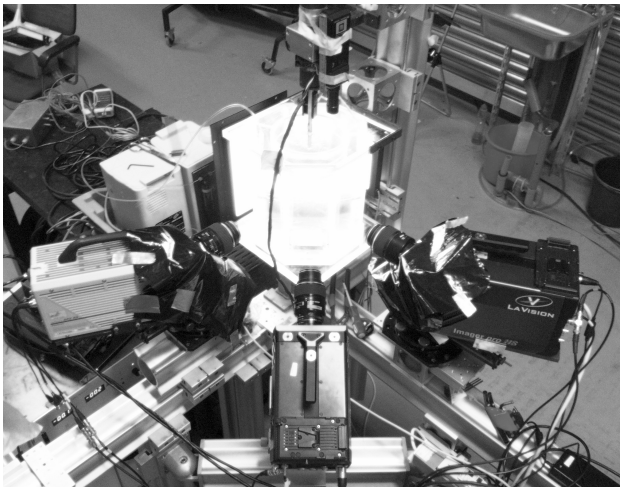

Figure 3.8: Imaging setup. Left camera is cam III, center camera is cam I, right camera is cam II.

The central camera, cam I, and the rightmost camera in Figure 3.8, cam II, are of type LaVision Imager Pro with a 2016×2016-pixel 12-bit image format and CMOS type sensor. Camera III is of type Photron APX-RS with a 10 bit CMOS sensor array and a resolution of 1024×1024 pixels. The objectives used for all cameras are of type Nikon Micro-Nikkor with a focal length of $f = 105$ mm and with $f^{\#} = 5.6$. LaVision Davis software version 7.1 is used to control cameras I and II. Camera III is controlled by Photron software, which is triggered by the LaVision software. Based on the acquired images the droplets can be tracked in 3D. The droplet tracking procedure is explained in section 3.4.

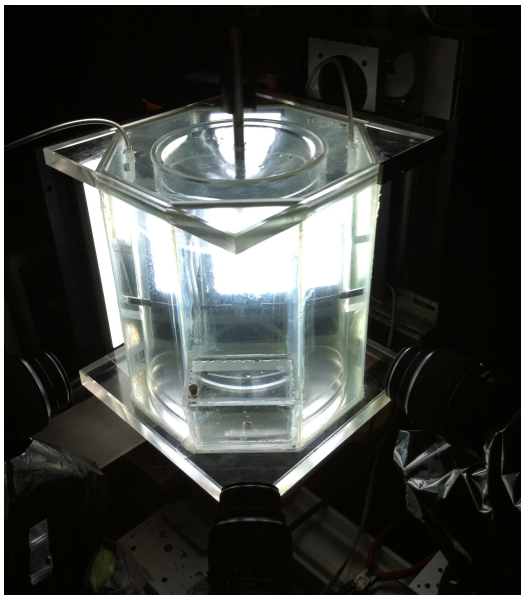

Figure 3.9: Close up of the Von Kármán flow facility and imaging setup during measurements.

3.3 Flow characterization by means of PIV

A fully characterized turbulent flow field is one of the requirements for the experimental facility. In this section the quantification of the flow in the Von Kármán facility is described.

3.3.1 Experimental approach

PIV was used to quantify the flow in the experimental facility [7]. The measurement plane is located at the center of the facility and is conceptually indicated in Figure 3.10. The size of the field of view is 2.2 × 2.2 cm^2. A Neodymium-doped yttrium lithium fluoride (Nd:YLF) laser (New Wave Pegasus) is used to illuminate the field of view. The laser beam is formed into a vertical sheet by a negative cylindrical lens with a focal length of $f = -300$ mm. For imaging a Photron APX-RS camera with a 10 bit CMOS sensor array and a resolution of 1024 × 1024 pixels is used. The camera is imaging the field of view straight from the front. This is different from the imaging setup for the droplet tracking as indicated in Figures 3.8 and 3.9. Flows driven by disc rotation velocities from 250 to 500 rotations per minute (RPM) in steps of 50 RPM are quantified. The frequency at which double frame images are acquired is 50 Hz during 40 s. Times between the double frame images range from 400 μs for the 250 RPM case to 300 μs for the 500 RPM case. A Nikon Micro-Nikkor objective with a focal length of $f = 105$ mm is used with $f^{\#} = 5.6$. The image correlation is performed using 32 × 32 pixel interrogation areas corresponding to 0.69 × 0.69 mm^2 and 7.0 × 7.0 times the Kolmogorov length scale η_K at 250 RPM. 0% correlation window overlap is used for the velocity statistics while a separate re-analysis

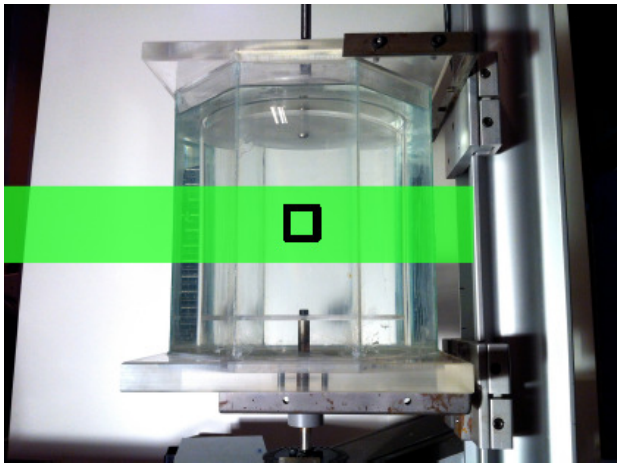

Figure 3.10: Sketch of the location of the field of view for the PIV measurements. The size of the field of view is 2.2 × 2.2 cm. The green area is an indication of the laser sheet.

of the images at 75% overlap is used to compute the spatial derivatives. According to Tokgoz et al. [78] a vector spacing of $\delta_x/\eta_K \approx 1.5 - 2.0$ is required to resolve the turbulent dissipation scales. Here δ_x represents the vector spacing. The current value of $\delta_x/\eta_K = 1.74$ when using 75% overlap thus complies with this requirement. To compute the velocity gradients, a second order polynomial regression to the measured velocity field is used, see Elsinga et al. [28]. The quantities that describe the flow are the horizontal and the vertical velocity fluctuations u_{rms} and v_{rms}, the Reynolds number based on disc rotation velocity and disc radius, $Re = \Omega_I {R_I}^2/\nu$ and the Reynolds number based on the velocity fuctuations and the Taylor micro scale λ_T, $Re_\lambda = u_{rms}\lambda_T/\nu$, the Kolmogorov length scale η_K and the Kolmogorov time scale τ_K and the dissipation rate ϵ. All flow velocities are determined on a centrally located horizontal line and then averaged. The Taylor micro scale, indicative of the scale at which viscous dissipation starts to affect the eddies, is determined by dividing the horizontal velocity fluctuations by their horizontal derivative: $\lambda_T = u_{rms}/\left(du'/dx\right)_{rms}$. To determine the actual dissipation rate one should in principle require the full velocity gradient tensor. However, under the assumption of isotropy an estimation proposed by Tanaka and Eaton [75] can be used:

$$\epsilon \approx 3\nu\left(\overline{s_{11}^2} + \overline{s_{22}^2}\right) + 12\nu\overline{s_{12}^2}, \text{ with } s_{ij} = \frac{1}{2}\left(\frac{\partial u_i'}{\partial x_j} + \frac{\partial u_j'}{\partial x_i}\right), \tag{3.1}$$

where the indices i and j refer to the horizontal direction if they are equal to 1 and to the vertical direction if they are 2. From the dissipation rate the Kolmogorov length and time scale are computed as follows:

$$\eta_K = \left(\frac{\nu^3}{\epsilon}\right)^{\frac{1}{4}}, \text{ and} \tag{3.2}$$

$$\tau_K = \left(\frac{\nu}{\epsilon}\right)^{\frac{1}{2}}. \tag{3.3}$$

3.3.2 Results

The averaged velocity field is shown in Figure 3.11. The color scale indicates the vertical component of the velocity and the arrows indicate the average velocity vectors. It can be observed that in the lower part of the field of view, the flow is downward and in the upper part of the field of view the flow is upward. From the sides inflow can be observed. The velocity field resembles the centrifugal component of the flow in Figure 3.3. The location of the stagnation point of the average flow differs between the measurements. This is in accordance with other measurements on similar flows such as by Ravelet [69] and Worth [84]. Azimuthal velocities are not measured in the current work. In the work of Ravelet [69] typical azimuthal velocities in the case without baffles are $V_\Theta/\Omega_I R_I \approx \pm 0.2$ near the edge of the discs and $V_\Theta/\Omega_I R_I \approx 0$ at the horizontal plane through the center. V_Θ denotes the azimuthal flow velocity. Because of the geometrical similarity approximately the same values are expected here. Table 3.1 displays the relevant flow quantities. Note that the flow quantities that contain derivatives can display inaccuracies for the cases of rotation rates of 250 rpm and 300 rpm. The inaccuracies are expected to be caused by particulate contamination in the flow facility during the relevant measurements.

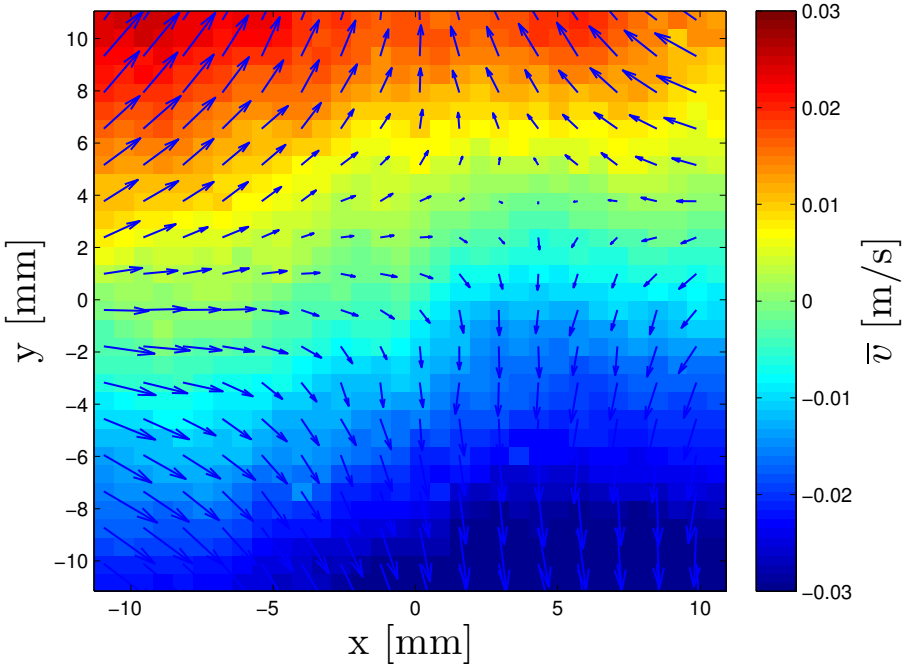

Figure 3.11: Typical average velocity field. Case 450 RPM in Table 3.1. One out of every two velocity vectors is shown.

Figure 3.12 shows the probability density functions of the horizontal and the vertical velocity fluctuations normalized with the velocity of the edge of the disc. In Figure 3.12 also a fitted Gaussian distribution is depicted. It is found that the collapse is reasonable. A

Table 3.1: Measured flow properties.

Case (RPM)	$\Omega_I R_I$ (m/s)	Re	Re_λ	u_{rms} (m/s)	v_{rms} (m/s)	λ_T (mm)	η_K (mm)	ϵ (m^2/s^3)	τ_K (ms)
250	2.17	1.80×10^5	141	0.064	0.035	2.2	0.099	0.0106	9.7
300	2.61	2.16×10^5	182	0.070	0.044	2.6	0.099	0.0104	9.8
350	3.04	2.53×10^5	243	0.090	0.057	2.7	0.088	0.0166	7.8
400	3.48	2.89×10^5	286	0.106	0.068	2.7	0.081	0.0231	6.6
450	3.91	3.25×10^5	269	0.117	0.074	2.3	0.072	0.0372	5.2
500	4.35	3.61×10^5	324	0.141	0.086	2.3	0.065	0.0548	4.3

striking difference with similar measurements, like those by Worth [84], is that relative to the disc edge rotation velocity the fluctuations are much smaller. This is caused by the absence of baffles on the discs. The fact that the standard deviation in the x-direction σ_x is approximately a factor 1.5 times the standard deviation in the y-direction σ_y is in agreement with measurements of Worth [84] and Voth et al. [82]. The cause of this difference is that the poloidal flow component stretches the flow vertically which induces more pronounced horizontal velocity fluctuations; see for example Nieuwstadt [62].

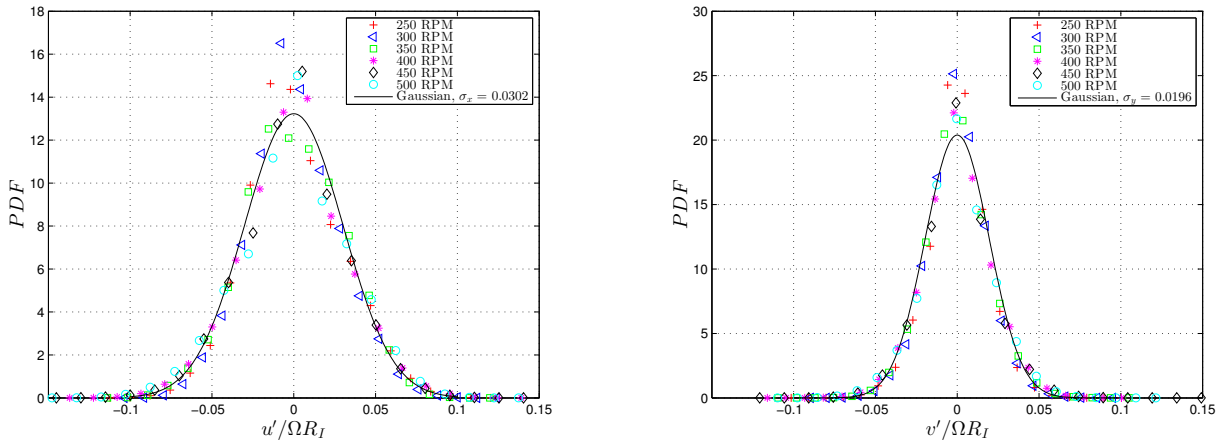

(a) (b)

Figure 3.12: Probability density functions of velocity fluctuations. (a) PDF of u'. (b) PDF of v'.

Figure 3.13 shows the horizontal and vertical velocity fluctuations versus the disc rotation velocity along with linear fits. It can be observed that the fluctuations in the horizontal component are approximately a factor 1.5 times the fluctuations in the vertical velocity. According to Voth et al. [82] the approximately linear behavior of the fluctuating velocity components with respect to the rotational frequency of the discs indicates that there is no

change in the large scale structure of the flow.

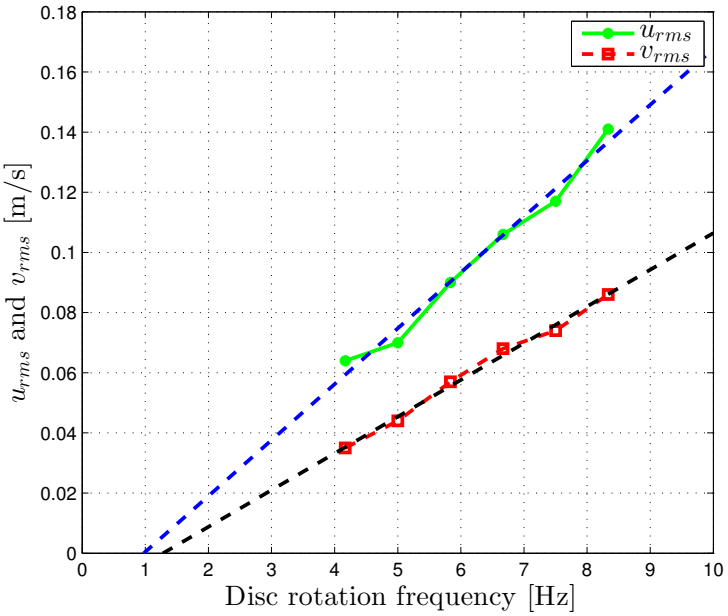

Figure 3.13: Velocity fluctuations as a function of the disc rotational frequency.

The integral length scale of the turbulence is not explicitly measured in the current work but an approximation can be done by applying an estimate for homogeneous isotropic turbulence from the work of Pearson et al. [65] for the relation between the Taylor micro scale Reynolds number Re_λ and a Reynolds number based on the velocity fluctuations and the integral length scale L: $Re_L = \rho_c u_{rms}/\nu$ as follows: $Re_\lambda \sim \sqrt{15 Re_L}$. Estimating the integral length scale L using values from Table 3.1 leads to a minimal estimate of $L = 2.1$ cm. In the work of Worth [84] a ratio of integral length scale to disc diameter of $L/D_{disc} \approx 0.07$ is found. In the current work this ratio is $L/D_{disc} \approx 0.13$.

3.4 Droplet tracking

The 3D droplet tracking is based on photogrammetry (or the line of sight approach). Via a calibration one can deduce the correspondence between a point in an image and a line in physical space. Three cameras are used as indicated in section 3.2.3. To estimate the position of the droplets one has to determine the point of intersection of the lines corresponding to the droplet position in the images. This approach is similar to photogrammetric 3D particle tracking velocimetry (3D-PTV), see Maas et al. [54]. In this section, the 3D droplet tracking method is explained along with the determination of the impact Weber number and the impact parameter B. The description of the droplet tracking is divided in a subsection on the calibration, 3.4.1, a subsection on the detection of the drops in the images

in subsection 3.4.2 and a subsection on the 3D position determination in subsection 3.4.3. The accuracy of the combined calibration and 3D droplet tracking method is described in subsection 3.6. In subsection 3.4.4 the determination of We and B is described.

3.4.1 Calibration

The coordinate system is defined in Figure 3.14 where also the nozzles are shown. A calibration is required to associate to every position in the image planes a line in object space. Calibrations for the current work are performed using a plexiglas calibration target with plus signs printed on it. The spacing between the plus signs is 5 mm and the size of the marks is 2.5 × 2.5 mm^2. The use of the calibration target is shown in Figure 3.15.

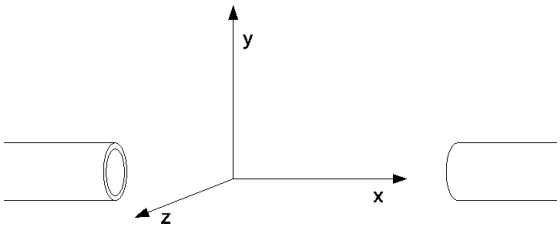

Figure 3.14: Definition of coordinates.

Using a y-z traverse the target is positioned parallel to the nozzles in the x-y plane at positions $z = -10$ mm and $z = 10$ mm and imaged at both positions. The images are projected onto a unique undeformed or dewarped image. Here undeformed means that the plus signs are positioned in a rectilinear grid with equal vertical and horizontal spacing in between the plus signs. The dewarping is based on the procedure as described by Soloff et al. [73]. Per camera per plane z = constant there will be a mapping where x and y in the object plane are described by a third order polynomial in X and Y in the image plane as:

$$x = C_0 + C_1X + C_2Y + C_3X^2 + C_4XY + C_5Y^2 + C_6X^3 + C_7X^2Y + C_8XY^2 + C_9Y^3 \quad (3.4)$$

and similarly for y. In total the mapping is described by twenty coefficients. If the x coordinates of the plus signs on the calibration target are gathered in a column vector $\mathbf{X} = \begin{bmatrix} X_1 & X_2 & \cdots & X_n \end{bmatrix}^T$, the constants are gathered in a column vector: $\mathbf{C} = \begin{bmatrix} C_0 & C_1 & \dots & C_9 \end{bmatrix}^T$ and the n coordinates in the object plane are gathered in a matrix as:

$$\mathbf{A} = \begin{bmatrix} 1 & X_1 & Y_1 & X_1^2 & X_1Y_1 & Y_1^2 & X_1^3 & X_1^2Y_1 & X_1Y_1^2 & Y_1^3 \\ 1 & X_2 & Y_2 & X_2^2 & X_2Y_2 & Y_2^2 & X_2^3 & X_2^2Y_2 & X_2Y_2^2 & Y_2^3 \\ \vdots & \vdots & \vdots & \vdots & \vdots & \vdots & \vdots & \vdots & \vdots & \vdots \\ 1 & X_n & Y_n & X_n^2 & X_nY_n & Y_n^2 & X_n^3 & X_n^2Y_n & X_nY_n^2 & Y_n^3 \end{bmatrix}, \quad (3.5)$$

Figure 3.15: Calibration mesh.

then the coefficients are determined by finding a solution for the matrix equation $\mathbf{AC} = \mathbf{X}$ in terms of $\mathbf{C}$. The system is solved using a least squares linear regression using Matlab software. The same is done for the y coordinates of the plus signs. For every camera this mapping is determined for the planes $z = +10$ mm and $z = -10$ mm. Care must be taken that in the dewarped image the mapping to the plus signs is unique. This can be facilitated by marking one plus sign on the target. If this mapping is determined, the physical location of an object in an image is on a line through the location $(x_{z=+10\ mm}, y_{z=+10\ mm}, z = +10\ mm)$ of the drop in the dewarped image using the mapping for the plane $z = +10$ mm, and the location $(x_{z=-10\ mm}, y_{z=-10\ mm}, z = -10\ mm)$ of the drop in the dewarped image using the mapping for the plane $z = -10$ mm. In this way the lines of sight for every camera through both drops are determined. The estimation of the location of the drop from the lines of sight is explained in section 3.4.3. The magnification for the dewarped images can be determined via the spacing of the plus signs on the calibration target. Figure 3.16 shows raw images of the calibration target for each camera along with the dewarped versions for a calibration target position of $z = +10$ mm.

3.4.2 Droplet detection via image analysis

In the following the different steps in the image processing are explained. Morphological image processing operations such as 'open', 'close', 'erode' and 'dilate' are used [38]. Before these steps are performed a background image is determined by averaging 200 images without droplets for every camera. The steps are shown in Figure 3.17. After background

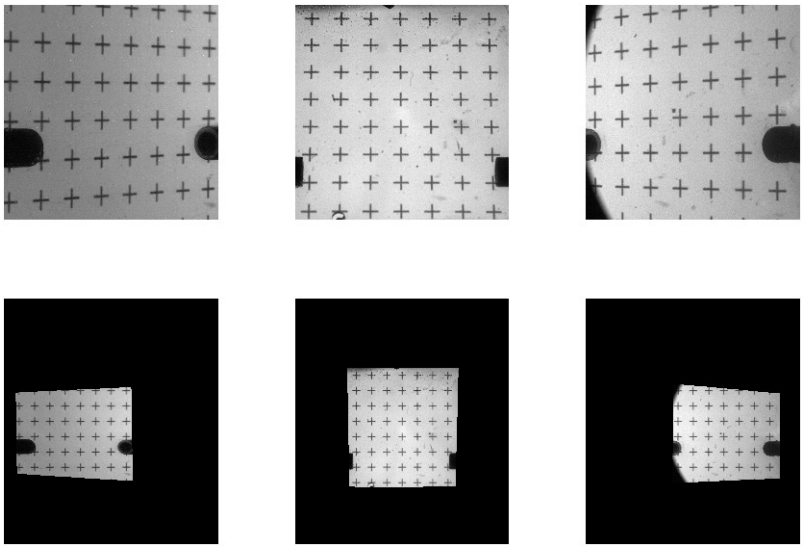

Figure 3.16: Top row: raw calibration images at $z = +10$ mm. Bottom row: dewarped calibration images at $z = +10$ mm. Left: camera 3, center: camera 1, right: camera 2.

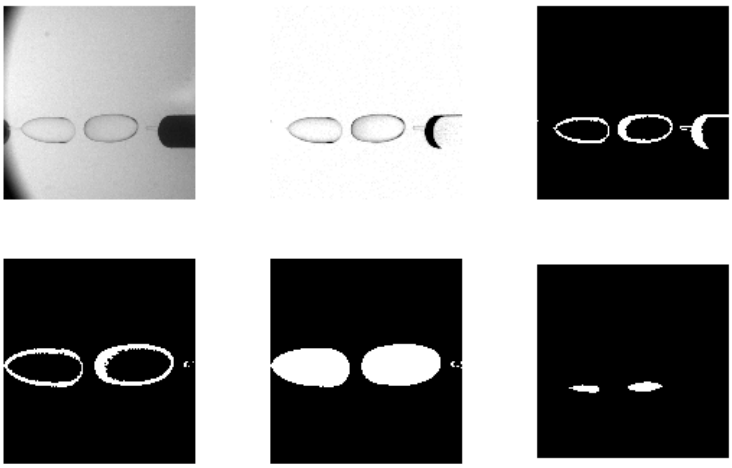

Figure 3.17: Steps of the image processing for the droplet detection. Top left: raw image. Top center: scaling by background. Top right: morphological opening. Bottom left: cropping. Bottom center: inversion, morphological opening, inversion. Bottom right: erosion and decropping (note the apparent change in position due to decroppping).

determination the image processing consists of the following procedure:

1. The image is divided by the background image, see the top middle subfigure in Figure 3.17. Gray values are multiplied times 1000 in order to have conventional pixel values.

2. First the image is binarized using custom threshold levels per camera, see the top right subfigure in Figure 3.17. Approximate threshold values are around 970. Connected

components smaller than 200 pixels are removed.

3. The images are cropped to remove the nozzles, see the bottom left subfigure in Figure 3.17. Note that the cropping is centralized around the droplets, so a larger part of the image above the drops is removed than below them.

4. The droplet outlines are filled by consecutive inverting, removing large unconnected parts like the inner part of the droplets and again inverting, see the bottom middle subfigure in Figure 3.17.

5. When the droplet contours are not closed, the contours are closed by convex closing in case of camera I and camera II, and by iterative dilation and erosion in case of camera III.

6. The droplets are eroded in order to reduce the shadow effect of one drop being behind the other, see the bottom right subfigure in Figure 3.17. The centers of area of the eroded droplets are taken as their position. Note that the drops appear to shift downward due to the asymmetry in the decropping operation.

3.4.3 3D droplet tracking

In section 3.4.1 it is stated that if a droplet is detected in an image, using the two mappings obtained in the process of calibrating, one can project the drop to a position (x, y) at $z = +10$ mm and to a position (x, y) at $z = -10$ mm. These two points define the line of sight on which the drop is located. An example of this projection is given in Figure 3.18, where the top row shows a raw image as from camera II on the left, and the dewarped version for the plane $z = +10$ mm on the right and on the bottom row the same raw image on the left and the dewarped image for the plane $z = -10$ mm on the right.
When a droplet is detected by all three cameras, its location is estimated as the center of the triangle formed by the points of minimal distance between the lines of sight. The expression *point of minimal distance* refers to the middle of the line of minimal distance between two lines of sight. The line of minimal length $\mathbf{w}_c$ between lines $\mathbf{u}$ and $\mathbf{v}$ is perpendicular to both: $\mathbf{u} \cdot \mathbf{w}_c = 0$ and $\mathbf{v} \cdot \mathbf{w}_c = 0$, see [1]. If points on $\mathbf{u}$ and $\mathbf{v}$ are now parametrized as $\mathbf{P} = \mathbf{P}_0 + s\mathbf{u} = \mathbf{P}(s)$ and $\mathbf{Q} = \mathbf{Q}_0 + t\mathbf{v} = \mathbf{Q}(t)$ with $\mathbf{P}_0$ and $\mathbf{Q}_0$ a point on each line. It is now possible to define the points where $\mathbf{u}$ and $\mathbf{v}$ are closest as $\mathbf{P}_c = \mathbf{P}(s_c)$ and $\mathbf{Q}_c = \mathbf{Q}(t_c)$. It is now possible to substitute the relation for $\mathbf{w}_c$ in the inner product equations: $\mathbf{w}_c = \mathbf{P}(s_c) - \mathbf{Q}(t_c) = \mathbf{w}_0 + s_c\mathbf{u} - t_c\mathbf{v}$, where $\mathbf{w}_0 = \mathbf{P}_0 - \mathbf{Q}_0$. This leads to two linear equations:

$$(\mathbf{u} \cdot \mathbf{u})s_c - (\mathbf{u} \cdot \mathbf{v})t_c = -\mathbf{u} \cdot \mathbf{w}_0, \text{ and} \tag{3.6}$$

$$(\mathbf{v} \cdot \mathbf{u})s_c - (\mathbf{v} \cdot \mathbf{v})t_c = -\mathbf{v} \cdot \mathbf{w}_0. \tag{3.7}$$

Putting $a = \mathbf{u} \cdot \mathbf{u}$, $b = \mathbf{u} \cdot \mathbf{v}$, $c = \mathbf{v} \cdot \mathbf{v}$, $d = \mathbf{u} \cdot \mathbf{w}_0$ and $e = \mathbf{v} \cdot \mathbf{w}_0$, s_c and t_c are obtained

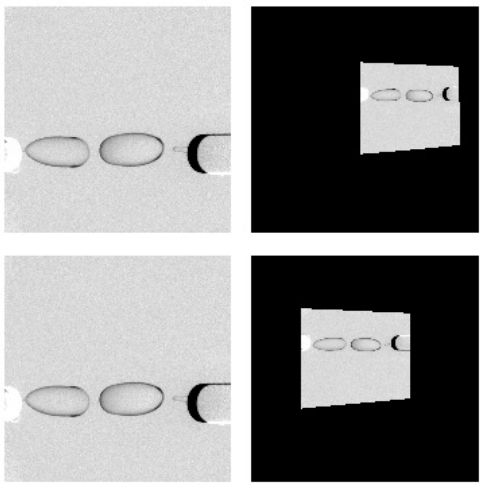

Figure 3.18: Leftmost image for both rows: cropped image divided by background. Top right image: droplets projected to position in the plane $z = +10$ mm. Bottom right image: droplets projected to position in the plane $z = -10$ mm.

via the following relations:

$$s_c = \frac{be - cd}{ac - b^2}, \tag{3.8}$$

$$t_c = \frac{ae - bd}{ac - b^2}. \tag{3.9}$$

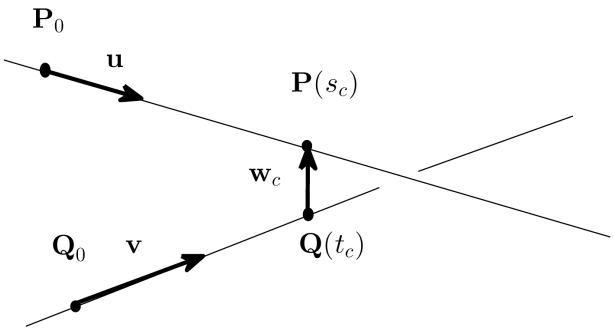

Figure 3.19: Minimum distance between lines, as in [1].

In case two drops are overlapping in one view, this view is discarded and the remaining two views are used. In this case, the droplet position is approximated by the point halfway the line of minimal distance between the two remaining lines of sight. If two or more cameras detect only one drop, the location is left undetermined. If also tracking of the droplets after the collision is desired one has to take into account that the droplets can interchange

position in one or multiple views. In order to detect this, one can compare the distance between the line of sight through one drop, say the leftmost drop in one view, with both the distance between the leftmost drop in another view and the rightmost drop in that same view. If for example the distance between the line of sight through the left drop in view 1 and the left drop in view 2 is much larger than the distance between the line of sight through the left drop in view one and the right drop in view 2, it is likely that in view 2 the drops interchanged horizontal position. Because only trajectories before collision are needed, no elaborate droplet interchange detection is implemented. A typical example of the tracking of droplets is shown in Figure 3.20.

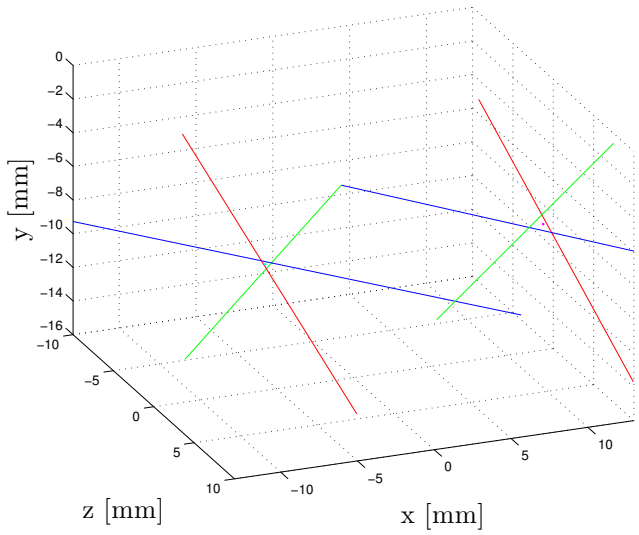

Figure 3.20: Lines of sight for 3D droplet tracking. The red lines are the lines of sight from camera I, the blue lines are the lines of sight from camera II, and the green lines are the lines of sight of camera III.

3.4.4 Determination of *We* and *B*

The Weber number as defined in (1.3) contains one parameter that is derived from the droplet trajectories: the magnitude of the relative droplet velocity, denoted by U. If $\mathbf{U}_1$ and $\mathbf{U}_2$ denote the two droplet velocity vectors and given that the droplets travel in approximately opposite directions, U is defined as:

$$U = ||\mathbf{U}_1 - \mathbf{U}_2||, \tag{3.10}$$

where the Euclidean norm is denoted by the double bars. In order to reduce measurement noise the velocity vectors are taken to be the median averaged value of the first six detected droplet velocities out of the last eleven detected droplet coordinates before collision. Thus

the last four frames for which two separate drops are detected before a collision are discarded, and the velocity vectors are approximated by the median average of the velocities between the seven images before the discarded images. The velocities are approximated by the difference in location multiplied by the imaging frequency of 1000 Hz. To determine the impact factor B first the offset χ has to be defined in terms of the droplet position difference $\mathbf{d}$, where: $\mathbf{d} = \mathbf{d}_1 - \mathbf{d}_2$, where the subscripts refer to the different droplets. This is defined as:

$$\chi = ||\mathbf{d} - \frac{\mathbf{d} \cdot \mathbf{U}}{||\mathbf{U}||^2}\mathbf{U}||. \tag{3.11}$$

Similar to the determination of the drop velocity vectors also for the droplet positions $\mathbf{d}_1$ and $\mathbf{d}_2$ a median averaged value over the last six locations of the seven locations used to determine the velocity is taken. The impact factor is then given by:

$$B = \frac{\chi}{2R}, \tag{3.12}$$

where R is a volume equivalent radius which can be determined from the amount of injected fluid.

3.5 Fluid properties and droplet size

The injected liquid volume is 0.0952 ml per drop, which leads to a volume equivalent radius of $R = 2.8$ mm. The determination of the interfacial tension is described in Appendix B and is found to be 41 mN/m. The drop density and viscosity are taken from the product sheet. The relevant parameters of the Wacker silicone fluid used for the drops are given in Table 3.2.
It thus holds that the diameter of the droplet is smaller than the estimated integral length scale of the turbulence: $2R < L$ with $L \approx 2.1$ cm as shown in section 3.3.2.
Now that the fluid properties and the turbulence properties are known the typical maximum diameter a droplet can attain in turbulence can be calculated according to equation 1.10. The values for the maximum diameter range from approximately $D_{max} = 1$ cm at a disc rotation rate of 250 rpm to $D_{max} = 5.4$ mm at 500 rpm. It is thus expected that the turbulence at the center of the facility will not cause the injected drops to break up except potentially at a disc rotation rate of 500 rpm. It could be possible that the turbulent eddies deform the injected droplets.

3.6 3D tracking accuracy estimate

To gain insight in the accuracy of the 3D droplet tracking method one can reconstruct a selection of points of which the location is known and compare the reconstructed values with the known locations. To do this, the calibration target is imaged at z coordinates $z = -5$ mm and $z = +5$ mm and the locations of the markers are reconstructed using

Table 3.2: Fluid properties of Wacker silicone fluid AK5 and water at 25^oC and volume equivalent drop radius R.

	Viscosity ratio λ
	4.6
Silicone oil AK5	
Density ρ_d (kg/m^3)	920
Dynamic viscosity μ_d $(mPas)$	4.6
Volume equivalent radius R (mm)	2.8
Water	
Density ρ_c (kg/m^3)	997
Dynamic viscosity μ_c $(mPas)$	1.0
Interface tension σ (N/m)	0.041

the algorithm as described in subsection 3.4.3. It is then possible to compare the reconstructed locations with the idealized marker locations. Idealized marker locations are integer multiples of the distance between the markers, so examples are: $(-10, -5, -5)$ mm, $(-5, -5, -5)$ mm, $(0, -5, -5)$ mm, $(-10, 0, -5)$ mm, $(-5, 0, -5)$ mm, $(-10, -5, +5)$ mm, $(-5, -5, +5)$ mm, etc. It is now possible to determine the difference between the ideal coordinates and the reconstructed coordinates $\Delta\mathbf{x}_{calib} = \mathbf{x}_{ideal} - \mathbf{x}_{rec}$. In Figure 3.21(a) the z-component of this difference is shown for the two mentioned planes. The z-component is chosen because it has the largest absolute difference Δz_{calib} and largest gradients in difference. From this Figure it can be observed that the central part of Δz_{calib} has negative values around $\Delta z_{calib} \approx -0.4$ mm. This means that the reconstructed planes are *in front of* the ideal planes. Figure 3.21(b) shows the averaged value of Δz at $z = -5$ mm and $z = +5$ mm. The errors are smaller than 0.5 mm and thus errors due to different sources, are expected to be more significant.

Two possible sources of loss of accuracy are the expected *ellipticity* of the droplets and the shadow effect and the associated *reconstructed trajectory discontinuities*. In case of an asymmetric collision due to turbulent velocity fluctuations it is possible that during a number of frames only two cameras detect two separate droplets whereas before both drops are detected in all images. Because two of the three views image the drops with a non constant magnification and the droplets are non spherical the detected droplet location is expected to display small jumps when the number of lines of sight for a drop decreases from three to two. The magnitude of the jump can not be larger than half the length of the largest side of the triangle used in the location estimation for the drop. In this way the size of the triangle gives an estimate of the accuracy of the position determination. The drop paths of the droplet collision measurements as presented in chapter 4 can be used to determine the average size of the triangle formed by the three points of minimal

distance between the three lines of sight. Table 3.3 displays the values of the square root of the average area of the triangles $A_{triangle}$ in case of detection by three cameras before collision, averaged over all measurements. Because of fluctuations due to the shadow effect in the reconstructed droplet position just before collision the last four detected locations are discarded. The accuracy of the 3D tracking as described above is thus approximately 0.5 mm. Relative to the volume equivalent drop diameter this is equal to $\frac{\sqrt{\overline{A}_{triangle}}}{2R} = 0.09$.

Table 3.3: Droplet triangulation accuracy and average drop distance during determination of collision parameters. Triangulation accuracy is indicated by the square root of the area of the triangle formed by the three points of minimal distance between the three lines of sight. Reported values are averages over all collisions.

	left drop	right drop
$\sqrt{\overline{A}_{triangle}}$ (mm)	0.52	0.54
$\overline{\|\|\mathbf{d}\|\|}$ (mm)	11	

The droplet velocity vectors for the curved trajectories are determined before the collision occurs. Inherent to this way to determine the velocity vectors are errors due to the *curvature* and due to *acceleration* of the droplets. In order to obtain an estimate for errors of this kind a possibility is to estimate the time between the last detected droplet position and the actual collision and to extrapolate the trajectories for the same curvature and acceleration. The time of actual collision can be estimated by the time at which the droplets are in contact in all views. The measurements as described in chapter 4 show that on average the magnitude of the distance vector $\mathbf{d}$ at the moment when the Weber number We and the impact parameter B are estimated is: $\overline{||\mathbf{d}||} = 11$ mm (also indicated in Table 3.3).

3.7 Discussion and conclusions

In the previous sections the experimental approach is explained. The Von Kármán flow facility is described and the flow is quantified using PIV. Also the 3D droplet tracking consisting of the calibration, the droplet detection in the acquired images and the 3D droplet trajectory determination is elaborated and the fluid properties are given. Finally the determination of the parameters We and B from the trajectories is explained.
The turbulence properties in the central part of the on Kármán flow facility are tabulated in Table 3.1. Values for the velocity fluctuations are in the order of 10^{-2} m/s and the values for the energy dissipation rate are in the range of 10^{-3} to 10^{-2} m^2/s^3. To put these values in perspective: the values for the dissipation are comparable to those found in cumuli and stratocumuli clouds and are relatively low compared to typical engineering

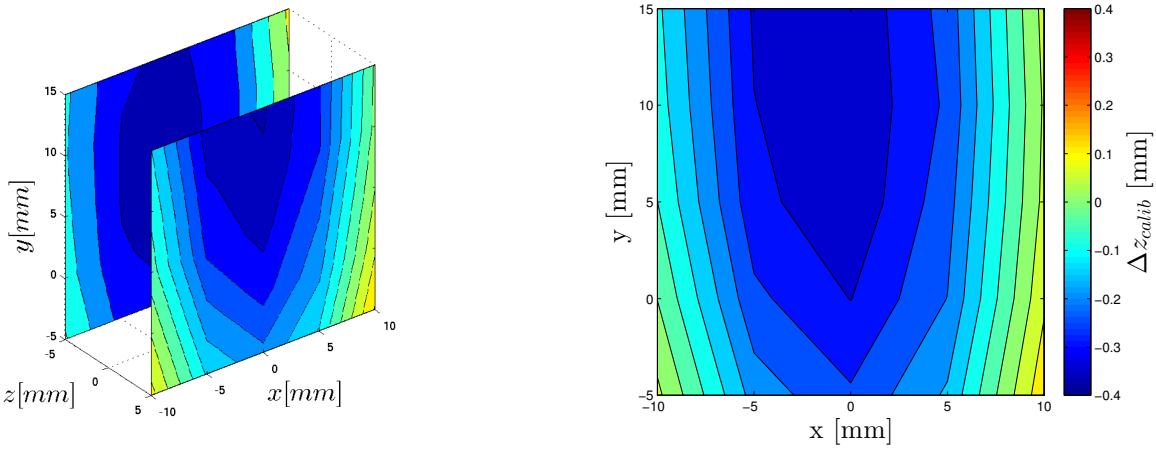

(a) (b)

Figure 3.21: (a) Difference in z-coordinate $\Delta z_{calib} = z_{ideal} - z_{rec}$ between reconstructed points via droplet tracking method and an ideal grid of points at $z = -5$ mm and $z = +5$ mm. (b) Estimated difference between ideal Cartesian grid and reconstruction at $z = 0$ mm.

applications according to Grabowski [31]. The velocity fluctuations in the current setup are smaller than the values for the velocity fluctuations in cumuli and stratocumuli clouds where values of around 1 m/s are attained.
The accuracy of the 3D droplet tracking is estimated to be approximately 0.5 mm which corresponds to 9 % of the drop diameter. This value refers to the reconstruction of the z-coordinate of points with a known location. The corresponding values for the x- and y-coordinates are smaller. One uncertainty in the determination of the collision parameters We and B is that their values are determined when the droplet distance is approximately 11 mm. It is likely that the values for the collision parameters determined in this way are not constant and may change due to continuous turbulent fluctuations but it is difficult to estimate this variation.
In the next chapter the results of the droplet collision measurements in a stationary ambient flow and in a turbulent ambient flow are discussed.

Chapter 4

Droplet collisions

4.1 Introduction

In the present chapter, measurements on colliding droplets are described. The main objective is to quantify a possible change in crossover Weber number between the bouncing and coalescence regimes for the collision outcome between the case of a stationary ambient flow and a turbulent ambient flow. In the following section the experimental approach is explained. This includes the measurement procedure together with a number of practicalities. After this section the results are given. The results section is subdivided in a subsection on collisions in a stationary continuous phase and a subsection on collisions in turbulence. In both sections, first the collisions are described phenomenologically where after results in (B, We)-parameter space are presented. The section on collisions for $Re_\lambda = 0$ is concluded with an observation on the interaction time. In the final section of this chapter conclusions are drawn.

4.2 Experimental approach

First the measurement procedure is explained. The measurement procedure is now explained.
First the flow facility is emptied. To minimize possible influence of change of the chemical composition of the water on the measurements every day of measurements the tank is filled with unused demineralized water. Then the facility is cleaned with filtered water. After the cleaning the facility is put in place, the axle of the bottom disc is connected, the facility is filled with demineralized water, the top part is connected and the prism is attached. The top part is removed, the traversing mechanism with calibration target is installed and the calibration images are captured. Every day of measurement the system is calibrated. Then the nozzle tubing and top part are connected and a number of test collisions are performed. If the test collisions are not satisfactory, the top part is removed and the tubing is reconnected. If the test collisions are satisfactory, top and bottom disc rotation is started. It takes approximately five minutes before both discs are rotating steadily.

Next droplet collision measurements are performed. The triggering of droplet injection and triggering of the cameras is both performed manually. Per collision 300 images are stored in total for camera one and camera two. The images for these cameras are 4032 $\times$ 2016 pixels, of which the top 2016 rows are the image of camera one and the bottom 2016 rows that of camera two. Camera three separately records 300 images.
From previous measurements of droplet collisions in a stationary continuous phase, it is known that during continuous collision of droplets the outcome in terms of bouncing or coalescence tends to vary during the first two collisions and from the third collision onwards stays approximately constant. It is not known whether this behavior is specific for droplets in a liquid or also applies to droplets in a gas. All processed collisions in the current work are thus third or later collisions in a series of collisions except for the collisions measured during one day. Out of the measurements during this specific day only collisions far from transitional behavior are used. Regarding the initially non constant outcome three possible explanations come to mind:

1. due to the droplet injection a minor secondary flow originates which attains some sort of steady state after approximately three collisions.

2. It is likely that the droplets in the second collision in a series of multiple collisions travel through the wake of the droplets in the first collision. The droplets for the first collision do not travel through a wake. This can explain a difference between the first and the second collision in a series of collisions *in a stationary ambient flow.*

3. During the generation of a series of droplet collisions it is expected that the pressure in the tubing does not entirely drop to the level before the first collision but rather increases somewhat during the first couple of collisions. It is expected that this will cause each subsequent collision to occur at an increased velocity difference until the equilibrium state is attained.

In case of a turbulent flow in the Von Kármán flow facility the droplets from the first and second collisions in the series remain in the field of view of the cameras and interfere with the processing of the images. It is possible that during the third collision of the series the droplets do not touch each other because of velocity fluctuations at the location of both drops in opposing directions. If this happens multiple times in a row, droplet accumulation can become too severe and droplet collisions have to be stopped in order to let the droplets rise out of the field of view and pass by the top disc. This takes approximately five minutes. The injection time of the pumps is varied in sweeps from large injection time to small injection time throughout the measurements. In total data is collected during 29 days of which 5 days of measurements are in a stationary continuous phase. The total number of collisions in turbulence is 527 and without turbulence is 159. It is expected that in the turbulent case the range of the measurement data over the impact parameter B is larger than in the stationary case, and the transition between bouncing and coalescence is expected to display a less discrete and more diffuse behavior, so one would like to interpret the data in an averaged sense. This is the reason that the number of measured collisions for

the turbulent case is much larger than for the stationary case. The frequency of imaging is 1000 Hz. For the measurements in turbulence the disc rotation is set to 250 rotations per minute. This corresponds to a Taylor micro scale Reynolds number of $Re_\lambda = 141$. This value is selected so that at least approximately half of the injected droplet pairs lead to an actual collision.
For all cases the drop liquid is silicone fluid (AK5, Wacker). The silicone fluid is a linear polydimethylsiloxane. The density and kinematic viscosity of the fluid at a temperature of 25° are respectively $\rho_d = 920$ kg/m^3 and $\nu_d = 5$ mm^2/s as taken from the product sheet.
All quantities with the dimension of time are non dimensionalised with the droplet oscillation period for the first oscillation mode ($l = 2$) as given by Miller and Scriven [57]. The choice for this non dimensionalisation is made following a remark in the work of Chesters [19] in which the interaction time is related to the droplet oscillation period. The droplet oscillation period equals the inverse of the inviscid drop oscillation frequency corrected for finite viscosity. The inviscid drop oscillation frequency as given by Lamb [51] is defined as:

$$f_l^* = \frac{1}{2\pi}\sqrt{\frac{\sigma l(l+1)(l-1)(l+2)}{(\rho_c l + \rho_d(l+1))R^3}} = \frac{1}{2\pi}\sqrt{\frac{24}{2\rho_c + 3\rho_d}\frac{\sigma}{R^3}}. \tag{4.1}$$

R is the volume equivalent drop radius as defined in (1.8). The corrected drop oscillation frequency is defined as:

$$f_l = f_l^* - \frac{1}{2\pi}\frac{(2l+1)^2\sqrt{f_l^*\mu_c\mu_d\rho_c\rho_d}}{2\sqrt{2}R\left[\rho_c l + \rho_d(l+1)\right]\left[\sqrt{\mu_d\rho_d} + \sqrt{\mu_c\rho_c}\right]}. \tag{4.2}$$

For the liquid properties as given in Table 3.2 this leads to the values: $f_2^* = 15.5\ s^{-1}$ and $f_2 = 14.8\ s^{-1}$ and to an oscillation period of $t_2 = 1/f_2 = 0.068$ s. The normalized time is thus:

$$\tau = t/t_2. \tag{4.3}$$

In the measurements typically 300 images are taken at an imaging frequency of 1000 Hz. This corresponds with $4.42t_2$. Note that one droplet oscillation period equals approximately seven Kolmogorov time scales as defined in 3.3: $t_2/\tau_K \approx 7.0$.

4.3 Droplet collision results

4.3.1 Stationary ambient flow ($Re_\lambda = 0$)

Phenomenological description of collisions The outcome of the droplet collisions at $Re_\lambda = 0$ was either bouncing, coalescence, or coalescence and reflexive separation (also referred to as *near head-on separation*), as described in for example Ashgriz and Poo [8] and Qian and Law [68]. These are regimes II, III and IV in Figure 1.5. Table 4.1 displays the number of times the different phenomena were observed. The distinction between the different collision outcomes was made by inspection of the images. For large values

of the injection time of the pump, often bouncing occurred. An example of a bouncing event is displayed sequentially in Figure 4.2. For this bouncing case the Weber number and the impact parameter are $We = 13$, $B = 0.1$. The measured drop velocities of each drop are approximately 15.8 cm/s in magnitude. One in every five images is shown and the normalized time is zero when the droplets are in apparent contact first. Two satellite drops are formed during the pinch off of the main drops. The main drops are not spherical but rather cylindrical before contact. During contact the drops flatten, but the thin film in between the drops does not drain to a thickness that is thin enough to initiate film rupture. The accumulated surface deformation energy of the flattened interacting droplets is released when the drops are accelerated in the direction opposite of the approach. At the time the apparent interaction between the drops ceases, often a pointy shape at the location of apparent contact is formed, possibly due to the decreased pressure in the film region. In Figure 4.2 this occurs between $\tau = 1.02$ and $\tau = 1.09$. In Figure 4.1 this phenomenon is shown for a different bouncing case. Often the specific shape of the drop interface around this point would cause locally a high image intensity as is the case in Figure 4.1. On the existence of this pointy shape has been speculated in literature by Yoon et al. [88], and it was observed experimentally in a microfluidic setting by Bremond et al. [17] and theoretically by Lai et al. [50]. The shape is referred to as a *nipple* and is not further discussed here. After interacting the drops started to rise due to buoyancy, and the droplet shape becomes approximately elliptical. Sometimes the satellite droplets would be trapped in the wake of the main drops during the buoyant rise.

Table 4.1: Number of observed collision outcomes for $Re_\lambda = 0$.

bouncing	coalescence	stretching separation	reflexive separation	total
34	106	0	19	159

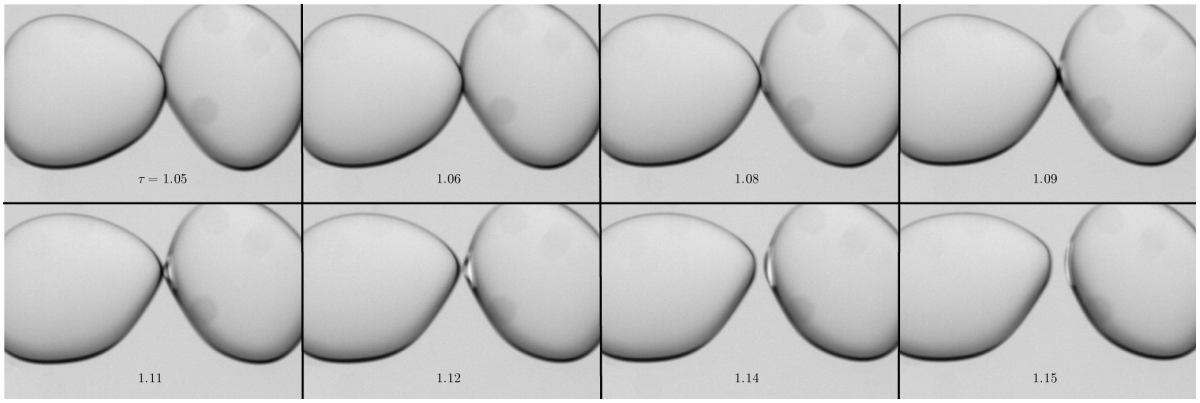

Figure 4.1: Image sequence for nipple formation after bouncing at $Re_\lambda = 0$. Eight consecutive images are shown.

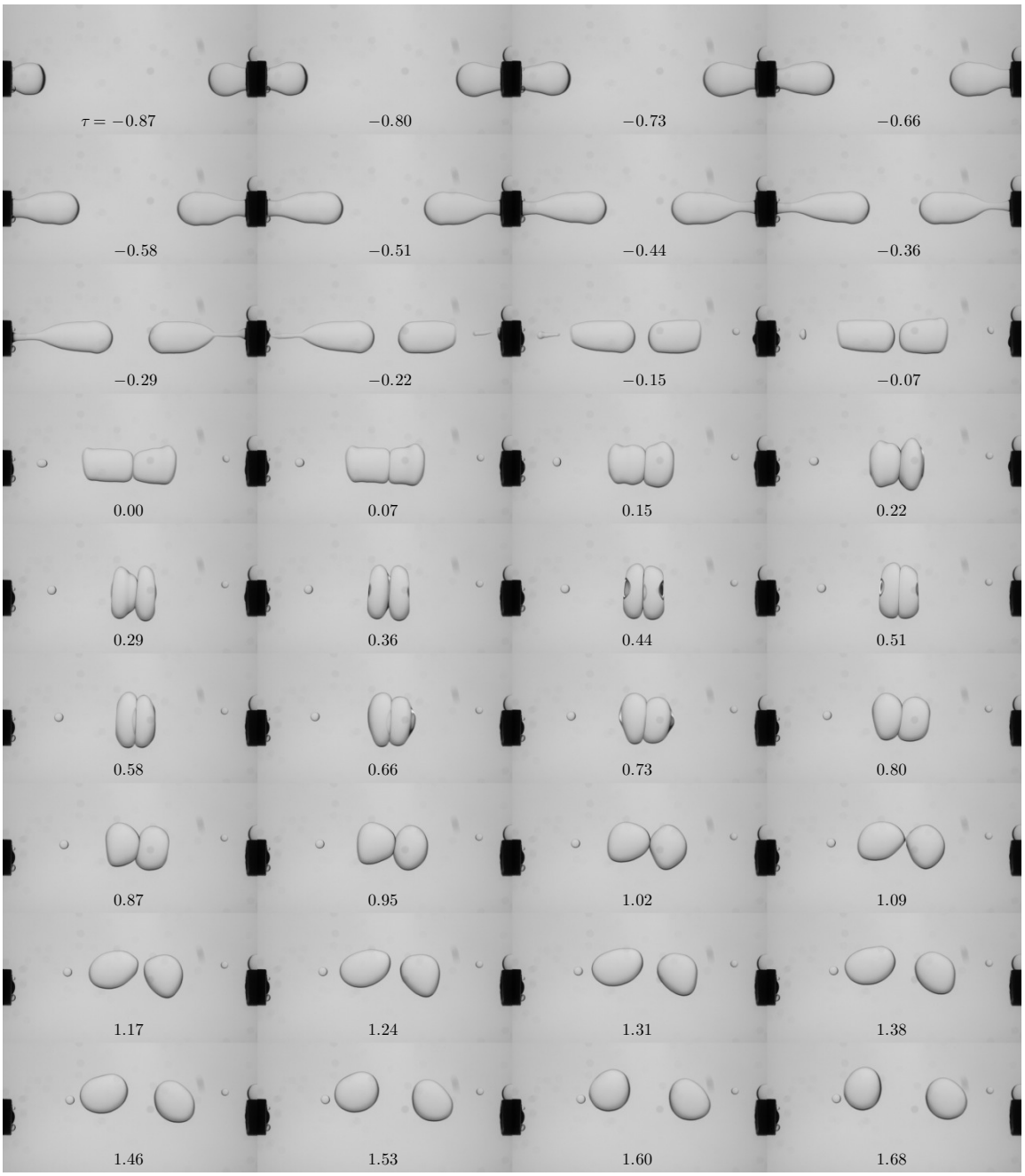

Figure 4.2: Image sequence for bouncing case with $Re_\lambda = 0$. One in every five acquired images is shown. $We = 13$, $B = 0.1$.

Upon decreasing the injection time of the pumps the outcome of the collisions changed from bouncing to coalescence. A typical coalescence event is shown in Figure 4.3. The values of the Weber number and the impact parameter for this case are $We = 36$, $B = 0.2$ so

the dimensional drop velocities are approximately 26.4 cm/s. Before interacting, the drops have a similar shape as in the bouncing case. The drops flatten severely during interaction. Between time $\tau = 0.29$ and $\tau = 0.36$ the film rupture initiates as the visible bridge between the droplets at the upper part of the subfigure at $\tau = 0.36$ indicates. This neck is not visible at the lower part of the area of drop interaction which could hint at off center film rupture. It appears that during the interaction from time $\tau = 0$ to approximately $\tau = 0.51$ the central part of the rear of the droplets continued to advance before retracting again to form two outward bulges between times $\tau = 0.51$ and $\tau = 1.53$. The outward motion of the central part of the rear of the two original drops induced pinch off of two drops of water inside the colliding droplets approximately at time $\tau = 0.66$. These two entrained water drops remain at the leftmost and rightmost part of the coalesced drop at later times as shown in Figure 4.3. Occasionally stretched dark patterns inside the coalesced drop were visible as shown in Figure 4.4. These are likely strings of small droplets formed during film rupture, as shown in chapter 2, because they were only observed after film rupture and not for bouncing cases.

When decreasing the injection time even more the permanent coalescence behavior is expected to change to coalescence followed by reflexive separation. This behavior is indicated by region IV in Figure 1.5. Figure 4.5 shows a sequence of images for this case. During pinch off two satellite drops are formed and the drops flatten severely during interaction. At the start of the interaction the left drop is not entirely pinched off yet. The sudden disappearance of a vertically oriented interface between the left and right droplet indicates that the film ruptures between $\tau = 0.15$ and $\tau = 0.22$. At $\tau = 0.51$ the vertical size of the coalesced droplet is at a maximum, and it then starts to decrease. At approximately $\tau = 0.87$ the horizontal and vertical sizes of the drop are equal and the drop starts to elongate horizontally. Between $\tau = 0.95$ and $\tau = 1.02$ an amount of liquid from the continuous phase is entrained by the left hand side drop. The elongation continues until the coalesced drop breaks up into two large drops and one small satellite drop in between the main droplets at time $\tau = 2.26$.

Figure 4.6 shows the droplet paths for the bouncing case at $Re_\lambda = 0$ resulting from the 3D droplet tracking. The reconstructed path of the left drop is colored cyan and the path of the right drop is colored magenta. When the drops are interacting the path is colored yellow. During the interaction of the drops only one combined drop is detected, and thus the position of both drops is approximated by the position of this combined drop. The jump in location from the separate cyan and magenta tracks to the yellow track during interaction is caused by the jump from the separate drop centers to the combined drop center. The yellow part of the path shows some oscillations. The cause of these oscillations is that in the image processing sometimes the center of mass of the combined drop is found, instead of only the center of mass of the left or right drops. This has no important consequences for the outcome of the measurements concerning the collision parameters We and B, because they are determined from the part of the trajectory before the collision, i.e. the lower cyan and magenta parts in Figure 4.6. The droplet paths belonging to the coalescence sequence in Figure 4.3 are depicted in Figure 4.7(a) and the droplet paths

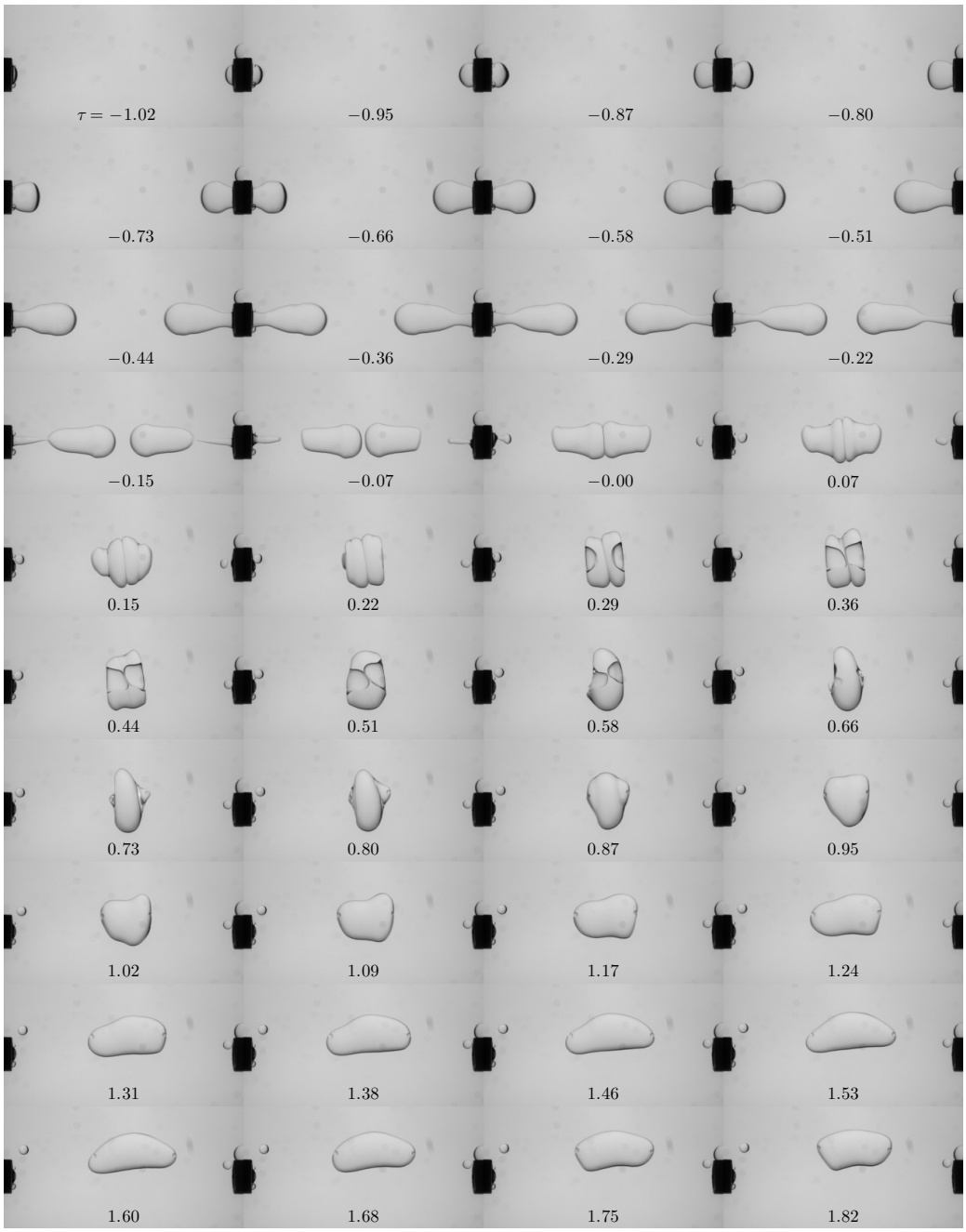

Figure 4.3: Image sequence for coalescence case at $Re_\lambda = 0$. One in every five acquired images is shown. $We = 36$, $B = 0.2$.

belonging to the coalescence and reflexive separation sequence in Figure 4.5 are depicted in Figure 4.7(b), as examples for the mentioned collision outcomes. It can be observed that immediately before the interaction starts the paths of the left and the right drops show

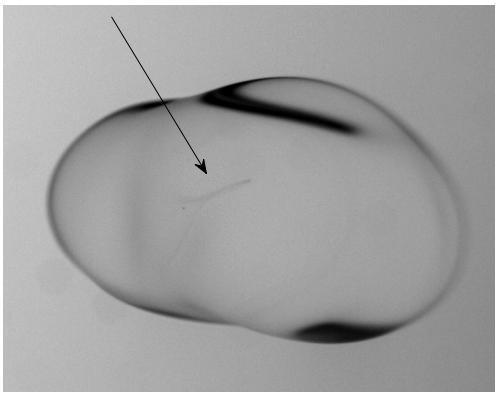

Figure 4.4: Dark stretched pattern, likely a string of satellite drops.

one or two locations which display a small jump in z-coordinate with respect to the earlier part of the trajectory. These jumps occur when one camera no longer detects two separate drops and are thus associated with the start of the drop interaction. This is the reason why the last four drop locations before the start of the interaction are discarded for the determination of the collision parameters We and B.

Results in (B, We)-parameter space All results for $Re_\lambda = 0$ are summarized in the (B, We)-parameter space as shown in Figure 4.8. The collisions resulting in bouncing are predominantly at values of the Weber number smaller than 20. At larger values of We the outcome is coalescence until approximately $We = 77$. At values of We larger than 77 coalescence and reflexive separation is the outcome of the collision. Two cases of coalescence followed by reflexive separation occurred between $We \approx 55$ and $We \approx 60$. The value of $We \approx 20$ at the boundary between the bouncing and coalescence regime is comparable to the values in Qian and Law [68] for liquid droplets in a gas. Because of the expected small inclination of the boundary between bouncing and coalescence it is possible that the transition value would be smaller for nozzles that can be aligned with very high accuracy. With a value of $We_{III,IV} \approx 77$, the transition point between 'coalescence' and 'coalescence followed by reflexive separation' is at a much larger value than any of the associated values in all the measurements by Qian and Law [68], where a value of $We_{III,IV} = 40$ is never exceeded. In their work, Qian and Law [68] find an expression for the boundary Weber number $We_{III,IV}$ based on a balance between kinetic energy, surface energy and viscous dissipation. Approximating the initial droplet shape by a half sphere connected to a cylinder and the severely deformed, pancake like, coalesced drop by a cylinder with dimensions taken from Figure 4.5, a boundary Weber number of $We_{III,IV} = 43$ is found using the model of Qian and Law [68]. A possible explanation of the difference is that the dissipation in the continuous phase liquid is disregarded in the model.
In order to be able to compare to the $Re_\lambda = 141$ case later on it is necessary to display

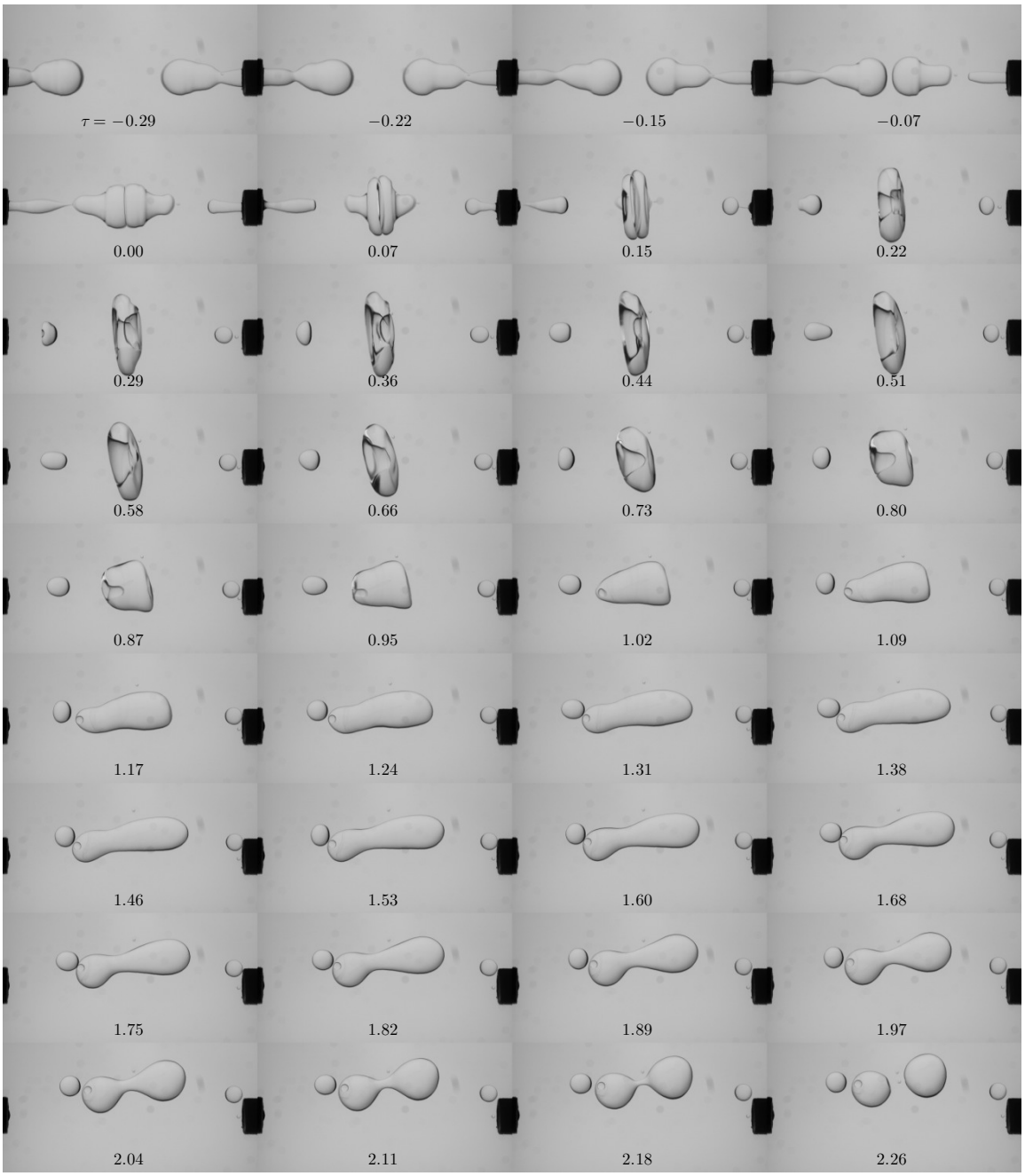

Figure 4.5: Image sequence for coalescence and reflexive separation case at $Re_\lambda = 0$. One in every five acquired images is shown. $We = 88$, $B = 0.1$

the results in an averaged way. To do this, the parameter space is divided in suitably chosen rectangular bins of constant width and height over which the average outcome will be determined. The different collision outcomes are given a weight, which is equal to the

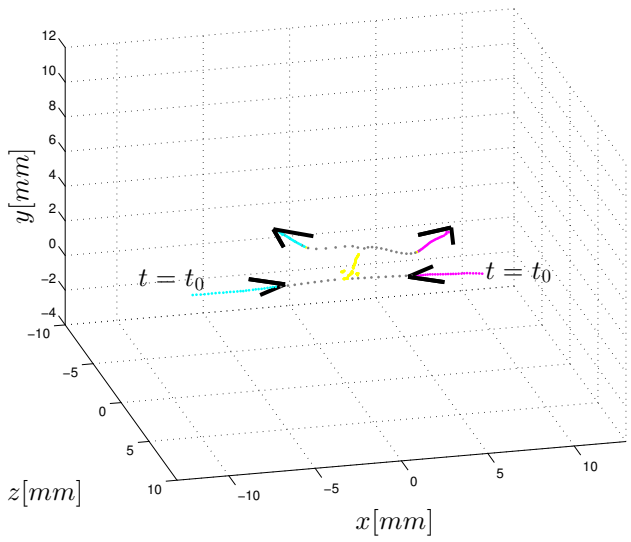

Figure 4.6: Droplet trajectories for bouncing case at $Re_\lambda = 0$. $We = 13$, $B = 0.1$. The droplet injected by the left nozzle is colored cyan and the droplet injected by the right nozzle is colored magenta. During apparent contact the trajectory is colored yellow. The gray dots are interpolations and are only intended as a visual aid.

total number of measurements divided by the number of measurements with the specific outcome of interest. The weight for the bouncing cases will thus be the total number of collisions divided by the number of bouncing cases. This definition for the weight is chosen in order to prevent that collision outcomes that are only found in a small part of the parameter space are ignored. Per bin the number of observations multiplied by the respective weights gives a score, and the type of observation with the highest score is selected to be the average outcome in the bin. To prevent very unlikely events to influence the process too much a minimum number of four observations per bin is required. In the following the size of the bins is chosen to be 10 in Weber and 0.2 in impact parameter B unless mentioned otherwise.

In Figure 4.9 the averaged results are shown. The general features agree with the results in Figure 4.8. It can be observed that the bin size of 10 in Weber number combined with the relatively large weight for the coalescence and reflexive separation cases shifts the distinguishable boundary between coalescence and coalescence followed by reflexive separation down to $We_{III,IV} = 70$ from approximately $We_{III,IV} = 77$. The bins for $20 < We < 40$ and $0.2 < B < 0.4$ were manually removed to prevent excessive extrapolation.

Menke [55] describes measurements of droplet collisions for identical liquids and nozzles and identical volume as in the current work at values of the impact parameter $B > 0.2$. The increase in offset is accomplished by attaching one nozzle to a lateral traverse. Imaging is performed using a dual axis setup with one camera imaging from the front and one camera imaging from below via a mirror. The image processing is similar to the image

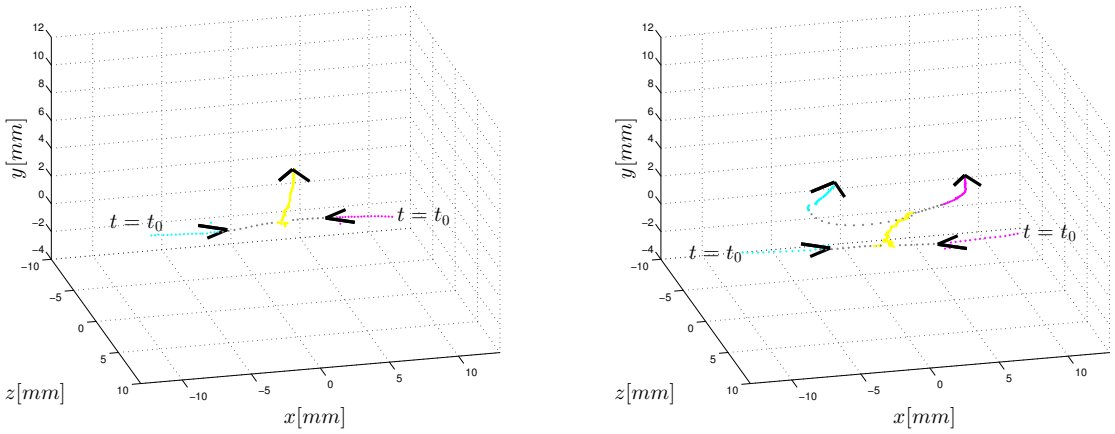

Figure 4.7: (a) Droplet trajectories for coalescence case at $Re_\lambda = 0$. $We = 36$, $B = 0.2$. (b) Droplet trajectories for coalescence and reflexive separation case at $Re_\lambda = 0$. $We = 88$, $B = 0.1$. The droplet injected by the left nozzle is colored cyan and the droplet injected by the right nozzle is colored magenta. During apparent contact or permanent or temporary coalescence the trajectory is colored yellow. The gray dots are interpolations and are only intended as a visual aid.

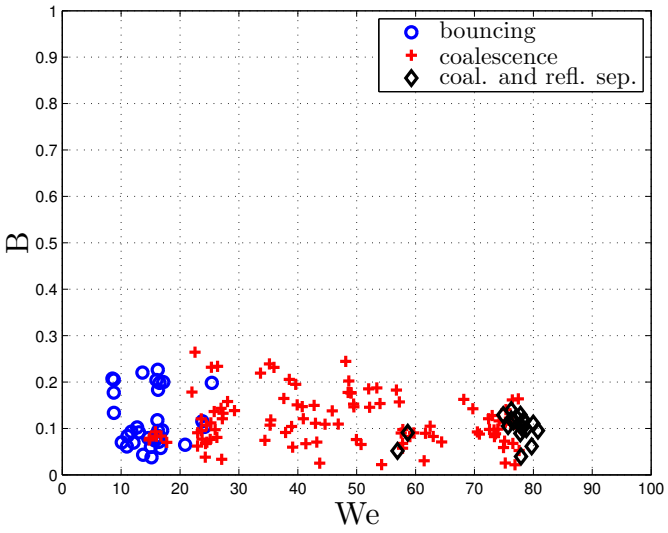

Figure 4.8: Collision outcome in (B, We)-parameter space for $Re_\lambda = 0$.

processing in the current work. The 3D droplet paths are composed from the x and y coordinates of the drops as determined from the front view images, and the z coordinate is determined from the images taken from below. Adding data from these measurements

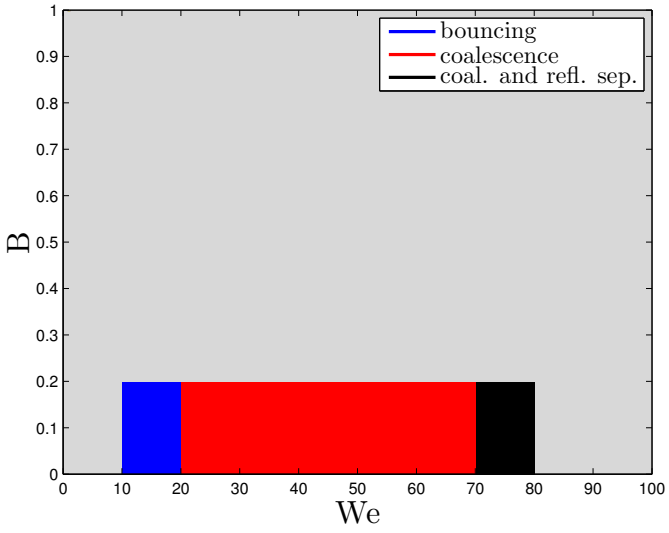

Figure 4.9: Average collision outcome in (B, We)-parameter space for $Re_\lambda = 0$.

to the previously described data leads to a total of 687 collisions as indicated in Table 4.2. The collision outcome of the combined data in terms of the Weber number and impact parameter is shown in Figure 4.10 and the averaged result in Figure 4.11. At larger values of B than present in Figure 4.11 the droplets would not come in apparent contact due to hydrodynamic interaction. The bin size for the impact parameter B was decreased to 0.1 for this plot. As a reference the collision outcome diagram for tetradecane droplets in nitrogen at 2.4 atm in Figure 7c of Qian and Law [68] is shown via digitization of the lines at an identical resolution as in Figure 4.11. The result is depicted in Figure 4.12. Despite scattered data a number of observations can be made:

1. the boundary between bouncing and (initial) coalescence, denoted as $B_{II,III/IV}(We)$, never exceeds $B = 0.5$ in the investigated range of We. This is a significantly smaller value than for liquid droplets in a gas, where the corresponding value is $B = 0.8$ as shown in Figure 4.12. The promotion of bouncing with increase of continuous phase density ρ_c found by Qian and Law [68] is continued for droplet collisions in a liquid.

2. Coalescence followed by stretching separation can occur for $We > 40$ and $B \geq 0.2$.

Table 4.2: Number of observed collision outcomes including collisions at $B > 0.2$ for $Re_\lambda = 0$.

bouncing	coalescence	stretching separation	reflexive separation	total
239	335	90	23	687

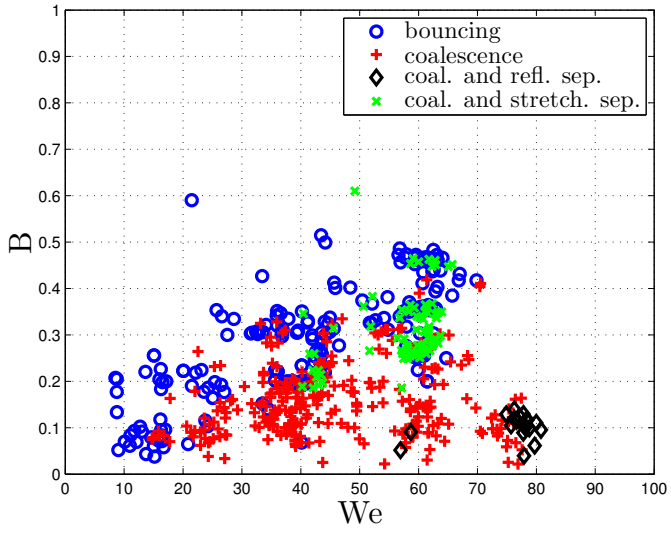

Figure 4.10: Collision outcome in (B, We)-parameter space for $Re_\lambda = 0$ including collisions at at $B > 0.2$.

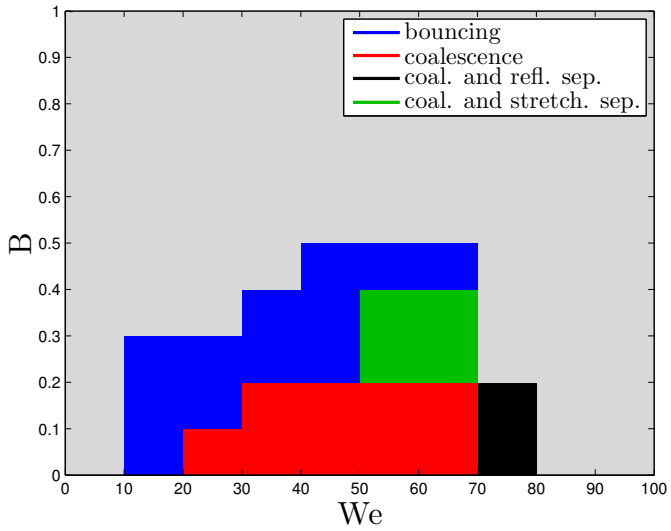

Figure 4.11: Average collision outcome in (B, We)-parameter space for $Re_\lambda = 0$ including collisions at $B > 0.2$. The bin size in Weber number is 10 and in B is 0.1

Interaction time It is possible to determine the film drainage time, defined as the time between the first moment the droplets apparently touch until the moment that the film ruptures, by manually inspecting the images. Film rupture can be observed in the images by the disappearing of the cusp at the top or bottom of the interface between the droplets during collision. An attempt was made to detect film rupture in an automatized way, but

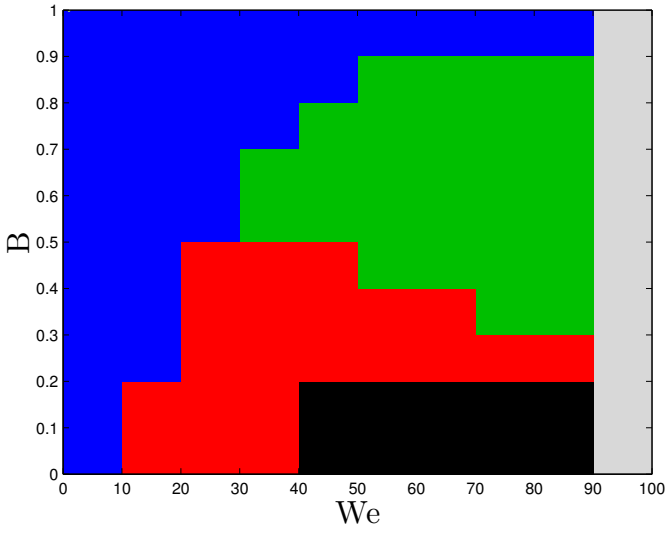

Figure 4.12: Averaged collision outcome diagram for tetradecane droplets in nitrogen at 2.4 atm. Based on lines in Figure 7c from Qian and Law [68].

this was unsuccessful. In Figure 4.13 the total dimensionless drop interaction time in case of bouncing, named $\tau_{interaction}$, the dimensionless film drainage time, $\tau_{drainage}$, and the time from the start of the interaction until eventual break-up, $\tau_{separation}$ in case of coalescence and reflexive separation are indicated as function of the Weber number. The interaction time $\tau_{interaction}$ is obtained from the droplet trajectories. The green lines indicate integer multiples of the viscous drop oscillation period. The green line between $\tau = 2.25$ and $\tau = 2.5$ indicates one droplet oscillation period for the initially sized droplets plus one droplet oscillation period for a droplet with a volume equivalent radius corresponding to the volume of the coalesced drop normalized by the initial drop oscillation period. Symbolically: $\tau = \left(t_{2,initial} + t_{2,coalesced}\right) / t_{2,initial}$.

The blue dots in Figure 4.13 collapse on $\tau = 1$. The interaction time is thus equal to the drop oscillation period. For the cases of coalescence and the cases of coalescence followed by reflexive separation the film rupture time $\tau_{drainage}$ decreases with increase of We. A linear fit on a double logarithmic scale leads to the following relation between $\tau_{drainage}$ and We: $\tau_{drainage} = 5.5\,We^{-0.73}$. For the fit only measurements at $We > 30$ are used. The black line in Figure 4.13 indicates this relation. In cases of coalescence followed by reflexive separation, the separation occurs between two periods of oscillation of the initial droplets and one period of oscillation of the initial droplet plus one period of oscillation of the coalesced drop.

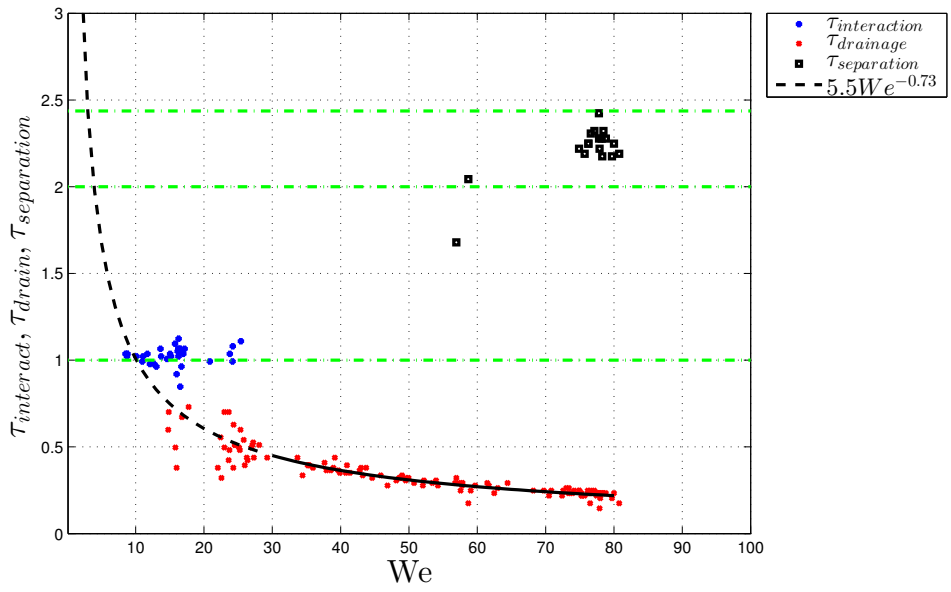

Figure 4.13: Droplet interaction time, film drainage time and time to separation versus We for $Re_\lambda = 0$. The green lines at $\tau = 1$ and $\tau = 2$ indicate the time from apparent first contact between the drops until one full period of oscillation t_2 and two full periods of drop oscillation $2t_2$. The green line between $\tau = 2.25$ and $\tau = 2.5$ indicates the time from first apparent contact until one full oscillation period with the initial drop radius plus one full oscillation period of a drop with a radius of the coalesced drop, normalized by the drop oscillation period corresponding to the initial drop radius: $\tau = (t_{2,initial} + t_{2,coalesced}) / t_{2,initial}$.

4.3.2 Turbulent ambient flow ($Re_\lambda = 141$)

Phenomenological description of collisions Table 4.3 displays the number of observed events for droplet collisions at $Re_\lambda = 141$. The observed collision outcomes are bouncing (II), coalescence (III), coalescence and reflexive separation (IV), and coalescence and stretching separation (V). Because coalescence followed by reflexive separation was observed only two times in 527 measurements, it will not be discussed further.

An example of a bouncing event is shown in Figure 4.14. The trajectories of the droplets are shown in Figure 4.15. For the right drop the shape is different from the non turbulent case. During interaction the droplets interchange position with respect to the nozzles. In the depth direction the right drop passes between the camera and the initially left drop. The interaction time is shorter than in the non turbulent case: $\tau < 0.51$. This is possibly due to the large impact parameter $B = 0.8$. During pinch off two satellite droplets are formed similar to the non turbulent case.

Severely decreasing the pump injection time led to coalescence events occasionally as shown in Figure 4.16. The values of the collision parameters for the coalescence case shown are: $We = 67$ and $B = 0.25$. The trajectories for this coalescence case are shown in subfigure

Table 4.3: Number of observed collision outcomes for $Re_\lambda = 141$.

bouncing	coalescence	stretching separation	reflexive separation	total
368	128	29	2	527

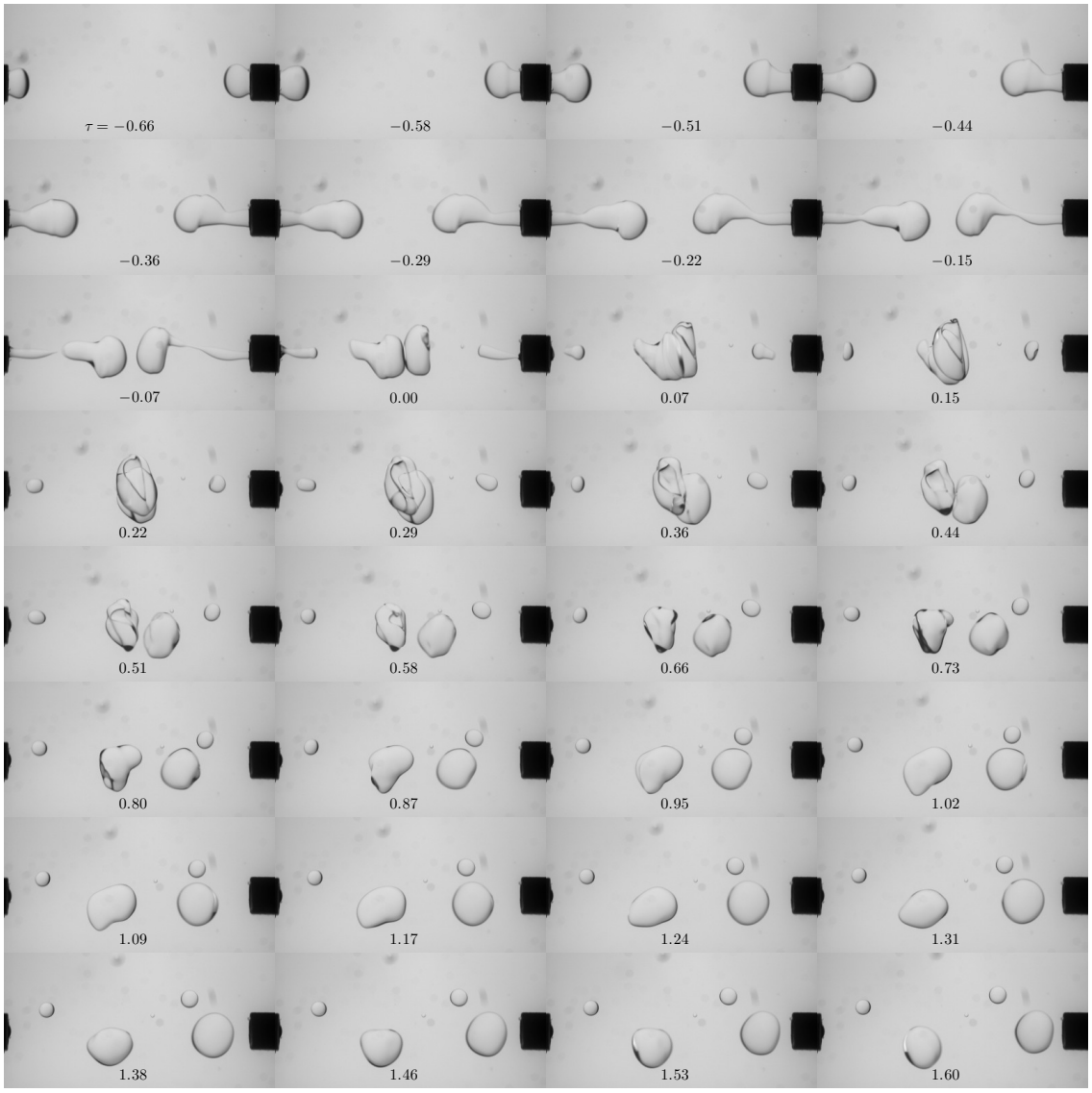

Figure 4.14: Image sequence for bouncing case at $Re_\lambda = 141$. $We = 44$, $B = 0.8$.

(a) of Figure 4.17. As was the case in the bouncing event in Figure 4.14, the shape of the droplets differs between the left and right droplet before impact. The film ruptures between $\tau = 0.22$ and $\tau = 0.29$. Entering the Weber number in the fit for the film drainage time in the non turbulent case (eq. 4.3) gives: $5.5(67)^{-0.73} \approx 0.25$, so this specific collision

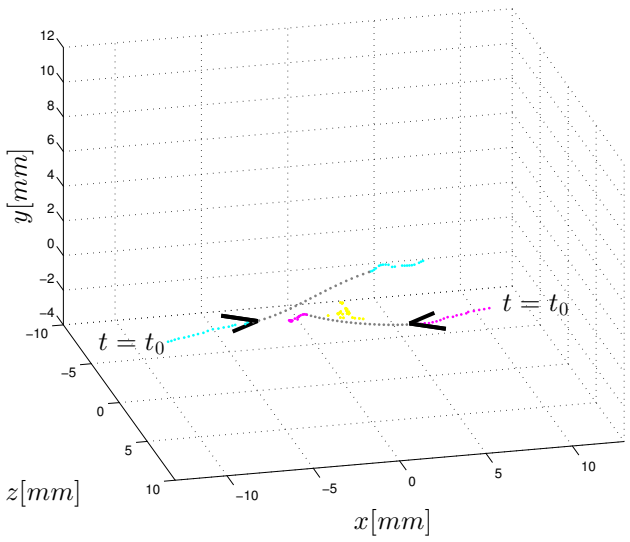

Figure 4.15: Droplet trajectories for bouncing case at $Re_\lambda = 141$. $We = 44$, $B = 0.8$. The droplet injected by the left nozzle is colored cyan and the droplet injected by the right nozzle is colored magenta. During apparent contact the trajectory is colored yellow. The gray dots are interpolations and are only intended as a visual aid.

in turbulence appears consistent with the non-turbulent case.
For short injection times of the pumps collisions sometimes led to coalescence followed by stretching separation, as shown in Figure 4.18. In the depicted case the shapes of the droplets are comparable to those in the case $Re_\lambda = 0$. The trajectories for this event are shown in subfigure (b) of Figure 4.17. Film rupture occurs between $\tau = 0.29$ and $\tau = 0.36$. These values are comparable to those predicted from the fit in the non turbulent case. Following film rupture the drop liquid interchanges position between left and right. The inertia of the drops is too large for the surface tension to overcome, and the coalesced drop breaks up into two separate drops between $\tau = 0.87$ and $\tau = 95$. A satellite drop is formed during the break up.
For large injection times of the pumps often the droplets would not come in apparent contact due to the turbulent velocity fluctuations. When decreasing the injection time to values that generated coalescence events in the case of $Re_\lambda = 0$ collisions would occur.

Results in (B, We)-parameter space Figure 4.19 displays the values of We and B for the measurements at $Re_\lambda = 141$. No clear boundary between any of the four observed regimes of collision outcome is apparent. Two observations can be made on the distribution of events in the parameter space. The event density is low at the region of low We and low B (the left bottom) and at high We and high B (the top right). It is likely that the cause of this distribution is that the injection times on average were shorter in the turbulent case than in the case of a stationary continuous phase. Shorter injection times were needed

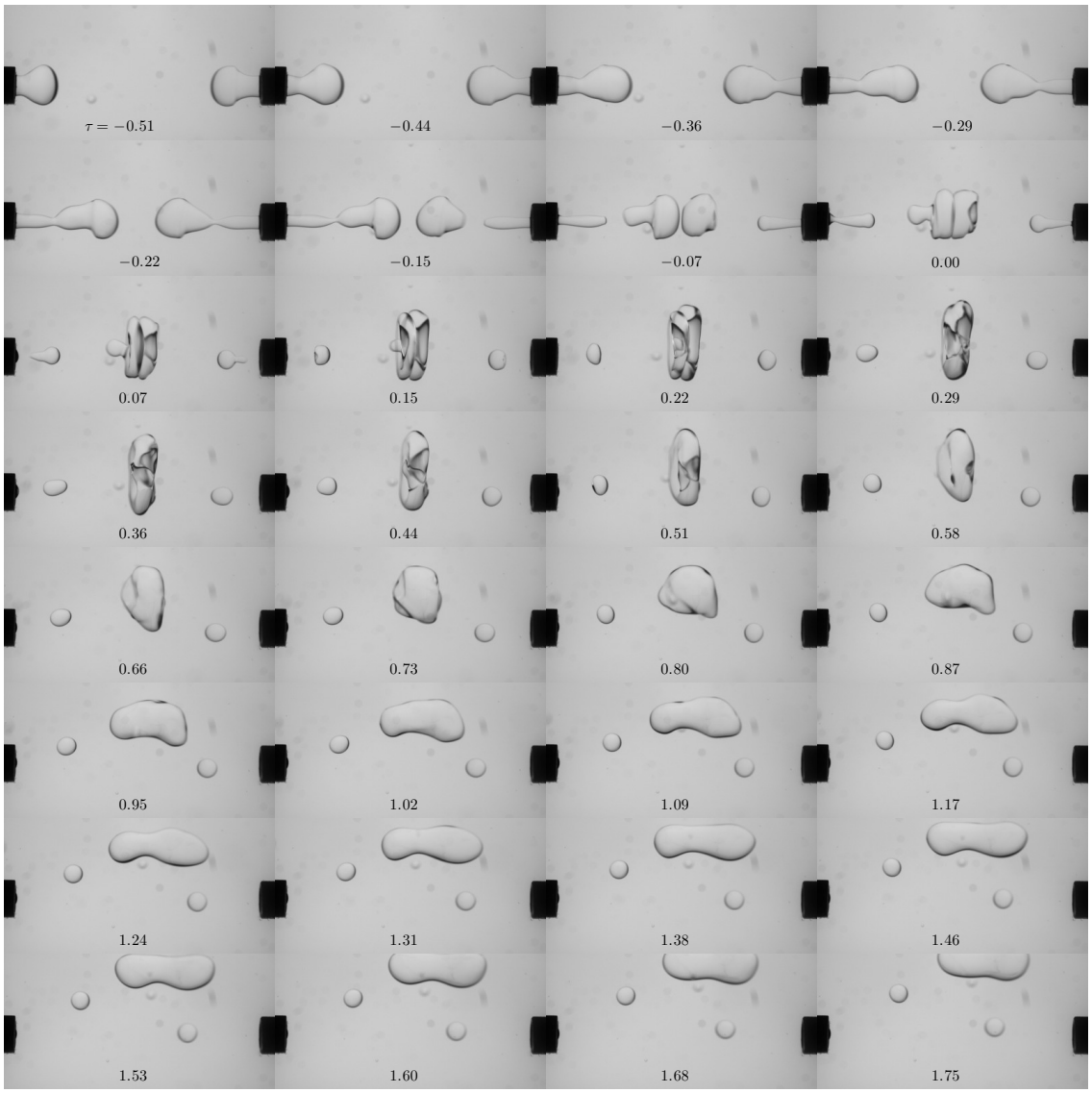

Figure 4.16: Image sequence for coalescence case at $Re_\lambda = 141$. $We = 67$, $B = 0.25$.

in the turbulent case to generate a significant number of coalescence events. In between the mentioned regions the density of events appears to be higher. Secondly the number of events for small value of B is low for the entire range of We. To visualize the number of events a binning is applied with bin size 10 in Weber number and 0.2 in B and the result is shown in Figure 4.20. A decrease of the number of events with increasing We at some fixed value of B can be explained by an increase in travel time before collision, and thus a larger offset during collision. Inspection of the collision outcome leads to the following observations. Coalescence at small value of the Weber number $We < 1$ did not occur. In the entire data set only one event exists for which $We < 1$. Coalescence events appear

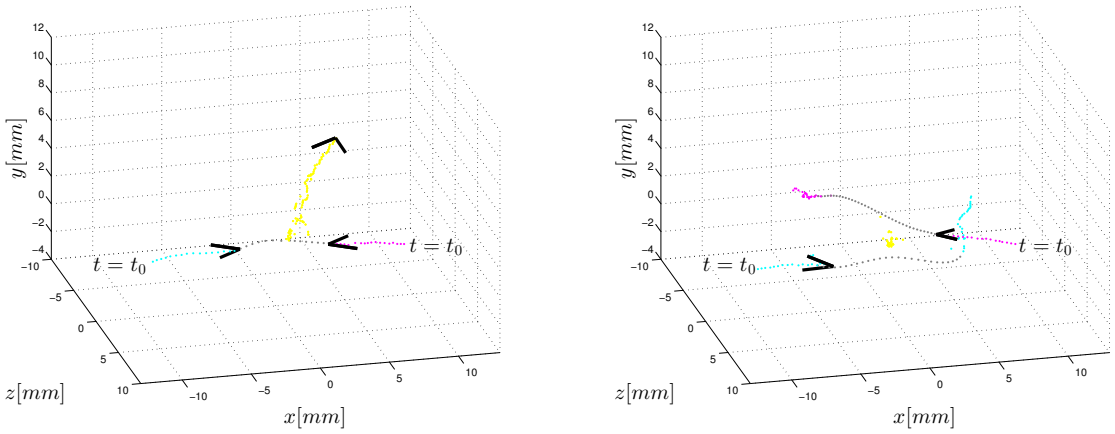

(a) (b)

Figure 4.17: (a) Droplet trajectories for coalescence case at $Re_\lambda = 141$. $We = 67$, $B = 0.25$. (b) Droplet trajectories for coalescence and stretching separation case at $Re_\lambda = 141$. $We = 56$, $B = 0.36$. The droplet injected by the left nozzle is colored cyan and the droplet injected by the right nozzle is colored magenta. During apparent contact or permanent or temporary coalescence the trajectory is colored yellow. The gray dots are interpolations and are only intended as a visual aid.

at values of We larger than 30 and for B in between $0.1 < B < 0.4$. For smaller and for larger values of the impact parameter B it appears as though the coalescence regime only occurs at larger values of We. The occurrence of *coalescence and stretching separation* does not happen below approximately $We \approx 39$ and a lower limit in impact parameter for the occurrence of this regime is $B \approx 0.12$. Finally the two events of coalescence and reflexive separation occur at $We > 70$. A possible explanation of the near absence of events of this type is the fact that events at $B \approx 0$ are very rare, and this together with very large values of We is especially the region where the mentioned events occur.

To interpret the measurements in a way less focused on individual events, the averaged result is plotted in Figure 4.21. The bin for $60 < We < 70$ and $0.4 < B < 0.6$ is manually removed because the two *coalescence and stretching separation* events and four coalescence events are in the author's opinion too few to make statements on the averaged outcome except that initially coalescence occurs. Striking in the averaged results is the non monotonicity of the boundary between the bouncing and the coalescence regime. For head-on collisions the boundary is at $We = 40$. For slightly less head on collisions, with $0.2 < B < 0.4$, the boundary is at a lower value: $We = 30$, and for higher values, $B > 0.4$, it returns to a value of $We = 40$. The regime of coalescence and stretching separation lies between $50 < We < 80$ and $0.2 < B < 0.4$. Head on collisions at very large Weber number lead to coalescence in an averaged sense up to at least $We = 90$.

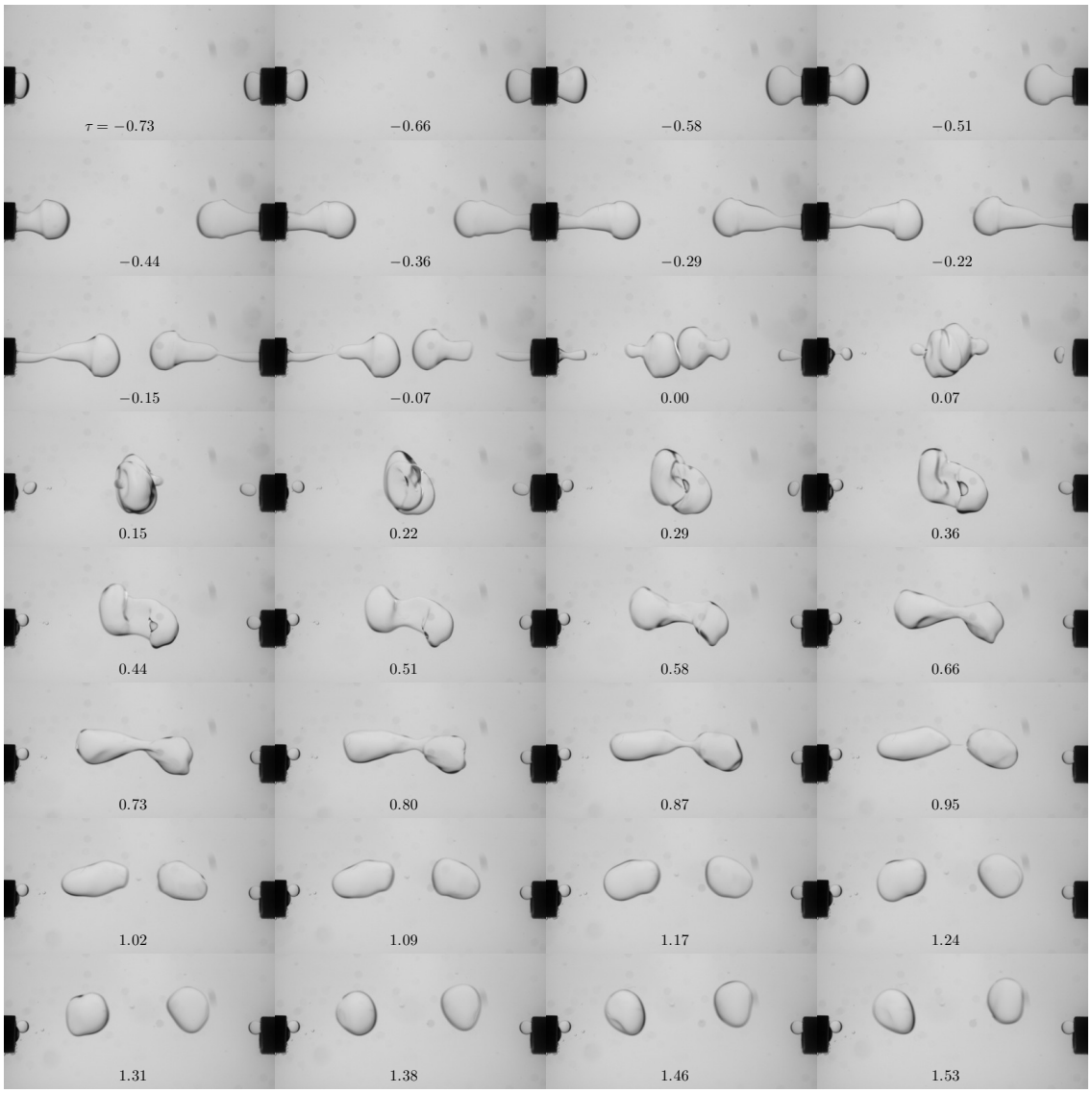

Figure 4.18: Image sequence for coalescence and stretching separation case for $Re_\lambda = 141$. $We = 56$, $B = 0.4$.

4.4 Discussion and conclusions

In the previous sections of this chapter inertial collisions between droplets of silicone oil in a continuous phase that consists of demineralized water are investigated. The kinematic viscosity of the droplets is five times the kinematic viscosity of water. The droplets are imaged using three high speed cameras and the trajectories are determined via a reconstruction based on triangulation. The droplets are injected through two nozzles that are mounted in an optically transparent Von Kármán flow facility. At the center of the flow facility a homogeneous turbulent flow can be created by rotating the discs at the top and

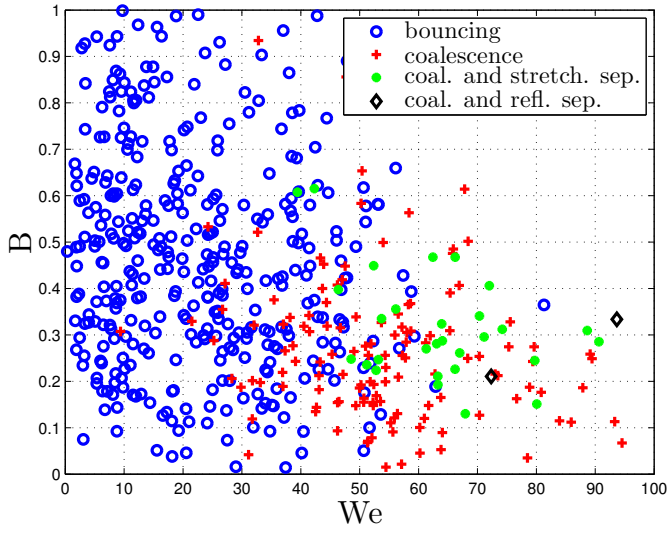

Figure 4.19: Collision outcome in (B, We)-parameter space for $Re_\lambda = 141$.

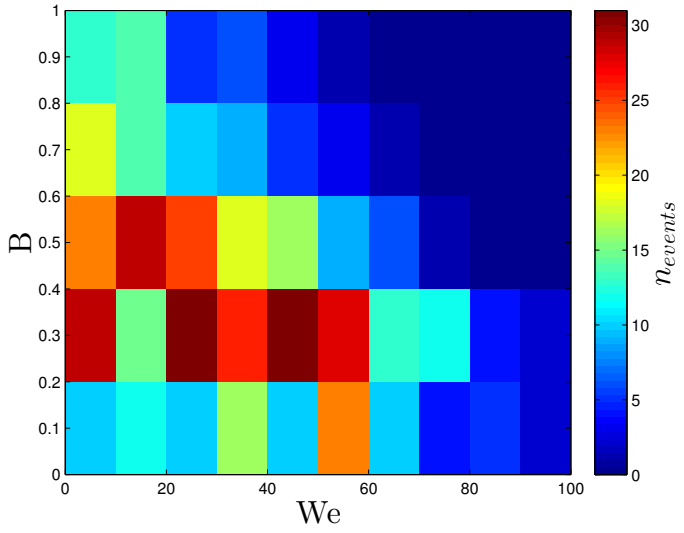

Figure 4.20: Number of events in (B, We)-parameter space for $Re_\lambda = 141$.

the bottom of the facility in opposite direction. Droplet collisions have been performed both during disc rotation, at a Taylor micro scale Reynolds number of $Re_\lambda = 141$ and in a stationary continuous phase ($Re_\lambda = 0$). The main goal of the experiment is to gain insight in the dependency of a possible change in the critical Weber number between the bouncing regime and the coalescence regime on the turbulence. This section is dedicated to the interpretation of the results, first for the case of $Re_\lambda = 0$ and then for the turbulent case $Re_\lambda = 141$.

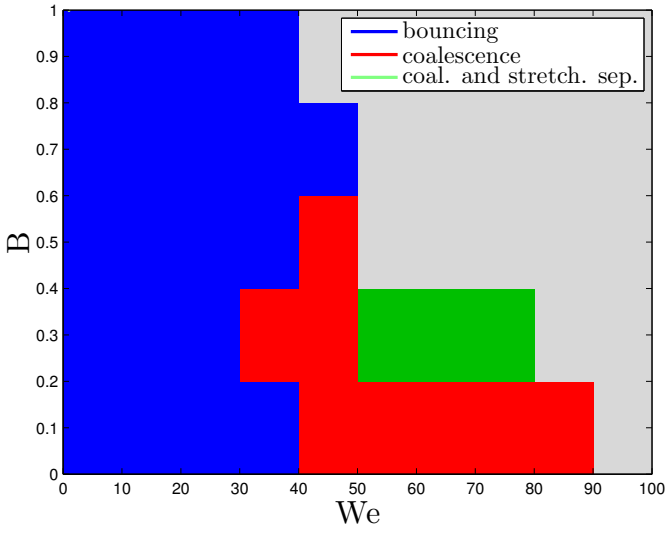

Figure 4.21: Average collision outcome in (B, We)-parameter space for $Re_\lambda = 141$.

For the case of a stationary continuous phase, $Re_\lambda = 0$ the observations are as follows:

1. Three regimes of collision outcome are found. These are: bouncing, coalescence, and coalescence followed by reflexive separation.

2. Clear boundaries between the different regimes of collision outcome are found for $B \approx 0$. For head on collisions the boundary between bouncing and coalescence lies approximately at $We_{II,III} = 20$ and the boundary between the coalescence and the regime of coalescence followed by reflexive separation is at approximately $We_{III,IV} = 77$.

3. The time during which the droplets are in apparent contact in case of a bouncing event is equal to the theoretical viscous droplet oscillation period (Miller and Scriven [57]).

4. The time from the onset of apparent drop contact until rupture of the thin fluid film in between the drops in case of coalescence decreases with increase of We and is approximately equal to $\tau_{drainage} = 5.5\,We^{-0.73}$.

5. Droplet collision experiments at an offset (the value of the impact parameter is larger than zero $B > 0$) carried out under identical circumstances indicate a small slope of of the boundary between the regime of bouncing and the regimes of coalescence (and of coalescence followed by stretching separation): $\frac{\partial B}{\partial We}|_{II,III/IV} \approx 1 \cdot 10^{-2}$ relative to liquid droplets in a gaseous environment. The trend that bouncing is promoted with increase of continuous phase density ρ_c as indicated for droplet collisions in a gas in the work of Qian and Law [68] thus continues for collisions in a liquid.

Among the observed phenomena are the formation of a so called nipple, see Lai et al. [50], and the entrainment of continuous phase liquid inside the drops in two ways, namely via the rear end of the drops during impact and via film rupture in case of coalescence. A final observation is that when performing droplet collisions at a fixed collision frequency, the outcome of the first two or three collisions is not very constant and only after two collisions the outcome remains constant in general. It is possible that a small secondary flow is initiated during the first couple of collisions after which a quasi steady behavior starts.
In case of a turbulent continuous phase with $Re_\lambda = 141$ the main observations are as follows:

6. four types of collision outcomes occurred: bouncing, coalescence, coalescence followed by stretching separation, and coalescence followed by reflexive separation.

7. No sharp boundaries between the different regimes are apparent in the (B, We)-parameter space (see Figure 4.19).

8. In an averaged sense the transition value of the Weber number is $We_{II,III} \approx 40$ for head on collisions ($B = 0$) and on average head on droplet collisions at very high values of the Weber number, $We > 70$, coalesce without separation.

9. Head on collisions ($B = 0$) and events at very large value of the Weber number are rare. In total less than 6 % of the events are at values of the Weber number for which it holds that $We > 70$. The fact that head on collisions are rare is possibly caused by the small chance of identical turbulent velocity fluctuations at the locations of both droplets. An explanation for the fact that events at large values of the Weber number are rare is not easily found.

A final observation for both the case $Re_\lambda = 141$ is that:

10. coalescence at low values of the Weber number $We < 1$ did not occur. A possible explanation for this is mentioned in chapter 5.

It is noted that coalescence events in the case $Re_\lambda = 141$ occur mostly at values of the Weber number $We > 40$. Out of all 527 collisions only eight coalescence events occurred at values of the Weber number below 30. For small values of the impact parameter $B < 0.1$, only one coalescence event occurred for $We < 45$.
The principal aim of the measurements in the present chapter is to quantify a possible change in the critical Weber number between the bouncing regime and the coalescence regime for droplet collisions in a stationary continuous phase as compared to a turbulent continuous phase. To compare the measurements for both cases the results for the case $Re_\lambda = 141$ are shown next to the results for the case $Re_\lambda = 0$ (including the measurements at $B > 0.2$) in Figure 4.22 with equal binning. For head on collisions ($B < 0.1$) the apparent boundary shifts from $We = 20$ to $We = 40$. Collisions with a larger offset,

$0.2 < B < 0.4$, show a remarkable shift of the boundary towards a lower value of the Weber number $We = 30$ for $0.2 < B < 0.4$.
To discuss this shift, knowledge of the measurement accuracy is required. The accuracy is difficult to estimate. It is possible that the accuracy in B is less than the currently adopted empirical estimate of 0.2. When averaging the results using a larger bin size in We and in B, for example $\frac{1}{3}$ in B, the transition Weber number shifts from the current value of $We = 40$ to a value of $We = 30$ for $0 < B < 0.4$. *But even in an averaged sense the boundary at small B between the bouncing and coalescence regimes is never at a smaller value of the Weber number than $We = 30$ for the case $Re_\lambda = 141$.*

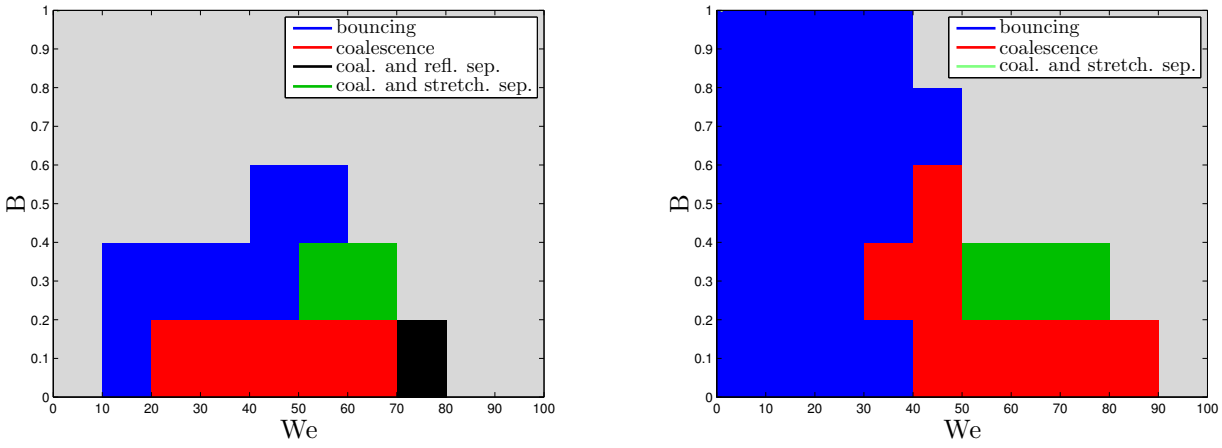

(a) $Re_\lambda = 0$ (b) $Re_\lambda = 141$

Figure 4.22: (a) Average collision outcome in (B, We)-parameter space for $Re_\lambda = 0$. (b) Average collision outcome in (B, We)-parameter space for $Re_\lambda = 141$.

Finding a physical explanation for the observation that droplets in a turbulent Von Kármán flow coalesce at larger values of the Weber number than in a stationary continuous phase is non trivial and speculative at this point. Nevertheless a number of suggestions are now given to explain this shift. The observed collision events occur in a turbulent flow with an average velocity field as shown in Figure 3.11. The radially inward flow along the direction of droplet injection is likely to cause a decrease in velocity of the internal droplet circulation on average. The horizontal inward velocity at the leftmost and rightmost edge of the field of view used for the PIV measurements have magnitudes of approximately $|u| = 0.02$ m/s. The Weber number that on average divides the bouncing and coalescence regimes in a turbulent flow is $We = 40$. The velocities corresponding to this value in the current work are $U_1 = -U_2 = 0.28$ m/s. If one now takes the velocity difference with the average surrounding flow as drop velocity $U_1 = -U_2 = 0.26$ m/s, the Weber number would have a value of $We = 35$. In theoretical and numerical work by Nemer et al. [60] it is shown that the internal droplet flow can significantly influence film drainage. In some cases drainage stagnates entirely. Hindered film drainage due to the outer flow is thus possibly a part of

an explanation for the observed increase of boundary Weber number between the bouncing and coalescence regimes. Remarkable is that such a possible influence of the outer flow is not unique to turbulence.
In general there are not many measurements of inertial droplet collisions in a flowing medium. Conceptually simple experiments on for example droplet collisions in a cross flow or a droplet colliding with a stationary droplet on a nozzle can already shed light on the induced asymmetries.
Finally, there is the possibility of contamination due to surface active agents. It could be that the turbulent mixing of the water distributes surfactants which could be present at isolated locations. Surfactants can immobilize interfaces leading to slower drainage. Because of the thorough cleaning of the facility and the use of new demineralized water on every day of measurements, the probability that surfactants influenced the measurements is considered small.
Next to the investigation of the influence of the influence of the external flow on the collision behavior of droplets, it could be interesting to investigate droplet collisions in a stationary liquid in more detail. One of the possible research questions could be wether the collision outcome really depends only on the Weber number for two given liquids. This can be examined by for example varying the drop size. In doing this it is expected that the nozzle distance has to be varied too in order to make sure the droplets are pinched off before the collision, i.e. a larger distance for larger droplets. Secondly the influence of the viscosity ratio λ on the drainage behavior is of interest. In the current work the viscosity ratio of $\lambda = 4.6$ was selected because the viscosity of the droplets was large enough to stabilize the droplet shape due to dissipation and small enough to attain large values of the Weber number with the employed syringe pumps. Thirdly it might be of interest to investigate the influence of different types of liquid for example by performing a similar experiment with hydrocarbon droplets in water. In this case one has to find hydrocarbons with a suitably low viscosity.

Chapter 5

Conclusions, perspectives and recommendations

The aim of this study was to experimentally investigate the influence of the external flow, specifically turbulent flow in the continuous phase, on the outcome of droplet collisions. The outcome of a collision can be characterized by a critical Weber number separating bouncing and coalescence.
The film drainage process is crucial for the outcome of droplet collisions. If, during drop interaction, the film thickness attains a thickness small enough for attractive intermolecular Van der Waals forces to initiate a liquid bridge between the colliding drops, the drops will coalesce. In order to gain insight in the film drainage process first an experiment on a drop at a two-fluid interface was performed. Secondly an experiment was performed where droplet collisions in a stationary continuous phase were compared with droplet collisions in a turbulent continuous phase. The main conclusions are summarized in this chapter.

5.1 Conclusions

5.1.1 Measurements of liquid film drainage

A drop at a two-fluid interface was investigated. The film thickness, the time until the film ruptures, also referred to as the film drainage time $t_{drainage}$, and the location where film rupture initiated were measured. The measurements were performed at three values of the viscosity ratio λ. The main conclusions are:

1. the film shape is thick at the center with a thin ring surrounding it, also referred to as a dimple.

2. The film thinning is not symmetric; simple models to predict the drainage time are inaccurate with errors in the order of a factor ten.

3. The drainage time $t_{drainage}$ increases with the viscosity ratio λ.

4. Film rupture initiates off-center.

5.1.2 Droplet collision measurements

For the droplet collision measurements the collision outcome was recorded, and the Weber number We and non dimensional velocity vector offset B were determined for hundreds of collisions of silicone oil drops in an ambient phase consisting of demineralized water. This was done for the case where the surrounding fluid was quiescent, denoted as $Re_\lambda = 0$, and for the case where the surrounding fluid was turbulent. The turbulence was generated by two counter rotating discs in a Von Kármán flow, and this case is denoted as $Re_\lambda = 141$. The turbulent Von Kármán flow is on average axisymmetric compressional in the direction of the nozzles, centered between the nozzles. The Taylor micro scale of the flow is measured to be $\lambda_T = 2.2$ mm and the Kolmogorov length scale is $\eta_K = 0.099$ mm. In the case $Re_\lambda = 0$ the time duration that the droplets are in apparent contact, denoted by $t_{interaction}$, and the drainage time $t_{drainage}$ are also determined. For all collisions the ratio of viscosities is $\lambda = 4.6$ and the volume equivalent drop radius is $R = 2.8$ mm. The main conclusions for the droplet collision measurements are now stated.

1. Droplet collisions in a liquid are similar in a phenomenological sense to droplet collisions in a gas as reported by Qian and Law [68]; see Figures 4.11 and 4.12.

2. In case a collision results in a bouncing event, the interaction time $t_{interaction}$ is approximately equal to the theoretical drop oscillation period as given by Miller and Scriven [57].

3. In case a collision results in a coalescence event, the drainage time $t_{drainage}$ decreases with increase of the Weber number. An empirical fit is presented in section 4.3.1, Figure 4.13.

4. The presence of turbulent continuous phase flow fluctuations influences the outcome of droplet collisions in a liquid significantly, specifically: bouncing is promoted.

5.2 Perspectives

To make it possible to interpret the results of the current research in a broader sense, here a comparison is made with similar experiments from literature. First the findings from the droplet collision measurements in chapter 4 are compared to two other droplet collision experiments. The main differences in the two other cases are in the ratio of viscosities λ in the first case and in the fact that the film medium is a gas in the second case. After this possible physical consequences are discussed.
In Figure 5.1 the interaction and drainage time from the measurements as discussed in chapter 4 are plotted together with values as taken from the work of Qian and Law [68] and from the PhD thesis of Kim [40] on linear and logarithmic axes. The times are taken

from the image sequences presented in both works and from written values. The experiment by Qian and Law involved drops of tetradecane with a diameter of approximately 150 μm in atmospheric nitrogen, and the experiment of Kim involved drops composed of a mixture of glycerol and water with a diameter of approximately 8 mm and a viscosity of 6.7 mPa s and the continuous phase consisted of silicone oil with a viscosity of approximately 48 mPa s. The three bouncing cases of Kim show that the interaction time is approximately 1.13 (two occurrences) and 1.06 times the drop oscillation period. The error bars for the data by Kim and Longmire in Figure 5.1 are based on the imaging frequency and are smaller than the symbols. For one bouncing case from the work of Qian and Law the interaction time is 1.13 times the drop oscillation period, and for the bouncing case at low Weber number the interaction time is 1.547 times the drop oscillation period. The error bars in the data from Qian and Law [68] are taken from the time between the images.
There are only a limited number of cases presented in the work by Kim from which the drainage times can be obtained, so it is hard to draw conclusions from these data. The drainage times in this case are smaller than the drainage times from the measurements as reported in chapter 4 of the present work. The Weber number on the boundary between bouncing and coalescence appears to be at $We = 10$, which is approximately equal to the corresponding value for the measurements of Qian and Law for tetradecane. The first observation is that the normalized drainage time for the coalescence case at very low value of the Weber number, $We = 0.2$, is larger than one. The drainage times for the cases where $We > 10$ in the work of Qian and Law [68] decrease faster with increase of the Weber number than the corresponding values from chapter 4 below $We \approx 30$, and these are relatively constant for larger values of the Weber number. A fit to the data from the work by Qian and Law [68] and to the data in Figure 4.13 from chapter 4 leads to the following estimates for the drainage time:

$$\tau_{drainage,Qian\&Law} \approx 15 \cdot 10^3 \, We^{-1.79}, \tag{5.1}$$

and

$$\tau_{drainage,Oldenziel} \approx 5.5 \, We^{-0.73}, \tag{5.2}$$

see Figure 4.13. Note that the data point from the work by Qian and Law at the lowest Weber number is a coalescence at very low Weber number (regime I) and is thus not used in the fit. At the time of writing no explanation of the powers of the Weber number in the estimates 5.1 and 5.2 in terms of physical phenomena was found.
To extend the obtained picture of droplet collisions as shown in Figure 5.1 it is possible to construct a plot where more viscous droplet collisions are depicted. Instead of using the Weber number here the relative drop velocity U_{rel} is non dimensionalised via a multiplication by the drop viscosity μ_d divided by the interfacial tension σ in a capillary number: $Ca_d = \mu_d U_{rel}/\sigma$. The logarithm of the drainage time is plotted versus the capillary number on a logarithmic scale in Figure 5.2. It is remarkable that the data from Kim [40] is virtually indistinguishable from the data from chapter 4 of this thesis in this plot. The additional data is digitized from the work of Yoon et al. [88], and from Klaseboer et al. [43]. In the measurements of Yoon et al. two drops were collided in a viscous compressional

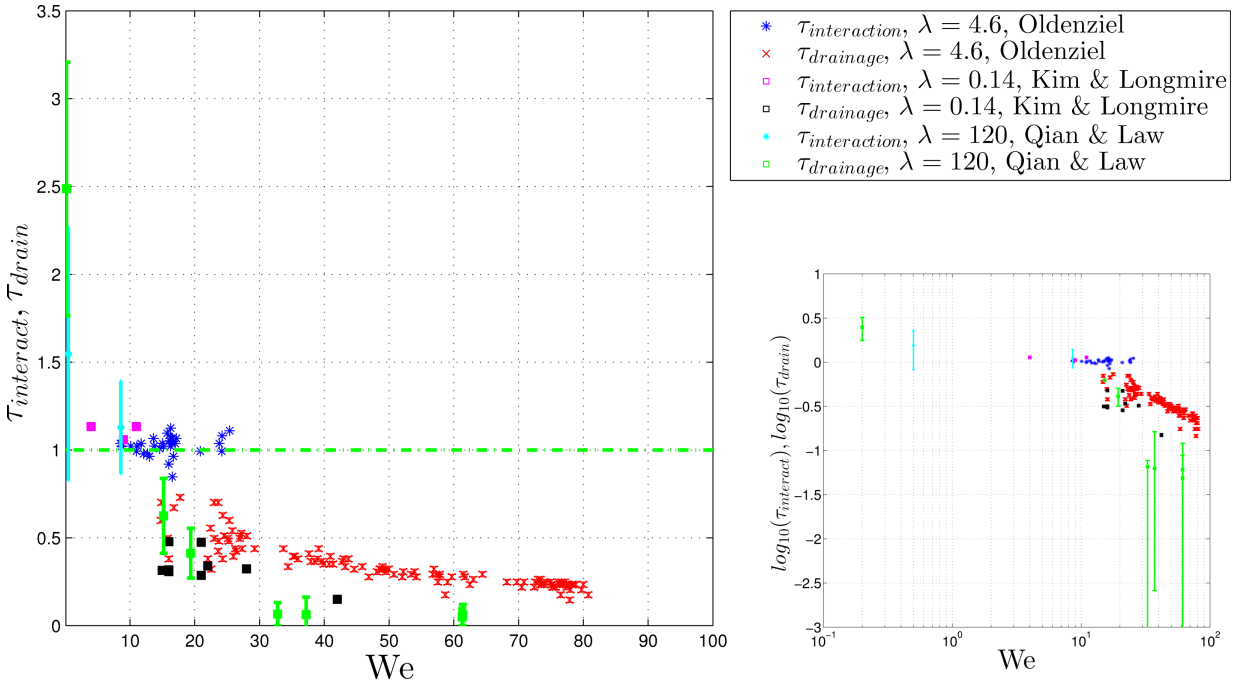

Figure 5.1: Drainage and interaction times from Qian and Law [68] and Kim [40] versus *We* compared to those as measured and reported in chapter 4. Left: linear axes, right: logarithm of the drainage and interaction times versus *We* on a logarithmic scale.

flow in a small four roll mill at different values of the viscosity ratio λ. In the original work of Yoon et al. [88] the data is plotted using a capillary number based on the continuous phase viscosity, but here the capillary number is based on the drop viscosity. In the work of Klaseboer et al. two drops which are positioned on nozzles are collided using a traverse at a relative velocity of 2 μm/s. A boundary integral type of model gave good agreement with experimental data in case the interfaces were assumed to be immobile. The drainage time for the data from Klaseboer et al. is constructed using the model for collisions at constant approach velocity and mobile interfaces from Abid and Chesters [5]. This model is also mentioned in [12] and agrees best with the viscosity ratio of $\lambda = 0.5$. In this model the minimum dimensionless film thickness decays approximately as: $h^*_{min} \approx 4.8(t^*)^{-1.6}$ after the dimple has established itself. The data from Klaseboer et al. for the case $\lambda = 0.5$ is used and the drainage time is taken to be the time it takes for the film thickness to go from approximately 0.13 μm to 60 nm using the mentioned model, and they are intended for indicative purposes. The final thickness of 60 nm is based on measurements by Burrill and Woods [18]. The drop oscillation period is computed, using the model for two fluids at high viscosity by Miller and Scriven [57]. It is remarkable that the drainage times $\tau_{drainage}$ are larger than the drop oscillation times for the viscous droplet collisions. This is in contrast with the inertial droplet collisions shown in Figure 5.2 and in agreement with the low inertial case from the data of Qian and Law [68] in the same figure. For low inertial or

viscous collisions leading to coalescence the interaction time is thus larger than the droplet oscillation period. It is likely that the interaction time can only exceed the period of oscillation of the droplets in case an external force causes the drops to interact. The drainage times for such viscous droplet collisions are on the order of seconds to minutes and thus much larger than $\tau_{interaction}$.
The viscous drop collision measurements by Klaseboer and the inertial drop collisions by Qian and Law [68], Kim [40] and Kim and Longmire [42] and those by the present author are separated by approximately four decades in the capillary number. It is thus clear that successful application of a Stokes type boundary integral method for inertial collisions at large values of Ca_d is unlikely. The agreement of simple models with experimental data from Yoon et al. at low value of the capillary number is discussed in Baldessari and Leal [9], and it is found that overall flow induced drop deformation plays a role in this case. The influence of strain in the continuous phase flow and the influence of body forces bringing the drops together was not known when the mentioned works were published. A straining flow can arrest film drainage completely, see Figure 1.6, whereas the film thickness in case body forces bringing the drops together can display algebraic film thinning versus time; see references [60, 61, 87].

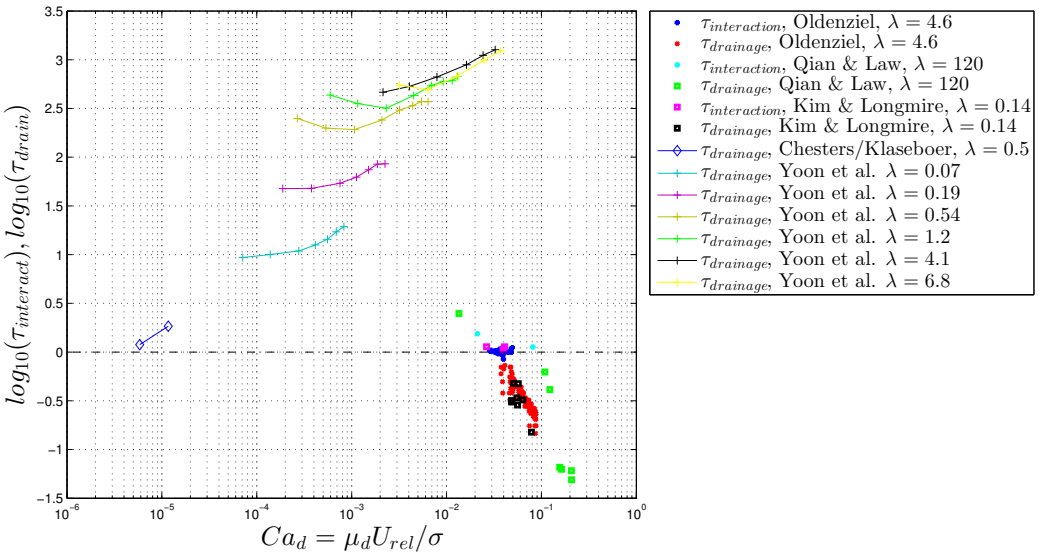

Figure 5.2: Drainage times versus capillary number for inertial and viscous collisions. Including data from Qian and Law [68], Kim and Longmire [42], Klaseboer et al. [43] via the model from Abid and Chesters [5], and Yoon et al. [88].

The final conclusion from section 5.1.2 can be rephrased and abbreviated as: *bouncing is promoted in case of droplet collisions in a turbulent flow.* The turbulent flow in question is on average axisymmetric compressional in the direction of the nozzles, centered between the nozzles. One of the possible part of an explanation for the hindered drainage is an effect

of the large scale internal drop flow on the film drainage, similar to the effect reported by Nemer et al. [60] for viscous drop collisions. One way to test this hypothesis would be to construct a setup where the nozzles are oriented vertically and the drops are thus collided against the local average flow direction. If the mentioned hypothesis is valid and the effect is of similar magnitude as the hindrance as experienced during the measurements as described in chapter 4, a larger fraction of the collisions will lead to coalescence. A sketch of the internal drop flow in case of possible enhanced drainage is shown in Figure 5.3. It is also possible that the strain caused by turbulent velocity fluctuations influences the internal drop flow and hinders the drainage of the thin film.

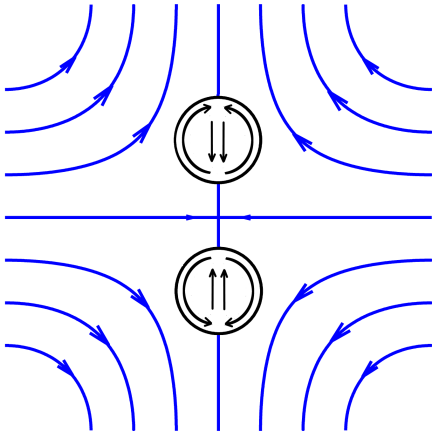

Figure 5.3: Sketch of flow field in case of possible enhanced drainage. In the sketch the drops are on vertical trajectories towards each other.

A last property to take into account is the density difference between the droplets and the continuous phase $\triangle\rho = \rho_c - \rho_d$. It is possible that in microgravity the boundaries between bouncing and coalescence and between coalescence and coalescence-followed-by-reflexive-separation shift to lower values of the Weber number as is suggested in private communication by the author with Longmire [53]. In general the effect of the density difference on the collision outcome is not known, although more information can possibly be found in the work of Kim [40], and could be a topic of interest for further research.
Now a practical example is discussed. In order to sketch a possible consequence of the hindered or promoted coalescence due to the large scale flow the outcome of droplet collisions for water drops in air under atmospheric conditions is depicted in Figure 5.4 as adapted from the work of Qian and Law [68].
The formation of warm rain can be subdivided in three processes according to Grabowski [31]. First small aerosol particles, referred to as cloud condensation nuclei (CCN), are activated until the supersaturation begins to decrease. After the activation the nuclei grow due to diffusion of water vapor. When drops reach radii of approximately 40 μm gravitational collisions become effective and larger drops grow due to collection of smaller drops via collision coalescence. In reality one of the poorly understood processes is how

the drops attain sizes of approximately 40 μm when growth by condensation maximally produces drops with a size of 20 μm. This is referred to as the condensation-coalescence bottleneck or the size gap. Here only gravitational collisions are considered.
Figure 5.4 indicates that collisions of water drops often lead to initial coalescence, but for collisions at a non dimensional offset larger than $B = 0.6$ a significant area of approximately 50% of the part of the (B, We)-parameter space that has been measured leads to bouncing events. A more realistic analysis incorporates that typical sedimentation velocities for water drops in clouds are approximately equal to 1 cm/s. This leads to Weber numbers in the order of $We \approx 1 \cdot 10^{-4}$ or capillary numbers of similar magnitude $Ca_d \approx 1 \cdot 10^{-4}$. It is thus expected that these collisions are thus not in regime III but in coalescence regime I in the general regime map of Figure 1.5. If the enhanced drainage, as found analytically and numerically by Nemer et al. [60], for collisions due to body forces also exists in reality, it should lead to an increase of the area of the coalescence regime in the (B, We)-parameter space, and thus to enhanced coalescence. It is possible that this enhanced coalescence effect plays a role in the formation of warm rain.

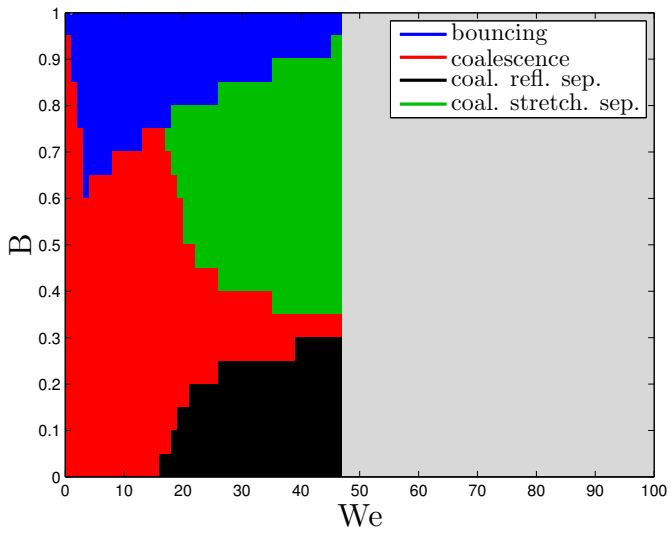

Figure 5.4: Droplet collision outcome diagram for water drops in atmospheric nitrogen (as adapted from Figure 6a in Qian and Law [68]).

It is difficult to directly translate the effect of turbulence as found in chapter 4 on droplet coalescence but an attempt is made here. The effect that is found is that the boundary between the bouncing regime and the coalescence regime in terms of the Weber number shifts to higher values of the Weber number in case of a turbulent medium. Not all media display bouncing at head-on impact, so only for media which do show a bouncing regime for head on impact something can be stated. This is often the case for hydrocarbon drops in a gas which can be subject to increased pressure. An application that comes to mind is fuel injection in a combustion engine or in rocket boosters. In some types of rocket boosters

the fuel and the oxidizer are combined by injecting them as jets that are impinging on each other. Under certain flow conditions, specifically at higher flow velocities, the liquid sheet, that is formed by the impinging jets, breaks up in droplets that will interact. If one is interested in for example typical drop size, knowledge of droplet collisions in conditions where there is a flow in the surrounding medium is required. Drop size can significantly affect the combustors performance. It is likely that coalescence is hindered as compared to collisions in a stationary medium. Note that all regimes in the (B, We)-parameter space play a role in the droplet size distribution after collisions.

5.3 Recommendations

The recommendation for further research is divided in two categories: recommendations for further physical research and recommendations to improve or refine the research as presented in this thesis. Suggestions for experiments with different levels of complexity in order to investigate issues arising from the current research are:

1. In chapter 2 of this thesis, it is shown that for a drop at a two-fluid interface simple drainage models do not give accurate estimates for the drainage time for values of the Bond number of $Bo \approx 1$ and for viscosities not exceeding $\mu = 51.1$ mPas. It is expected that these parallel disc models yield better estimates of the drainage time if the Bond number is much smaller than one, $Bo \ll 1$, and if the liquids are highly viscous. In this case an experiment where drainage times can be determined by determining the time until the drop coalesces can be performed, possibly at different values for the viscosity ratio. A possible aim of the measurements can be to determine a critical Bond number above which the estimates of the drainage time from the parallel disc model are off by a specified percentage.

2. In chapter 4 of this thesis, it is shown that the drainage time for the film between two colliding droplets at a viscosity ratio of $\lambda = \mu_d/\mu_c \approx 4.6$ decays with increase of the Weber number approximately as $\tau_{drainage} \approx 5.5\,We^{-0.73}$ when non dimensionalised with the droplet oscillation period. Twelve data points were extracted from the work of Kim [40] and Kim and Longmire [42] for a viscosity ratio of $\lambda \approx 0.14$. In order to differentiate between continuous phase density (ρ_c) effects and continuous phase viscosity (μ_c) effects an increase in drainage time data for this ratio of viscosities can be very useful. The goal would be to determine drainage times for inertially colliding droplets over a significant range in the Weber number at a low viscosity ratio ($\lambda < 0.3$). Another potentially important parameter to investigate is the influence of the collision angle on the Weber number dividing bouncing and coalescence.

3. In chapter 4 of this thesis, it is shown that bouncing is promoted in case of droplet collisions in a turbulent flow. If the promoted bouncing is indeed caused by the compressional flow in the direction of the nozzles centered between the nozzles, an experiment with vertically oriented nozzles would lead to enhanced coalescence. Quantification

of this potential effect is the final recommendation potentially along with analytical, numerical and experimental analysis of possible scaling with the average flow velocity or strain rate.

Possible enhancement or refinement of the work presented in this thesis has to incorporate enhancements to the experimental setup for the droplet collision experiments. Three possibilities are:

1. In the measurements as described in chapters 3 and 4 of this thesis, droplet fluid is injected in a flow that is driven by two counter-rotating discs. The injected fluid collects above the top disc. When this fluid reaches a certain amount, the disc fragments the dispersed fluid, and it is recirculated into the measurement domain, where it hinders drop detection via image processing. Also, if too much liquid collects at the top, the flow facility overflows and thus also render drop detection in image processing to become almost impossible. It is thus desirable to equip the current experimental setup with automatic suction of the liquid collecting at the top.

2. The DC motors driving the discs and the control of the disc rotation velocity currently occurs manually, i.e. just before and after every collision the rotation velocities are checked at the displays of the optical timing devices. In order to facilitate the measurement process it would be convenient to have feedback control on the DC motors. Improvement of the motors can also result in an increase of the accuracy in disc rotation velocity.

3. If the previous two recommendations are implemented one can reason as follows: in order to attain an improved estimate of the Weber number for the boundary between the bouncing and coalescence regimes, the number of measurements must be larger than the current 527. To achieve a very large number of measurements, ideally the measurements should be automated.

Appendix A

Fluid properties for drop at two-fluid interface

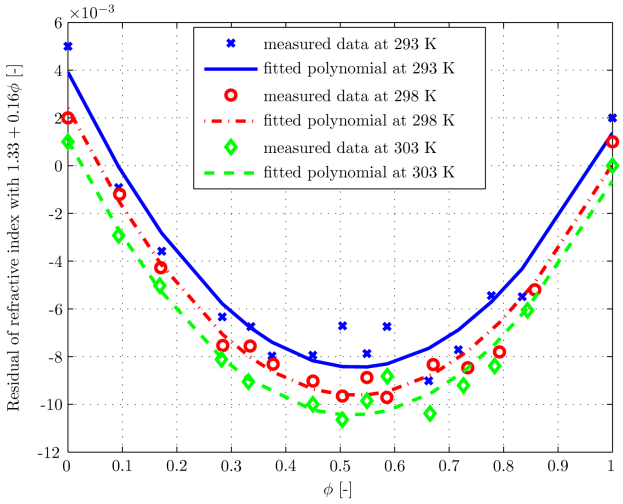

Figure A.1: Residual of measured refractive index n_{meas} of the water/glucose syrup mixture to $n = 1.33 + 0.16\phi$ versus mass fraction of glucose syrup (ϕ) at three temperatures. $Res = n_{meas} - n$. Symbols represent measured data at different temperatures. Lines are fitted second order polynomials. In the fitted polynomial for the measurements at $T = 303K$ one inconsistent measurement was disregarded.

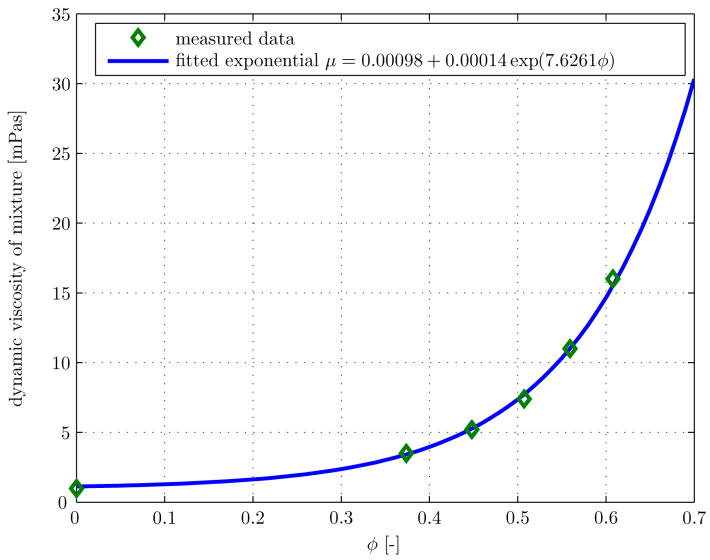

Figure A.2: Dynamic viscosity of water/glucose syrup mixture as a function of mass fraction ϕ at a temperature of 298 K. Symbols represent measurement data; the solid line is an exponential function fitted to the measurement data.

Appendix B

Determination of the interfacial tension

B.1 Interfacial tension for a drop at a two-fluid interface

The method to determine the interface tension for the measurements of the drop at the two-fluid interface is explained in this section. In Figure B.1 the definitions of the variables are given.
To relate the pressure p_1 at height h_2 below the unperturbed interface far from the droplet to the pressure p_0 at height h_1 above the interface and also far from the droplet, the assumption of hydrostatic equilibrium yields for p_1:

$$p_1 = p_0 + \rho_1 h_1 g + \rho_2 h_2 g. \tag{B.1}$$

Next the Young-Laplace equation is applied twice to obtain the pressure p_3 at the top of the droplet.

$$p_3 = p_2 + \frac{2\sigma}{R_1} = p_0 + \frac{4\sigma}{R_1} \tag{B.2}$$

Here it is assumed that the the radii of curvature of the top and the bottom of the thin liquid film between the drop and the top phase to be identical, and we neglect the hydrostatic contribution of this thin film. Now the pressure p_4 at the bottom of the droplet is equal to:

$$p_4 = p_3 + \rho_1 g(h_1 + h_2), \tag{B.3}$$

and for the pressure p_1 it holds that:

$$p_1 = p_4 - \frac{2\sigma}{R_2} = p_0 + \frac{4\sigma}{R_1} + \rho_1 g(h_1 + h_2) - \frac{2\sigma}{R_2}. \tag{B.4}$$

Equating the two expressions for p_1 now yields an expression for the interface tension σ:

$$\sigma = \frac{(\rho_2 - \rho_1)\, g h_2}{\frac{4}{R_1} - \frac{2}{R_2}}. \tag{B.5}$$

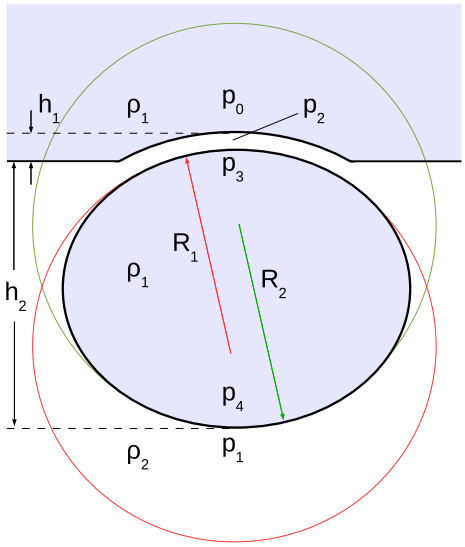

Figure B.1: Droplet variables.

B.2 Interfacial tension for droplet collision measurements

The interfacial tension for the droplet collision measurements is determined via a method in which use is made of a correction to the pendant drop method. In the pendant drop method the balance between gravitational forces and interfacial tension forces just before pinch off of a drop from a nozzle leads to an estimate for the interfacial tension.

$$\sigma = \triangle\rho g \frac{V}{2\pi R_{neck}}. \tag{B.6}$$

Here, $\triangle\rho$ is the density difference $\rho_c - \rho_d$ between the continuous phase and the drop, g is the gravitational acceleration, V is the drop volume, and R_{neck} is the radius of the neck just before the pinch off starts. In Figure B.2 the geometry of the drop just before pinch off is depicted.
The balance of gravitational forces, pressure forces and interfacial tension forces on the control volume which is indicated by the dashed blue line in Figure B.2, leads to an expression for the interfacial tension that is now derived.
If the pressure at point 1 in Figure B.2 is denoted by p_1 and the pressure at points 2 and 3 are denoted by p_2 and p_3, then p_2 is given by the pressure jump due to the curvature of the interface at the top of the drop R_{top}:

$$p_2 = p_1 + \frac{2\sigma}{R_{top}}. \tag{B.7}$$

The pressure in point 3 is equal to the pressure at point 2 plus the increase from the

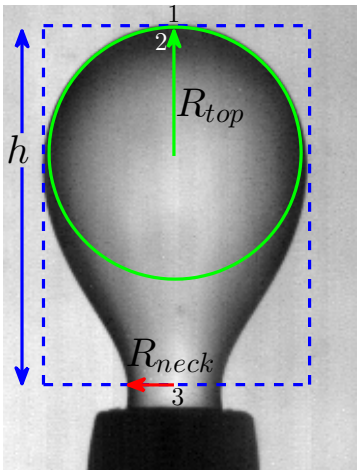

Figure B.2: Sketch with definition of geometric quantities for pendant drop method.

hydrostatic contribution due to the height difference h:

$$p_3 = p_2 + \rho_d g h = p_1 + \frac{2\sigma}{R_{top}} + \rho_d g h. \tag{B.8}$$

The body forces on the control volume are given by F_z:

$$F_z = -\rho_d g V - \rho_c g \left(h\pi R_{top}^2 - V \right). \tag{B.9}$$

The total pressure force working on the control volume is given by F_p:

$$F_p = -p_1 \pi R_{top}^2 + (p_1 + \rho_c g h) \left(\pi R_{top}^2 - \pi R_{neck}^2 \right) + p_3 \pi R_{neck}^2, \tag{B.10}$$

and the interfacial tension force working on the control volume is given by F_σ:

$$F_\sigma = -2\pi R_{neck}. \tag{B.11}$$

Equilibrium of forces together with the derived expression for the pressure at point 3 in equation B.2 leads to:

$$\Sigma F = F_z + F_p + F_\sigma = \triangle \rho g \left(V - h\pi R_{neck}^2 \right) - 2\pi\sigma R_{neck} \left(1 - \frac{R_{neck}}{R_{top}} \right) = 0. \tag{B.12}$$

Thus the expression for the interfacial tension is given by:

$$\sigma = \frac{\triangle \rho g \left(V - h\pi R_{neck}^2 \right)}{2\pi R_{neck} (1 - \frac{R_{neck}}{R_{top}})}. \tag{B.13}$$

The nozzle for the interface tension measurements is of the same dimension as the nozzles used in the droplet collision measurements. The inner diameter is 3.0 mm and the outer diameter is 5.0 mm. A computer controlled syringe pump (Hamilton 500B) with a 25 ml syringe is used to inject the droplet fluid. Near the point of pinch off the injection is performed in discrete steps of the minimum step size of the pumps, which corresponds to an amount of 0.0238 ml. The process is imaged using a Photron APX-RS camera with a 10 bit CMOS sensor array and a resolution of 1024×1024 pixels. A projector using a halogen lamp in combination with a diffusing sandblasted plexiglas plate is used to provide lighting from the back. The imaging frequency is 125 Hz and the magnification is $M = 0.26$. The neck width R_{neck} is determined by image processing and is equal to half the minimum drop diameter determined by thresholding the image where the pinch off starts. The radius of curvature at the top R_{top} is the radius of the circle obtained by a least squares fit to nine manually selected points on the top edge of the drop. The drop volume at the pinch off frame is determined by thresholding the image of the drop above the neck and assuming cylindrical symmetry. In order to obtain an accurate estimate, ten measurements are performed, and the final value is the average of the ten obtained values. The density of the drop liquid is obtained from the Wacker AK5 silicone oil product sheet and is $\rho_d = 920$ kg/m^3, and the density of the demineralized water is taken as $\rho_c = 997$ kg/m^3. The acceleration of gravity is 9.8 m/s^2.

An example of a sequence of acquired images during a measurement is shown in Figure B.3. It is important to note that the moment that the pinch off starts is defined to be the moment when the vertical acceleration first becomes non zero. This is before the actual pinch off. In Figure B.3 the time of the frame on which the different quantities are determined is put to zero. The actual pinch off occurs at a time between 0.14 s and 0.16 s. In order to quantify possible changes in interfacial tension due to chemical reactions in the continuous phase liquid (water) over a longer time, the interfacial tension is remeasured 38 days after the first measurement.

The resulting values for the interfacial tension are tabulated in Table B.2 for both methods. The uncertainties are the standard deviations in the interface tension over the ten measurements. For all results in chapter 4 the value of the interfacial tension is thus taken to be $\sigma = 41$ mN/m. Results for the measurements of the interfacial tension for the case when the water was exposed to air for 38 days are denoted by σ_{aged} and are approximately five percent smaller than the non-aged values in case of the corrected method.

Table B.1: Interfacial tension as determined via pendant drop method and corrected pendant drop method.

method	regular pendant drop	corrected pendant drop
σ (mN/m)	32.9 ± 1.1	40.7 ± 1.0
σ_{aged} (mN/m)	30.6 ± 0.9	38.7 ± 1.2

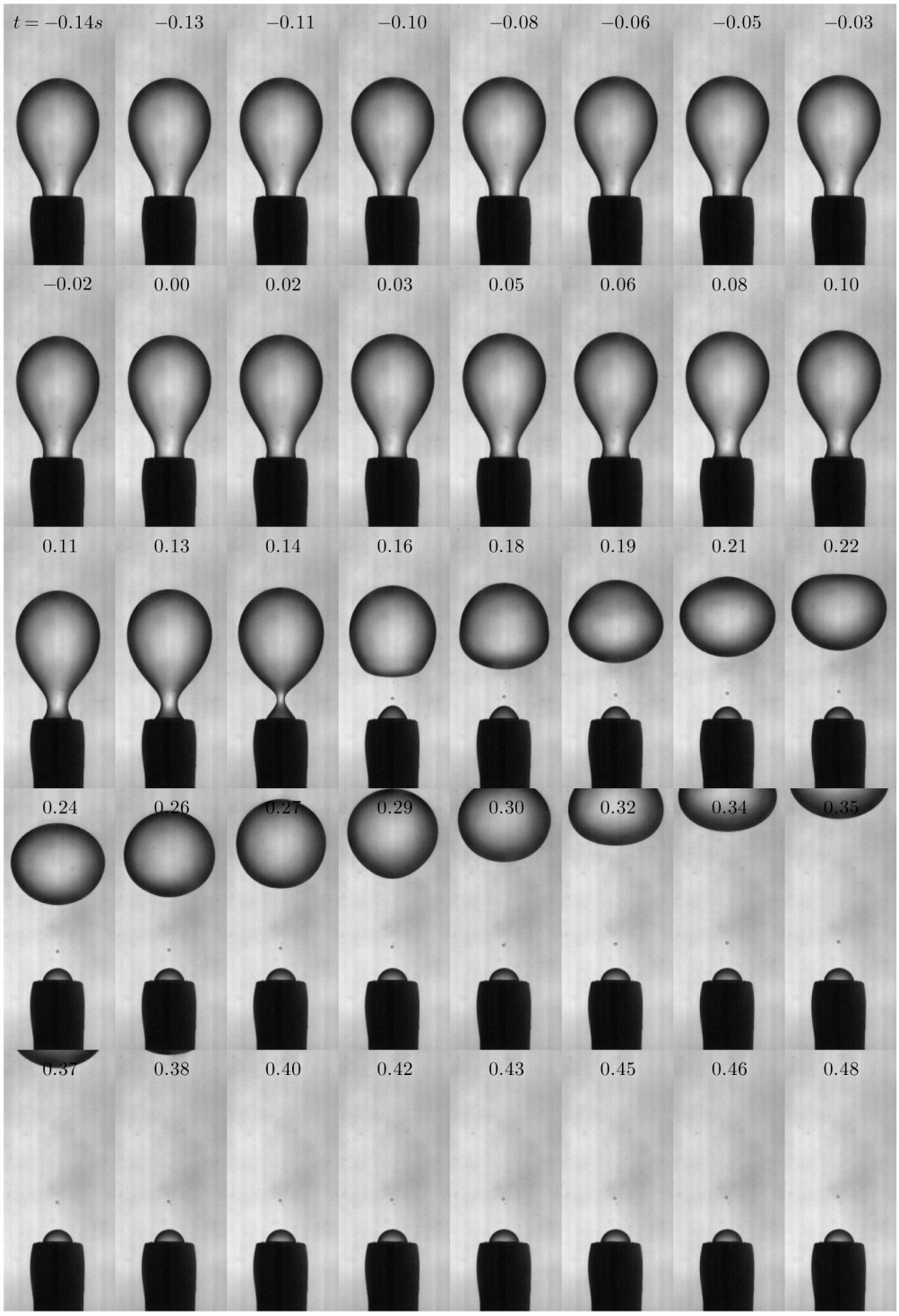

Figure B.3: Image sequence for interfacial tension measurement. One in every two acquired images is shown.

Bibliography

[1] Geomalgorithms.com. `http://geomalgorithms.com/a07-_distance.html`. Accessed: 2013-04-23.

[2] D.G.A.L. Aarts, H. N.W. Lekkerkerker, H. Guo, G.H. Wegdam, and D. Bonn. Hydrodynamics of droplet coalescence. *Phys. Rev. Lett.*, 95:164503, 2005.

[3] D.G.A.L. Aarts and H.N.W. Lekkerkerker. Droplet coalescence: drainage, film rupture and neck growth in ultralow interfacial tension systems. *J. Fluid. Mech.*, 606:275, 2008.

[4] D.G.A.L. Aarts, M. Schmidt, and H.N.W. Lekkerkerker. Direct visual observation of thermal capillary waves. *Science*, 304:847, 2004.

[5] S. Abid and A.K. Chesters. The drainage and rupture of partially-mobile films between colliding drops at constant approach velocity. *Int. J. Multiphas. Flow*, 20:613, 1994.

[6] J.R. Adam, N.R. Lindblad, and C.D. Hendricks. The collision, coalescence, and disruption of water droplets. *J. Appl. Phys.*, 39:5173, 1968.

[7] R.J. Adrian and J. Westerweel. *Particle image velocimetry*. Cambridge Univ Press, 2011.

[8] N. Ashgriz and J.Y. Poo. Coalescence and separation in binary collisions of liquid drops. *J. Fluid Mech.*, 221:183, 1990.

[9] Fabio Baldessari and L Gary Leal. Effect of overall drop deformation on flow-induced coalescence at low capillary numbers. *Phys. Fluids*, 18:013602, 2006.

[10] G. K. Batchelor. Note on a class of solutions of the Navier-Stokes equations representing steady rotationally-symmetric flow. *Q. J. Mech. Appl. Math.*, 4:29, 1951.

[11] G. K. Batchelor. *An introduction to fluid dynamics*. Cambridge Univ Press, 2000.

[12] I.B. Bazhlekov, A.K. Chesters, and F.N. Van de Vosse. The effect of the dispersed to continuous-phase viscosity ratio on film drainage between interacting drops. *Int. J. Multiphas. Flow*, 26:445, 2000.

[13] B.P. Binks and T.S. Horozov. *Colloidal particles at liquid interfaces*. Cambridge Univ Press, 2006.

[14] A. D. Bordoloi and E. K. Longmire. Effect of neighboring perturbations on drop coalescence at an interface. *Phys. Fluids*, 24:062106, 2012.

[15] W. Bouwhuis, R.C.A. van der Veen, T. Tran, D.L. Keij, K.G. Winkels, I.R. Peters, D. van der Meer, C. Sun, J.H. Snoeijer, and D. Lohse. Maximal air bubble entrainment at liquid-drop impact. *Phys. Rev. Lett.*, 109:264501, 2012.

[16] P.R. Brazier-Smith, S.G. Jennings, and J. Latham. The interaction of falling water drops: coalescence. *P. Roy. Soc. Lond. A Mat.*, 326:393, 1972.

[17] N. Bremond, A.R. Thiam, and J. Bibette. Decompressing emulsion droplets favors coalescence. *Phys. Rev. Lett.*, 100:24501, 2008.

[18] K.A. Burrill and D.R. Woods. Film shapes for deformable drops at liquid-liquid interfaces. II. The mechanisms of film drainage. *J. Colloid Interf. Sci.*, 42:15, 1973.

[19] A.K. Chesters. The modelling of coalescence processes in fluid-liquid dispersions:-A Review of Current Understanding. *Chem. Eng. Res. Des.*, 69:259, 1991.

[20] B.K. Chi and L.G. Leal. A theoretical study of the motion of a viscous drop toward a fluid interface at low reynolds number. *J. Fluid Mech.*, 201:123, 1989.

[21] R. Clift, J.R. Grace, and M.E. Weber. *Bubbles, drops, and particles*. Academic Press, Inc., New York, 1978.

[22] E. Coyajee and B.J. Boersma. Numerical simulation of drop impact on a liquid-liquid interface with a multiple marker front-capturing method. *J. Comput. Phys.*, 228:4444, 2009.

[23] R.H. Davis, J.A. Schonberg, and J.M. Rallison. The lubrication force between two viscous drops. *Phys. Fluids*, 1:77, 1989.

[24] G. Debrégeas, P.G. De Gennes, and F. Brochard-Wyart. The life and death of" bare" viscous bubbles. *Science*, 279:1704, 1998.

[25] R. Delfos, U. Miessner, E. Coyajee, R. Lindken, and J. Westerweel. An oil droplet colliding with an oil-water interface: An experimental flow facility for the validation of numerical simulation data. In *Euromech Colloquium*, volume 479, 2006.

[26] C.D. Eastwood, L. Armi, and J.C. Lasheras. The breakup of immiscible fluids in turbulent flows. *J. Fluid Mech.*, 502:309, 2004.

[27] J. Eggers, J.R. Lister, and H.A. Stone. Coalescence of liquid drops. *J. Fluid Mech.*, 401:293, 1999.

[28] G.E. Elsinga, R.J. Adrian, B.W. Van Oudheusden, and F. Scarano. Three-dimensional vortex organization in a high-reynolds-number supersonic turbulent boundary layer. *J. Fluid Mech.*, 644:35, 2010.

[29] G.E. Elsinga, F. Scarano, B. Wieneke, and B.W. Van Oudheusden. Tomographic particle image velocimetry. *Exp. Fluids*, 41:933, 2006.

[30] B. Gopalan, E. Malkiel, and J. Katz. Experimental investigation of turbulent diffusion of slightly buoyant droplets in locally isotropic turbulence. *Phys. Fluids*, 20:095102, 2008.

[31] W.W. Grabowski and L.P. Wang. Growth of cloud droplets in a turbulent environment. *Annu. Rev. Fluid Mech.*, 45:293, 2013.

[32] Hamilton. *MICROLAB 500B/C usermanual*.

[33] S. Hartland and D. Robinson. Unsymmetrical drainage beneath a rigid sphere approaching a deformable liquid-liquid interface. *Chem. Eng. Sci.*, 25:277, 1970.

[34] Y.A. Hassan and E.E. Dominguez-Ontiveros. Flow visualization in a pebble bed reactor experiment using PIV and refractive index matching techniques. *Nucl. Eng. Des.*, 238:3080, 2008.

[35] J.O. Hinze. Fundamentals of the hydrodynamic mechanism of splitting in dispersion processes. *AIChE Journal*, 1:289, 1955.

[36] P.D. Howell. The draining of a two-dimensional bubble. *J. Eng. Math.*, 35:251, 1999.

[37] F.O. Iancu. *Droplet dynamics in a fluid environment. A mesoscopic simulation study*. PhD thesis, Delft University of Technology, 2005.

[38] A. K. Jain. *Fundamentals of digital image processing*, volume 3. Prentice-Hall Englewood Cliffs, 1989.

[39] Y.J. Jiang, A. Umemura, and C.K. Law. An experimental investigation on the collision behaviour of hydrocarbon droplets. *J. Fluid Mech.*, 234:171, 1992.

[40] J. Kim. *Binary drop coalescence in liquids*. PhD thesis, University of Minnesota, 2009.

[41] J. Kim and E. K. Longmire. Investigation of binary drop coalescence using dual-field PIV technique. 2006.

[42] J. Kim and E.K. Longmire. Investigation of binary drop rebound and coalescence in liquids using dual-field PIV technique. *Exp. Fluids*, 47:263, 2009.

[43] E. Klaseboer, J.P. Chevaillier, C. Gourdon, and O. Masbernat. Film drainage between colliding drops at constant approach velocity: experiments and modeling. *J. Colloid Interf. Sci.*, 229:274, 2000.

[44] H. Kočárková, F. Rouyer, and F. Pigeonneau. Film drainage of viscous liquid on top of bare bubble: Influence of the bond number. *Phys. Fluids*, 25:022105, 2013.

[45] M. Kwakkel. Private communication. 2011.

[46] M. Kwakkel, W.P. Breugem, and B. Boersma. Extension of a clsvof method for droplet-laden flows with a coalescence/breakup model. *J. Comput. Phys.*, 253:166, 2013.

[47] A. La Porta, G. A. Voth, F. Moisy, and E. Bodenschatz. Using cavitation to measure statistics of low-pressure events in large-reynolds-number turbulence. *Phys. Fluids*, 12:1485, 2000.

[48] G. La Porta, A. Voth, A. Crawford, J. Alexander, and E. Bodenschatz. Fluid particle accelerations in fully developed turbulence. *Nature*, 409:1017, 2001.

[49] O.A. Ladyzhenskaya and R.A. Silverman. *The mathematical theory of viscous incompressible flow*, volume 76. Gordon and Breach New York, 1969.

[50] A. Lai, N. Bremond, and H.A. Stone. Separation-driven coalescence of droplets: an analytical criterion for the approach to contact. *J. Fluid Mech.*, 632:97, 2009.

[51] H. Lamb. *Hydrodynamics*. 1932.

[52] L.G. Leal. Flow induced coalescence of drops in a viscous fluid. *Phys. Fluids*, 16:1833, 2004.

[53] E. K. Longmire. Private communication. 2014.

[54] H.G. Maas, A. Gruen, and D. Papantoniou. Particle tracking velocimetry in three-dimensional flows. *Exp. in Fluids*, 15:133, 1993.

[55] R. Menke. Droplet collisions in a liquid. Master's thesis, Delft University of Technology, 2013.

[56] U. Miessner, E. Coyajee, R. Delfos, R. Lindken, and J. Westerweel. Private communication. 2006.

[57] C.A. Miller and L.E. Scriven. The oscillations of a fluid droplet immersed in another fluid. *J. Fluid Mech.*, 32:417, 1968.

[58] Z. Mohamed-Kassim and E.K. Longmire. Drop impact on a liquid–liquid interface. *Phys. Fluids*, 15:3263, 2003.

[59] Z. Mohamed-Kassim and E.K. Longmire. Drop coalescence through a liquid/liquid interface. *Phys. Fluids*, 16:2170, 2004.

[60] M.B. Nemer, X. Chen, D.H. Papadopoulos, J. Bławzdziewicz, and M. Loewenberg. Hindered and enhanced coalescence of drops in stokes flows. *Phys. Rev. Lett.*, 92:114501, 2004.

[61] M.B. Nemer, X. Chen, D.H. Papadopoulos, J. Bławzdziewicz, and M. Loewenberg. Comment on two touching spherical drops in uniaxial extensional flow: Analytic solution to the creeping flow problem. *J. Colloid Interf. Sci.*, 308:1, 2007.

[62] F.T.M. Nieuwstadt. Turbulentie. *Theorie en toepassingen van turbulente stromingen. Epsilon Uitgaven*, 1998.

[63] C. Ortiz-Dueñas, J. Kim, and E.K. Longmire. Investigation of liquid–liquid drop coalescence using tomographic PIV. *Exp. Fluids*, 49:1, 2010.

[64] J.D. Paulsen, J.C. Burton, S.R. Nagel, S. Appathurai, M.T. Harris, and O.A. Basaran. The inexorable resistance of inertia determines the initial regime of drop coalescence. *P. Natl. Acad. Sci. USA.*, 109:6857, 2012.

[65] B. R. Pearson, T. A. Yousef, N. E. L. Haugen, A. Brandenburg, and P.Å. Krogstad. Delayed correlation between turbulent energy injection and dissipation. *Phys. Rev. E*, 70:056301, 2004.

[66] C. Pozrikidis. *Boundary integral and singularity methods for linearized viscous flow.* Cambridge Univ Press, 1992.

[67] H.M. Princen. Shape of a fluid drop at a liquid-liquid interface. *J. Coll. Sci. Imp. U. Tok.*, 18:178, 1963.

[68] J. Qian and C.K. Law. Regimes of coalescence and separation in droplet collision. *J. Fluid Mech.*, 331:59, 1997.

[69] F. Ravelet. *Bifurcations globales hydrodynamiques et magnétohydrodynamiques dans un écoulement de von Kármán turbulent.* PhD thesis, Ecole Polytechnique X, 2005.

[70] F. Ravelet, A. Chiffaudel, and F. Daviaud. Supercritical transition to turbulence in an inertially driven von kármán closed flow. *J. Fluid Mech.*, 601:339, 2008.

[71] I.V. Roisman, C. Planchette, E. Lorenceau, and G. Brenn. Binary collisions of drops of immiscible liquids. *J. Fluid Mech.*, 690:512, 2012.

[72] S. Salber and E. K. Longmire. Droplet collisions in a liquid-liquid flow with surface tension. Master's thesis, University of Minnesota, 2004.

[73] S.M. Soloff, R.J. Adrian, and Z.C. Liu. Distortion compensation for generalized stereoscopic particle image velocimetry. *Meas. Sci. Technol.*, 8:1441, 1997.

[74] J.W. Strutt, Baron Rayleigh. *The Theory of Sound*, volume 2. Macmillan and Co, New York, 1896.

[75] T. Tanaka and J.K. Eaton. A correction method for measuring turbulence kinetic energy dissipation rate by PIV. *Exp. Fluids*, 42:893, 2007.

[76] C. Tang, P. Zhang, and C.K. Law. Bouncing, coalescence, and separation in head-on collision of unequal-size droplets. *Phys. Fluids*, 24:022101, 2012.

[77] T. Tobin, R. Muralidhar, H. Wright, and D. Ramkrishna. Determination of coalescence frequencies in liquid-liquid dispersions: effect of drop size dependence. *Chem. Eng. Sci.*, 45:3491, 1990.

[78] S. Tokgoz, G.E. Elsinga, R. Delfos, and J. Westerweel. Spatial resolution and dissipation rate estimation in taylor–couette flow for tomographic PIV. *Experiments in fluids*, 53:561, 2012.

[79] F. Toschi and E. Bodenschatz. Lagrangian properties of particles in turbulence. *Annu. Rev. Fluid Mech.*, 41:375, 2009.

[80] D. C. Tretheway, M. Muraoka, and L. G. Leal. Experimental trajectories of two drops in planar extensional flow. *Phys. Fluids*, 11:971, 1999.

[81] C. Tsouris and L.L. Tavlarides. Breakage and coalescence models for drops in turbulent dispersions. *AIChE Journal*, 40:395, 1994.

[82] G. Voth, K. Satyanarayan, and E. Bodenschatz. Lagrangian acceleration measurements at large reynolds numbers. *Phys. Fluids*, 10:2268, 1998.

[83] K. Willis and M. Orme. Binary droplet collisions in a vacuum environment: an experimental investigation of the role of viscosity. *Exp. Fluids*, 34:28, 2003.

[84] N. Worth. *Tomographic PIV measurement of coherent dissipation scale structures.* PhD thesis, 2010.

[85] D. Wunsch, P. Fede, O. Simonin, and P. Villedieu. Numerical simulation and statistical modeling of inertial droplet coalescence in homogeneous isotropic turbulence. In *Turbulence and Interactions*, pages 401–407. Springer, 2010.

[86] S.G. Yiantsios and R.H. Davis. On the buoyancy-driven motion of a drop towards a rigid surface or a deformable interface. *J. Fluid Mech.*, 217:547, 1990.

[87] Y. Yoon, F. Baldessari, H.D. Ceniceros, and G.L. Leal. Coalescence of two equal-sized deformable drops in an axisymmetric flow. *Phys. Fluids*, 19:102102, 2007.

[88] Y. Yoon, M. Borrell, C. C. Park, and L. G. Leal. Viscosity ratio effects on the coalescence of two equal-sized drops in a two-dimensional linear flow. *J. Fluid Mech.*, 525:355, 2005.

[89] P.J. Zandbergen and D. Dijkstra. Von Kármán swirling flows. *Annu. Rev. Fluid Mech.*, 19:465, 1987.

[90] P. Zhang and C.K. Law. An analysis of head-on droplet collision with large deformation in gaseous medium. *Phys. Fluids*, 23:042102, 2011.

Acknowledgements

I'd like to thank the following people: Jerry, René and Gerrit for being good colleagues and advisors. I know it is sometimes not easy to work together with an occasionally stubborn guy like me, but all in all it is very much appreciated and I wish all of you all the best in the future, both career wise and personal.
The social environment of the laboratory for Aero- and Hydrodynamics, or 'the lab', is one thing I will surely miss. Christian, I loved our band's practice sessions, Wim-Paul, Daniel, Dirk-Jan, Marc, Marieke, Manu, Sita, Vincent, Mathieu, Astrid, Arnoud, Marcel Kwakkel, Pedro, Peter, Valentina K, Valentina V, Mark, Maurice, Sacha, Sebastian, Massimo, Sedat, Norbert, Carole, Henk, Uli and Gijs, I enjoyed being colleagues and friends thoroughly. I'd also like to thank the people at the Leeghwater office that Mark and I could come over and play table football and meet everyone at the office. Hyoungsoo, Nikolay, Greta and Jerke, being roommates is kind of special, I enjoyed it a lot and I'd like to thank all of you for all the help and support.
One thing I was a bit less fond of was being in the board of Panta Rhei, the representatives and simultaneously odd job responsibles of the lab. Jasper, Daniële, and Pepijn, I think you were the best board of Panta Rhei during my time at the lab. It's not nothing to realize a one week lab outing during your phd project but you showed the conviction to do it together with Jerry. I enjoyed the trip to Switzerland a lot. The only criticism I can think of is that the coffee could have been a tad stronger.
I'd also like to thank all the non-scientific staff: Edwin a.k.a. Ed Edsen a.k.a. Led Ledsen, Jasper, Simon, Rob, Ria, Caroline, Cor, Joop, Jan and Gerben. I gave probably all of you a hard time at some point because of some reason, but you all helped me out one way or the other. Of course I cannot forget Chris and Ellert from Flowmotion and also Zoubia.
Also I'd like to thank all master students during my time at the lab, specifically: Ruben, Paul 'hypersonic bath' Lunen, Sander, Renée, Vincent, Frans-Jan, Maarten, Arjang, Tjerk, Renzo, Andrea, Gabriele and Joost. Finally I'd like to wish all new bachelor, master, and phd students at the lab all the best.
Because my official employer is Stichting FOM I had the opportunity to do a number of courses on different and useful topics like presentation techniques and potentially less useful topics like business management. Doing these courses together with fellow FOM phd students was always good fun and I'd like to thank especially Sietse van de Post and Adrian de Nijs for this.
I spent the last three months at the Nuclear Research Group (NRG) in Petten and I would

like to thank my colleages and research students there for the good time I had: Santosh, Tadej and Ed, Tomasso, Donato and Camilla, Varun, Leo, Henny, Heleen, Dirk, Vinay, André, Ferry, Nyke and Caroline, Liesbeth and Afaque.
My parents are just the nicest parents imaginable, Cobi and Siebrand, thanks for being so supportive and for helping anytime I need some help. Corné and Alexandra, thanks for being a happy couple.
Finally, and as my father would say: "Lest bût not liest", I'd like to thank my friends: Friso, Marije and Lelie and Emilie, Sjoerd, Gunay and Raul, Saskia, Milan and Emma and Melisa, my former roomies Bob and Enrico, Sebas, Joost and Siri, Wouter and Nicky, Floor and Lucy, Joost and Piet, Frank, Bonne and Bea, Mick, Dirk, Bruce, Jedu and Darcy, Florian and Ilana, Bats, Dio and Anne, Aik, Daan, Collin, Stefan 'Egghead' and Nicki, Alex, Hos, Tijs, Rutger, Vera, Baskerville, Jeroen and all Revert 95 till ∞, Marianne and Rosanne, Erik and Roos and Elize, Jaap and Judith, Reinout and Lisa, the Dudes, all Delft and Westland skaters: Martijn, Robin, Abdi and Patricia, Floyd and the Hoogendijk family, Marc-Peter and Astrid, Jasper, Arne, Ruud, Vincent, Daan and Gaab, Rob Dekker, Rob Vollaard, Shaldi and Stella, Milan, Tanguy, Aletta and Jorge, Isabel, Tim, Ivo, Cas and Judith, Baris, Tom Galesloot, Job and Ilse, Silas and Rianne, Patrick Hurd, Shada, Marieke, Dirk-Jan, Floris and Hark, Rory, the Rinnooy Kan family, Marc Gerritsma and of course everyone that I forgot!

Gosse Oldenziel
Heemstede, January 2014

About the Author

Gosse Oldenziel,
born on June 24th, 1980
in Haarlem, The Netherlands

1992 - 1998	**High school**, Adriaen Pauw Atheneum, Heemstede (VWO).
1999 - 2007	**Bachelor and Master of Science in Aerospace engineering**, Delft University of Technology. Thesis title: *The Least Squares Spectral Element Method for 1D hyperbolic differential equations.*
2007 - 2009	**Researcher at TNO Science and Industry**, Group of acoustics.
2009 - 2013	**PhD researcher at the Laboratory for Aero- and Hydrodynamics**, Faculty of Mechanical, Maritime and Material sciences (3ME), Delft University of Technology.
2013 - 2014	**Computational fluid dynamics researcher**, Nuclear research and consultancy group (NRG).
2014 - now	**Hydrodynamics researcher**, Deltares.

Publication

G. Oldenziel, R. Delfos and J. Westerweel, *Measurements of liquid film thickness for droplets at a two-fluid interface.* Phys. Fluids **24**, 022106 (2012)

Conference contributions

American Physical Society, meeting of the division of fluid dynamics (APS-DFD).

- 2012, San Diego - Oral presentation, title: *Droplet collisions in a liquid.*
- 2011, Baltimore - Oral presentation, title: *Measurements of liquid film thickness for droplets at a two-fluid interface.*

Burgers day for fluid dynamics.

- 2012, Eindhoven - Oral presentation, title: $1 + 1 = 1$.
- 2010, Enschede - Poster presentation, together with M. Kwakkel.

Physics at FOM.

- 2012, Veldhoven - Oral presentation, title: *Measurements of liquid film thickness for droplets at a two-fluid interface.*
- 2010, Veldhoven - Poster presentation, together with M. Kwakkel.